Imaging Methodology for Assessment of Chronic Disease

by

Carmen Celeste Taylor

DISSERTATION

Submitted in partial satisfaction of the requirements for the degree of

DOCTOR OF PHILOSOPHY

in

BioEngineering

in the

GRADUATE DIVISION

of the

UNIVERSITY OF CALIFORNIA, SAN FRANCISCO

AND

UNIVERSITY OF CALIFORNIA, BERKELEY

Copyright

Acknowledgements

I would like to thank Sharmila Majumdar, Thomas Link, and Dave Attwood for all of their help and guidance during the course of preparing this thesis. Their advice and support have been invaluable.

I would also like to thanks Sarah Nelson for her assistance in changing thesis labs. I very much appreciate her taking an interest in me and helping me to find a great lab in which to finish my graduate studies.

Finally, I would like to thank my friends and family for their patience and support throughout graduate school.

Abstract

Chronic diseases such as cancer and cardiovascular disease are among the leading causes of death in industrialized nations such as the United States. In addition, many other chronic diseases such as osteoarthritis result in disability and reduced quality of life for even more people, especially as they age. Imaging modalities, such as single-photon emission computed tomography (SPECT) magnetic resonance imaging (MRI), and x-ray computed tomography (CT), have a unique advantage in the area of medical research relative to their classical counterparts such as histology and gross pathology. Noninvasive imaging methodologies are an attractive alternative for obtaining physiologic assessments without disruption of the phenomenon of interest.

In response to the importance placed on noninvasive small animal studies at the biological and medical research fronts, the focus of this work is on the advancement of imaging technologies which will augment and extend the current capabilities of noninvasive imaging systems. In the initial portion of this thesis, we will focus on the advancement of SPECT and CT techniques used to measure perfusion and those biological factors to which it is correlated, including improvements in physiological monitoring, dual-isotope imaging, and dual-modality imaging. In addition, we will complement our design focus with an illustration of the effectiveness of the small animal imaging approach to the study of osteoarthritis using MRI. We will illustrate the utility of imaging techniques via an ***ex vivo*** MRI study of human osteochondral specimens, and then we will apply them to study the development of osteoarthritis ***in vivo*** in a rabbit model.

Contents

List of Tables

List of Figures

Chapter 1

Thesis Introduction and Overview
Introduction to Small Animal Imaging

I. Introduction to Chronic Disease

Chronic diseases such as cancer and cardiovascular disease are among the leading causes of death in industrialized nations such as the United States[1]. In this country, approximately two out of every five people who die this year will die of heart disease. Of the rest, another one will die of cancer, and approximately one more will die of a stroke[1]. In addition, many other chronic diseases such as osteoarthritis result in disability and reduced quality of life for even more people, especially as they age. As science advances, we are developing more understanding of these diseases and better treatments for not only the root diseases but also their symptoms.

Although the advent of improved treatments is very exciting, health service use and the associated medical costs have risen dramatically in recent years and are expected to continue to rise as the prevalence of chronic conditions continues to expand[2]. Furthermore, it is becoming increasingly evident that these conditions depend upon a number of risk factors, many of which interact, and most of which are poorly understood. For example, one such factor which is common to many chronic conditions is blood flow, or perfusion. In the arena of heart disease, perfusion of the ventricular myocardium is essential to its function: decreases in perfusion lead first to substandard performance, followed by irritability, arrhythmia, and eventually death. An associated factor is sympathetic innervation:

sympathetic stimulation of the heart leads to increases in heart rate, contractility, and ejection fraction. However, although we can surmise that a relationship between the effects of perfusion and innervation in the formation of heart disease exists, the exact process by which it takes place is not well understood. As such, there is a large body of study devoted to the improvement of our understanding of the molecular mechanisms involved in the evaluation of tissue perfusion and the factors which influence its evolution.

In addition, due to the enormous achievements of molecular biology, several transgenic and knockout cell lines and animal models are now available as subjects for scientific study[3]. In the biological arena, small animals such as rodents are the models of choice. Their advantages include small size, which corresponds to low cost and ease of housing; short reproductive cycle, which allows the relatively quick generation of interesting disease models and transgenics; and genetic similarity to humans, which makes the study of small animal biology useful to the study of human conditions.

II. Imaging As a Means to Study Disease Processes

Traditionally, much biological and medical research has utilized invasive methods, such as histologic studies, to tease out relationships between different molecular components in rodent models of disease[4]. These classical methods are advantageous in that they allow researchers to obtain high-quality data with good spatial resolution and quantitative information, but they also have some significant drawbacks. For example, excision of diseased tissue may potentially interfere with the disease process under study; in extreme cases this may make longitudinal studies difficult or impossible, resulting in the inability to

follow the evolution of a disease process over time. Some researchers attempt to circumvent this problem by studying several groups of animals at different time points. Although this approach is valid and has contributed to much of our understanding of various pathological process, it is not ideal. The associated time and expense of increasing the number of animals in any given scientific study is a major consideration for any researcher: studies involving tissue sampling or autoradiography are often labor-intensive. In addition, normal variation between individual study participants, even between members of the same species, complicates analysis of the underlying pathology[5]. Thus, there is opportunity for improvement.

Imaging modalities, such as single-photon emission computed tomography (SPECT) magnetic resonance imaging (MRI), and x-ray computed tomography (CT), have a unique advantage in the area of medical research relative to their classical counterparts. For example, due to the noninvasive nature of imaging studies, each animal can serve as its own control. Not only does this eliminate natural variation between individuals, but it also reduces experimental costs and the number of animals required for a given study. The low labor-intensive nature of an imaging study further benefits the research in terms of personnel time and cost. In particular, imaging techniques such as those presented here benefit from the relative ease of imaging agent procurement, the relatively low cost of these agents, and their ability to be handled and manipulated in a laboratory setting. Therefore, noninvasive imaging methodologies are an attractive alternative for obtaining physiologic assessments without disruption of the phenomenon of interest, especially in serial or other studies which benefit from comparing repeated measurements made over a

period of time[6].

In response to the importance placed on noninvasive small animal studies at the biological and medical research fronts, and given the advantages of imaging studies listed above, the focus of this work is on the advancement of imaging technologies which will augment and extend the current capabilities of noninvasive imaging systems.

In the initial portion of this thesis, we will focus on the advancement of SPECT and CT techniques used to measure perfusion and those biological factors to which it is correlated, including improvements in physiological monitoring, dual-isotope imaging, and dual-modality imaging. Specifically, we will focus our efforts on the leading causes of death in industrialzed society: cancer and heart disease. These investigations will expand the range of options of our microSPECT/CT imaging systems as a means of obtaining medically relevant physiologic and pathologic data, allowing researchers greater flexibility in experimental design and better capabilities for ***in vivo*** data collection.

In addition, we will complement our design focus with an illustration of the effectiveness of the small animal imaging approach to the study of osteoarthritis using MRI. Osteoarthritis, like heart disease and cancer, is a chronic condition. However, in contrast to these other pathologies, osteoarthritis does not directly contribute to mortality. Instead, the disease and its effects persist for long periods of time, often decades, rendering osteoarthritis second only to heart disease in producing long-term disability[7]. We will illustrate the utility of imaging techniques via an ***ex vivo*** MRI study of human osteochondral specimens, and then we will apply them to study the development of osteoarthritis ***in vivo*** in a rabbit model.

Before discussing these advancements and applications, however, we will summarize the principles by which SPECT and MRI operate and by which an image is obtained. In this manner, we lay the foundation for the work developed in this thesis.

III. Techniques and Instrumentation for Small Animal Imaging

III.I Introduction to the Tracer Effect and SPECT

SPECT imaging of radionuclides is based on the notion of tracers, which reside on the principle that different isotopes of the same element exhibit identical chemistry; we expect this to be the case because chemistry is dominated by interactions between electrons, and radioisotopes differ from their nonradioactive counterparts by virtue of altered nuclear composition. For example, if an atom which exhibits a certain type of chemistry in a given pharmaceutical is replaced by its radioactive counterpart, we expect that the radioactive pharmaceutical and the nonradioactive pharmaceutical will behave in identical (chemical) ways when injected into an organism. Thus we can use radionuclides to follow molecules of biological interest as they interact with an organism's tissues. In addition, if we choose a pharmaceutical with the appropriate biological properties (i.e., one with a high binding coefficient for a cell-surface receptor), we can study a physiological process with only a very small quantity of radiolabeled pharmaceutical. Moreover, as illustrated by George de Hevesy's work which received the Nobel prize in Chemistry in 1943, when radioisotopes are utilized in concert with the tracer principle, researchers can obtain very sensitive and accurate measures of processes such as biological uptake. This principle forms the basis for the noninvasive nature of SPECT imaging.

III.II Use of the Pinhole Collimator in Small Animal SPECT

To produce an image of the radiotracer distribution within an animal or a phantom (an inanimate representation of an animal), we must first establish a mapping function which relates physical points in our animal with representative points in our image. In conventional imaging systems such as microscopes, this correlation is established through the use of refractive and reflective optics which change the direction of photon travel such as lenses and mirrors. However, because high-energy gamma rays tend to penetrate most conventional optical materials, and fail to change their direction of travel upon interaction with these materials, current methods of radionuclide imaging rely not on redirecting photons of interest to form an image, as optical systems do, but instead produce a mapping between object and image via methods of deducing photon direction such as absorptive collimation. In particular, small animal SPECT makes use of the pinhole collimator as its imaging system of choice.

Figure 1: Pinhole Camera Geometry

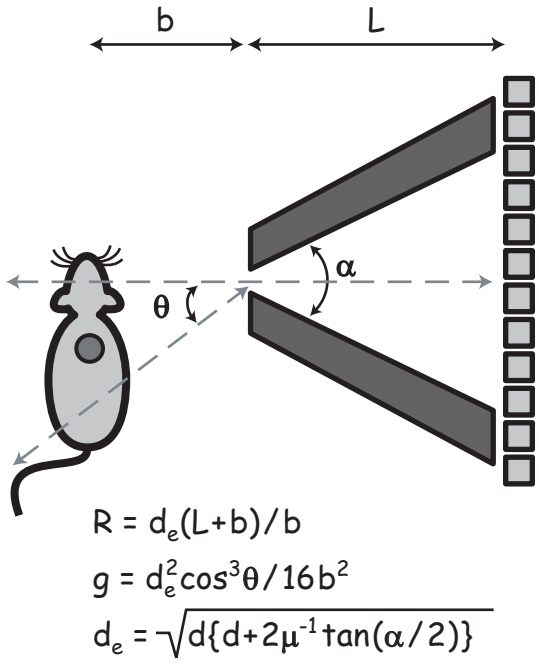

Pinhole collimators used for nuclear medicine consist of a small hole drilled into a thick plate of highly attenuating media, such as lead. These collimators produce both high spatial resolution and reasonable sensitivity, at least when the object of interest is placed close to the pinhole[8]. To illustrate, consider the situation in which a measurement of myocardial uptake in a mouse is acquired

using a perfusion tracer which accumulates in viable myocardium. As shown in Figure 1[9], the mouse is positioned for imaging very near to the pinhole collimator. Photons emitted from the mouse travel in all directions, but those that are recorded by the scintillation camera must travel through the pinhole, which creates a relationship between the location of photon detection in the camera and the direction of photon travel from mouse to camera. The image formed compresses the three dimensional radionuclide distribution information into a two-dimensional image, and the resulting data recorded by the pinhole camera is known as a projection image.

Because it is usually the main determinant of the overall spatial resolution and efficiency of photon (signal) collection, the geometry of a such a pinhole collimator is an important consideration of the imaging system. Using the figure above as a reference, we can derive expressions for the resolution and efficiency of a given pinhole collimator geometry. Specifically, the efficiency g is given by the formula

$$g = (d_e^2 / 16b^2) \cos^3\theta$$

where b is the distance from the pinhole to the source, L is the distance from the pinhole to the detector, and θ is the angle between the source and the central axis of the collimator. Here we define an effective diameter of the pinhole d_e as

$$d_e = (d\,(d + 2\mu^{-1}\tan(\alpha/2)))^{1/2}$$

where d is the nominal diameter of the pinhole, α is the acceptance angle of the pinhole, and μ is the attenuation coefficient of the collimator material. Using the same notation, the resolution R is given by the formula

$$R = d_e(L+b) / L$$

A derivation of these equations can be found in Sorenson and Phelps[8].

From these equations, we can see that to obtain high resolution with a pinhole collimator, we must sacrifice high efficiency. This is a critical tradeoff which is a central limitation to imaging via absorptive collimation; imaging systems which acquire data with submillimeter resolution often operate with efficiencies of less than 10^{-5}, which translates to increased imaging times for many experiments. Moreover, these increased imaging times in themselves also present challenges to the experimenter. For example, in our heart experiment above, a measurement of cardiac output using electrocardiogram gating would require the production of several images corresponding to phases of an "average" heartbeat from a combined data set which was recorded over the course of several individual heartbeats. This averaging in turn requires that the animal's heart rate remain constant over the course of the entire experiment, necessitating careful attention to physiological factors which affect the heart's function such as the animal's core body temperature and the level of anesthesia. Therefore, successful pinhole imaging must be done with care to achieve optimum results.

III.III CT Imaging as a Means to Improve SPECT Measurements

Although pinhole imaging can produce good images of physiologic data, recently it has been shown that the functional utility of SPECT imaging can be enhanced by combining the SPECT data with correlated CT images[10, 11]. Anatomical knowledge provided by CT images can be incorporated into iterative SPECT reconstruction techniques to better

quantify physiological function, tracer localization, and biological uptake/distrubution. To perform CT imaging, an x-ray beam is generated by accelerating electrons toward a target which produces x-rays as a result of the collision. This beam is directed toward and through the patient or object of interest and the amount of attenuation of the beam is recorded by a detector on the other side, producing a projection image. By acquiring many such projection images at different angles around the patient, we can combine the information to generate a three-dimensional attenuation map of the patient. This attenuation map corresponds to patient anatomy and can be used diagnostically in some cases (e.g., finding a lung tumor), but it has additional utility in helping us to correct and quantify physiologic information obtained from SPECT imaging.

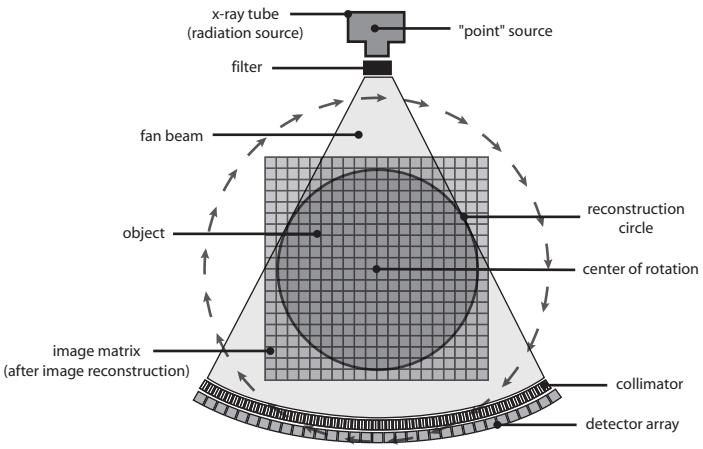

Figure 2: CT Geometry

III.IV Introduction to Magnetic Resonance Imaging

In addition to our SPECT/CT studies, we will also employ magnetic resonance imaging to pursue an application of small animal imaging. Magnetic resonance imaging utilizes the phenomenon of nuclear spin to produce image data. Most commonly, MRI is performed by manipulating the nuclear spin of hydrogen atoms, due to their high abundance in soft tissues. To illustrate how this process takes place, consider what happens when the nucleus of a hydrogen atom (a proton) is placed within a magnetic field[15].

The proton which makes up the hydrogen nucleus has a property known as spin. In classical mechanics, spin would be associated with the rotation of some amount of mass about a central point, analogous to the motion of the Earth about its axis. Because the proton is also charged, the "motion" created by spinning this charge is associated with a magnetic dipole moment, μ. We can quantify this relationship as

$$\mu = \tilde{a}\, S$$

where S is the spin angular momentum of the proton and the proportionality constant ã is known as the gyromagnetic ratio. When placed in an external magnetic field, the magnetic moment of the proton produces a torque on the magnetic moment which is proportional to the strength of the external magnetic field and tends to align the magnetic moment with the external field. More interesting, however, is what happens to the spin angular momentum as a function of time. We can calculate this behavior using basic quantum mechanical formalism in which the Hamiltonian H is just the energy associated with alignment of the proton's magnetic moment with the external field B_0.

$$H = \tilde{a}\, B_0 \cdot S$$

We will follow the derivation of Griffiths[16] below. Here, we find that the eigenstates associated with such a system are of the form

$$a\, e^{i\tilde{a}B_0 t/2} \quad \text{and} \quad b\, e^{-i\tilde{a}B_0 t/2}$$

where a and b are constant and the sum of their magnitudes is equal to unity. Choosing the forms of a and b, we may write the general solution to the Schrodinger equation as

$$\div(t) = \cos(á/2)\, e^{iãB_0t/2} + \sin(á/2)\, e^{-iãB_0t/2}$$

where á is a constant determined by the initial conditions of the experiment. If we look further, we find that we can calculate the expectation value of the proton's spin as a function of time as

$$\langle S_x \rangle = \div(t)^\dagger\, S_x\, \div(t) = (ħ/2) \sin á \cos(ã\, B_0 t)$$

$$\langle S_y \rangle = \div(t)^\dagger\, S_y\, \div(t) = (-ħ/2) \sin á \sin(ã\, B_0 t)$$

$$\langle S_z \rangle = \div(t)^\dagger\, S_z\, \div(t) = (ħ/2) \cos á$$

These results[15] clearly show that we expect that the spin of a proton tilted with respect to the external B_0 field will precess about the axis of the B_0 field at a frequency equal to ã B_0. This frequency is known as the Larmor frequency. Without external simulation, the proton's spin will tend to align with the external magnetic field. However, because an electromagnetic field exerts a torque on the magnetic moment of the proton, we can manipulate this parameter by stimulation with radiofrequency (RF) pulses. MRI takes advantage of this fact to produce an image first by placing a volume of interest (i.e., soft tissue) in a static magnetic field and then by exciting the volume using an RF pulse. An antenna placed close to the volume of interest is then used to detect the signal produced by the precessing hydrogen nuclei. As the protons within the tissue volume rotate, their magnetic fields interact with those in the tissue surrounding them. The interaction is accompanied by the transfer of energy from the protons to the surrounding tissue, which in turn degrades the signal from the rotating nuclei. The nature of this signal degradation is related to the composition of the surrounding tissue, and we can indirectly infer the chemical composition and health of the tissue based on the rate at which the signal relaxes

back into its pre-excitation state.

IV. Thesis Overview

We will begin with the development of methodology, specifically SPECT and CT methodology which will be applied to cardiovascular disease and cancer. We will then move to the implementation of hardware such as anesthesia and heating which will allow ***in vivo*** studies of small animals. At the present time, funding difficulties prevent the validation of our SPECT development work and so we will instead present preliminary data from SPECT experiments. After presentation of these preliminary results, we will then redirect our interest to a set of validation studies using magnetic resonance imaging for the final section of this thesis. We will briefly introduce the principles by which MRI operates, and, in contrast to the development work presented in the SPECT section, we will introduce two studies which are quite applied in nature. First we will perform a validation study using MRI to investigate imaging parameters related to osteoarthritis ***ex vivo*** in surgical specimens; then we will use these imaging parameters to follow the development of the disease in an ***in vivo*** rabbit model.

IV.I Development of Dual-Isotope SPECT Methodology

The ability to acquire data from two—or more—biological processes in just one imaging session is one of the great advantages of an imaging modality such as SPECT over other modalities such as computed tomography (CT) or positron emission tomography (PET), in which only a single measurement can be made at a time. This is an especially large

advantage in studies which specifically target correlations between biological entities of interest as the source of the investigation. For example, in this work we are interested in correlations such as those between perfusion and inflammation, between perfusion and innervation, and between perfusion and radiosensitivity. Ideally, to characterize these relationships, it is desirable to measure both quantities simultaneously. Dual-isotope methodology is especially suited to this role.

Unfortunately, the microSPECT/CT imaging system in our laboratory does not currently have the capability to perform dual-isotope SPECT, although the hardware contained within the system could support such a capability. Therefore, we desire to develop the methodology ourselves. SPECT techniques, due to the nature of photon acquisition, lend themselves to energy discrimination as a means of differentiation between two simultaneously acquired sets of data. We will employ our knowledge of photon acquisition to perform this task by characterizing the energy response of our recently-obtained X-SPECT microSPECT/microCT small animal imaging system (Gamma Medica-Ideas, Northridge, CA) to two radionuclides which exhibit photopeaks that differ widely in energy: technetium-99m (^{99m}Tc) and iodine-125 (^{125}I). Because no tools are provided by the manufacturer for examining any form of the raw data, this process will first require that we find and decode this raw data. Once this has been done, we will then perform phantom experiments to determine our ability to construct useful projection data from the raw data from individual isotopes and reconstruct those projections into tomograms. We will then separate the two signals and characterize the crosstalk between them. We will also model the interaction of these high-energy photons with objects in the field of view and with our

detector using Monte Carlo simulation techniques to expand our understanding of the detection and crosstalk processes in our system.

IV.II Hardware Specializations For Small Animal Imaging

We also desire not only to develop dual-isotope methodology but also to test its efficacy *in vivo*. Although the imaging community has done a considerable amount of work in specializing SPECT and CT imaging hardware to be compatible with sizes relevant to small animals[8], much of the current focus has been on the imaging hardware itself (such as detector systems with enhanced resolution); correspondingly less work has been done in areas pertaining to support of the animal's physiology during the course of data acquisition. Therefore, in addition to our interest in dual-isotope studies, we will also discuss the implementation and specialization of SPECT/CT imaging equipment which will enhance the quality and accuracy of perfusion-related measurements by better accommodating the physiological needs of small animals. As part of this study, we will also make some additional hardware modifications to our X-SPECT imaging system which will allow us to image live animals. These improvements will include anesthesia, heating, and catheterization of small animals.

IV.III MicroSPECT/CT Perfusion Studies Using Mouse Models of Human Pathology

Finally, we will explore the application of imaging to the study of small animal models of human disease. Clinical SPECT studies are in large part comprised of bone and metabolic

scans, to detect cancer metastasis; and heart and viability scans, to evaluate extent of cardiovascular disease. Clinical CT studies often involve structural evaluations such as imaging of blood vessels, tumors, and hemorrhage. Noninvasive ***in vivo*** measurements are central to each. We have chosen to study representative animal models in each area to illustrate the utility of the technical advances developed in this work.

IV.IV Dual-Isotope SPECT Studies

For our dual-isotope SPECT studies, we will focus first on the Welm model of metastatic mammary carcinoma[12]. This model is an orthotopic model in which primary cells are removed from the mammary glands of a normal mouse; infected with a retrovirus carrying the genes for some combination of the polyoma middle T antigen (PyMT), dsRed, GFP, and macrophage stimulating protein (MSP); and returned to the cleared inguinal fat pad of the mouse. There, these cells form large primary tumors, and depending on the genes transferred to them, also metastasize to the lung and skeleton. This model is an excellent opportunity to study the relationship between perfusion, MSP, and metastasis.

We are also interested in the Conklin mouse model of dilated cardiomyopathy (DCM)[13,14]. This mouse expresses a constitutively active receptor (Ro1) which is suppressed by the presence of tetracycline antibiotics. The mouse is physiologically normal when its diet is supplemented by antibiotics, but develops a severe cardiomyopathy and ventricular conduction delay followed shortly by heart failure and death upon the removal of those antibiotics from its diet. Because we can image the mouse before and after the induction of disease, this mouse represents a unique opportunity to assess the effects, if any,

of the sympathetic nervous system on the development of heart failure and arrhythmia.

IV.V Contrast-Enhanced CT as an Added Dimension of Perfusion Imaging

In addition, we would further like to extend the utility of our methodology to include complementary perfusion measurements made with CT. Although CT imaging is often used to help localize and enhance the physiological information provided by SPECT[9], it may often be used to provide functional perfusion imaging in its own right. Because many researchers tend to focus exclusively on the functional capabilities of one modality, the ability of dual-modality imaging to provide information about ***physiological*** correlations (as opposed to structural/physiological relationships) is often overlooked. The ability of CT to provide functional information about perfusion will also open up the possibility of using combined dual-isotope SPECT/CT to assess the effect of ***interactions*** between biological molecules on perfusion. Therefore, in addition to our evaluation of perfusion correlations via SPECT agents, we will evaluate a new CT contrast agent, Fenestra VC, as a perfusion marker. Previous studies using CT contrast agents to evaluate perfusion have suffered from difficulties involving x-ray beam hardening and contrast agent washout during the experiment[15]. We believe that the use of this new contrast agent in mice will greatly reduce these difficulties, due to the small size of the mouse and the long vascular retention time of this agent. In addition, we will develop a new method of mathematical decomposition of CT images to provide quantitative data about the steady state location and extent of soft tissue perfusion.

This measurement will be of interest not just to arteriogenesis and cardiovascular studies,

but will also be relevant to cancer studies, in which the ability of a tumor to respond to chemotherapeutic drugs or radiation treatments often rests on its level of perfusion. In particular, there is much interest in the level of oxygen available to the tumor, which is dependent upon blood flow; hypoxia (a low level of oxygen) often confers radioresistance to certain areas of large tumors, making them difficult to treat. Again, although almost any mouse model of cancer could be used, the Welm model of mammary carcinoma would provide an excellent opportunity to test this idea ***in vivo***.

IV.VI MRI and the Study of Soft Tissues

Now that we have presented the above development work in the SPECT arena, we would like to focus our remaining efforts on validation studies which will be performed using magnetic resonance imaging (MRI). Magnetic resonance imaging is an imaging modality which has undergone remarkable advancement in recent years; in recognition of this, in 2003 Paul Lauterbur and Peter Mansfield were awarded the Nobel Prize in Medicine for their achievements in this arena. MRI has many advantages, including excellent soft tissue image contrast, which allows us to study pathologies which might not be accessible directly using x-ray or gamma ray based methods such as SPECT or CT. We will begin by summarizing the principles by which images are acquired in MRI; we will then follow up by describing two validation studies which employ these principles to study the pathology of degenerative joint disease.

IV.VII MRI in the Study of Osteoarthritis

Clinical MRI focuses on the evaluation of soft tissues. We will take advantage of this strength to employ MRI in the study the degradative changes which occur in the soft tissues of the knee during the development of osteoarthritis.

Osteoarthritis (OA) is a chronic degenerative disease characterized primarily by the loss of articular cartilage. Loss of articular cartilage may lead to inflammation, pain, and associated pathology such as the growth of new vasculature, osteophyte development, and joint space narrowing. Traditionally, osteoarthritis has been diagnosed by these secondary indicators of cartilage loss via radiographic examination[17], in which a planar x-ray is used to assess the presence or absence of osteophytes and the width of the joint space; determination of pathology is based on indirect measures of surrounding anatomical structures[18]. Although this is an effective approach, because radiographs lack the ability to directly image soft tissues, they tend to be limited to the detection of disease only at later stages of progression[19]. Therefore, there is much interest in the development of new imaging techniques which would allow diagnosis of osteoarthritis at an early stage of disease, ideally before tissue loss has occurred.

Magnetic resonance imaging is a promising alternative to radiographic examination of joints exhibiting degenerative changes due to its strengths in the evaluation of soft tissues. In this work, these strengths will be employed to study changes apparent in cartilage specimens obtained from osteoarthritis patients who will undergo total knee arthroplasty (TKA). We will compare each of the most promising MRI methodologies and also a

contrast-enhanced CT method to study the pathologic changes in the cartilage of each of these specimens; moreover, the acquisition of imaging data from various techniques in these specimens will facilitate a direct comparison between the data acquired with each method. Because there is some controversy in the field regarding the specific imaging technique best suited to the study of articular cartilage degradation, these specimens represent an excellent opportunity to perform a comprehensive imaging study. Hence, we will determine which of these methods, if any, are complementary and therefore might be used together to provide a more complete picture of the underlying pathology in osteoarthritis.

In addition to these ***ex vivo*** studies, we will extend the results of our imaging experiments to an ***in vivo*** study in rabbits in which osteoarthritis has been induced via transection of the anterior cruciate ligament (ACL) in the hind limb of the animal. Mimicking ACL tear injuries sustained by athletes, this model is of interest to the study of osteoarthritis because it is well known to develop degenerative joint changes secondary to surgical insult[20-22]. Moreover, the development of disease is quite rapid, occurring over the course of a few weeks following anterior cruciate transection, facilitating its study in a research setting. In particular, we propose to use this model to investigate the prognostic value of T1ρ and T2 imaging measures for the assessment of early osteoarthritis. Combined with the aforementioned imaging data, this study will provide us with valuable information regarding the development of osteoarthritis in a traumatic setting.

V. Discussion

The methodology developed here will expand the range of options of our microSPECT/CT imaging systems as a means of obtaining medically relevant physiologic and pathologic perfusion information pertinent to the leading causes of death and disease in industrialized nations. In addition, the preclinical studies performed using MRI will lend insight into the pathological basis underlying the development of a major source of human disability. These advancements will in turn allow researchers greater flexibility in experimental design and better capabilities for ***in vivo*** data collection, which in turn will yield better experimental information about physiologic relationships. In time, this new information may also yield improved treatments for many chronic diseases which trouble society today.

VI. References

1. Minino, A.M., M.P. Heron, and B.L. Smith, ***Deaths: preliminary data for 2004***. Natl Vital Stat Rep, 2006. 54(19): p. 1-49.

2. ***Heart Disease and Stroke Statistics—2004 Update***. 2004, American Heart Association: Dallas, Texas.

3. Bernstein, A. and M. Breitman, ***Genetic ablation in transgenic mice***. Mol Biol Med, 1989. 6(6): p. 523-30.

4. Jaffer, F.A. and R. Weissleder, ***Molecular imaging in the clinical arena***. JAMA, 2005. 293(7): p. 855-62.

5. Peremans, K., et al., ***A review of small animal imaging planar and pinhole spect Gamma camera imaging***. Vet Radiol Ultrasound, 2005. 46(2): p. 162-70.

6. Weisenberger, A.G., Bradley, E.L., Majewski, S., Saha M.S., ***Development of a novel radiation imaging detector system for in vivo gene mapping in small animals***. IEEE Trans Nucl Sci, 1998. 45: p. 1743-49.

7. Cotran RS, Kumar V, Collins T, Robbins SL. *Robbins Pathologic Basis of Disease.* W.B. Saunders Company; 6th edition (January 15, 1999)

8. Wu, M.C., B.H. Hasegawa, and M.W. Dae, ***Performance evaluation of a pinhole SPECT system for myocardial perfusion imaging of mice***. Med Phys, 2002. 29(12): p.

2830-9.

9. Cherry, S.R., Sorenson, J., Phelphs, M., ***Physics in Nuclear Medicine***. 3 ed. 2003: Saunders.

10. Hasegawa, B.H., et al., ***Dual-modality imaging of cancer with SPECT/CT.*** Technol Cancer Res Treat, 2002. 1(6): p. 449-58.

11. Hasegawa, B.H., et al., ***Dual-modality imaging of function and physiology.*** Acad Radiol, 2002. 9(11): p. 1305-21.

12. Welm, A.L., et al., ***The macrophage-stimulating protein pathway promotes metastasis in a mouse model for breast cancer and predicts poor prognosis in humans.*** Proc Natl Acad Sci U S A, 2007. 104(18): p. 7570-5.

13. Redfern, C.H., et al., ***Conditional expression of a Gi-coupled receptor causes ventricular conduction delay and a lethal cardiomyopathy.*** Proc Natl Acad Sci U S A, 2000. 97(9): p. 4826-31.

14. Redfern, C.H., et al., ***Conditional expression and signaling of a specifically designed Gi-coupled receptor in transgenic mice.*** Nat Biotechnol, 1999. 17(2): p. 165-9.

15. Miles, K.A. and M.R. Griffiths, ***Perfusion CT: a worthwhile enhancement?*** Br J Radiol, 2003. 76(904): p. 220-31.

16. Griffiths, D.J., ***Introduction to Quantum Mechanics***. 1995: Prentice-hall, Inc.

17. Altman, R., J. Fries, and D. Bloch, *Radiographic assessment of progression in osteoarthritis.* Arthritis Rheum, 1987. **30**: p. 11.

18. Rogers, J., Watt, and P. Dieppe, *A comparison of the visual and radiographic detection of bony changes at the knee joint.* BMJ, 1990. **300**: p. 367-368.

19. Chan, W.P., et al., *Osteoarthritis of the knee: comparison of radiography, CT, and MR imaging to assess extent and severity.* Ajr Am J Roentgenol, 1991. **157**(4): p. 799-806.

20. Smith, G., Jr., et al., *Effect of intraarticular hyaluronan injection on vertical ground reaction force and progression of osteoarthritis after anterior cruciate ligament transection.* J Rheumatol, 2005. **32**(2): p. 325-34.

21. Smith, G.N., Jr., et al., *Effect of intraarticular hyaluronan injection on synovial fluid hyaluronan in the early stage of canine post-traumatic osteoarthritis.* J Rheumatol, 2001. **28**(6): p. 1341-6.

22. Smith, G.N., Jr., et al., *Diacerhein treatment reduces the severity of osteoarthritis in the canine cruciate-deficiency model of osteoarthritis.* Arthritis Rheum, 1999. **42**(3): p. 545-54.

Chapter 2

List-Mode Data Processing in the X-SPECT System

I. Introduction

In the study of human disease, radionuclide tracers are often used *in vivo* to discriminate between viable and nonviable or cancerous and noncancerous tissue[1, 2]. The measurement of localized radionuclide uptake by a given tissue in a clinical or preclinical environment is often accomplished via imaging techniques such as single photon emission computed tomography (SPECT). Unlike other imaging modalities such as computed tomography (CT) and positron emission tomography (PET), SPECT imaging has a unique advantage in biological research due to its ability to simultaneously collect *in vivo* data from two sources at once (dual-isotope imaging).

In particular, recognizing the extraordinary attention the medical community currently directs on the elucidation of biological relationships, we will focus here on extending the capabilities of the X-SPECT microSPECT/CT imaging system into the arena of simultaneous dual-isotope studies, in which data from two distinct radiopharmaceuticals can be collected and correlated during the course of a single study. This work will allow investigators to elucidate biological relationships between perfusion and such phenomena as inflammation, carcinogenesis, heart failure, G-protein activation, ischemia, and arrhythmia. By acquiring correlation data simultaneously, as opposed to sequentially, researchers will be better able to assess correlations and elucidate relationships between various biological entities of interest. The development of methodology for dual-isotope imaging will be

broken up into two chapters: methodology pertaining to decoding and manipulating the raw data obtained from our microSPECT/CT scanner, and methodology which utilizes these manipulations to separate the signal from one isotope from the signal emitted by the second isotope. Methodology pertaining to the formatting and manipulation of the scanner's raw data will be the subject of this chapter.

II. Background

II.I Radionuclide Detectors Used for Small Animal SPECT

A common detector configuration currently used for small animal SPECT relies on scintillators to convert high-energy radiation into visible light for the production of images. Scintillators used in nuclear medicine are most often coupled to PMTs to produce what is known as an Anger camera, which is illustrated in Figure3[3] below. In this arrangement, gamma rays pass through the imaging collimator and are incident on a scintillator, which converts the energy of the incoming high-energy photon into visible light. The light output of a scintillator depends on the energy absorbed by the scintillator. Therefore, in order

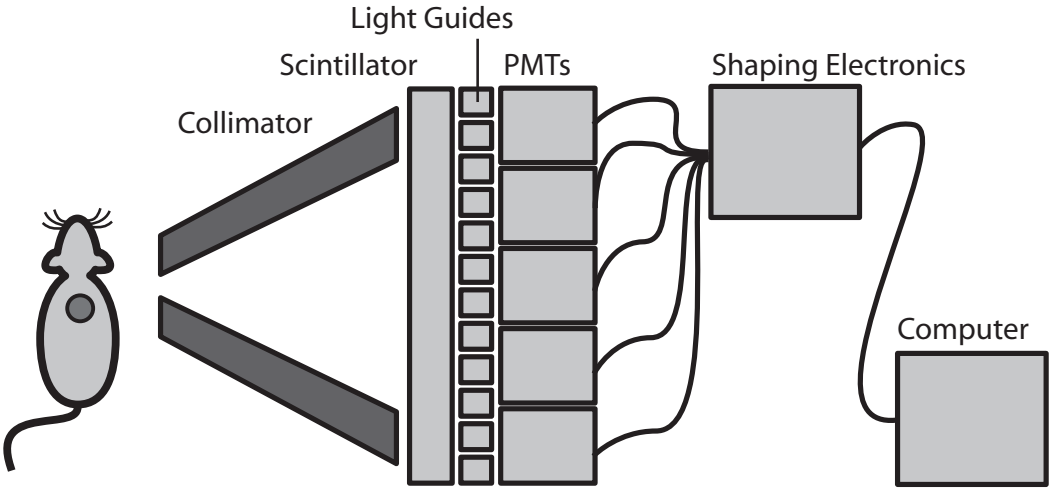

Figure 3: Gamma Camera

to increase the probability that an incident gamma ray is detected, it is desirable for the scintillator to have a high density or to be made of materials with high atomic number. In addition, the absorbance of the scintillator can be increased by increasing the thickness of the scintillator material. This increase in sensitivity comes with an inherent drawback, however; the thicker the crystal, the more light will spread as it propagates through the crystal, leading to a positional degradation in the output signal.

The most common scintillator material used in nuclear medicine today is sodium iodide (NaI) doped with thallium, NaI(Tl)[3]. NaI(Tl) is highly absorbing to high-energy photons such as those emitted from ^{99m}Tc, is relatively transparent to visible light, and produces a high light output per amount of crystal-absorbed radiation. Once the energy in an incident gamma ray is converted to visible light in a gamma camera's scintillator, this visible light propagates through the rest of the scintillator crystal and is transferred to a light guide, at the end of which the light is collected by an array of photomultiplier tubes housed directly behind the scintillator and light guide. Here, as shown[3], visible light photons are converted by the PMT to electrical current. Each PMT contains a photocathode, which converts visible light into electrical charge; a series of dynodes, which amplify the number of electrical charges by accelerating them through a known voltage; and an anode, which collects the amplified charge and delivers it to the system electronics responsible for cataloging the signal based on such features as location and energy. In a typical gamma camera, these electronics employ a weighted average of the

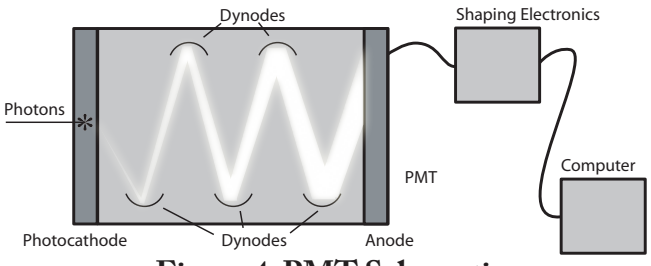

Figure 4: PMT Schematic

combined scintillator outputs to determine the location of gamma ray impingement on the scintillator crystal, and they use the combined total output of all PMTs to determine the energy of the incident gamma ray (the strength of the signal output by each PMT is proportional to the average amount of light input on the PMT face).

II.II The X-SPECT Anger Camera

The X-SPECT microSPECT imaging system employs an Anger camera as its radionuclide detection system. This camera consists of a sodium iodide scintillator crystal doped with thallium, NaI(Tl), which is pixelated into a 54 x 54 array of individual units 2 mm (L) x 2 mm (W) x 6 mm (T). Each of these crystals is optically isolated from the others by 0.2 mm of diffuse, optically opaque, reflective material. As discussed earlier, the scintillator is coupled to an 5 x 5 array of position-sensitive photomultiplier tubes through the use of a light guide. The overall dimensions of the gamma camera in its housing are 20 cm x 15 cm, which includes the lead bucket shielding the detector from stray photons. The pinhole collimator has a 9 cm focal length. Several interchangeable tungsten pinhole apertures are available for this collimator, and range from 0.5 mm to 2 mm. Although the X-SPECT can be configured with two gamma cameras, the system studied here contains just a single detector.

II.III Radionuclide Energy Spectra and Use of Energy Windowing

As discussed in Chapter 1, absorptive collimation produces a projection image on the basis of creating a relationship between detection location in the gamma camera and incident

photon direction. By combining several different SPECT projections taken from several different vantage points, the distribution of radionuclides in a patient or phantom can be estimated. There are, however, some difficulties inherent in this method of estimation. First, photons may be absorbed by photoelectric interactions in the patient, which would lead to a misestimation of radionuclide local activity when the amount or content of tissue between the radionuclide source and gamma camera varies. Second, photons emitted from a radionuclide source may undergo Compton scattering. As shown in the figure[4], a gamma ray changes direction when undergoing a Compton scattering event. In addition, the gamma ray loses energy during this process dependent upon the angle through which it was scattered:

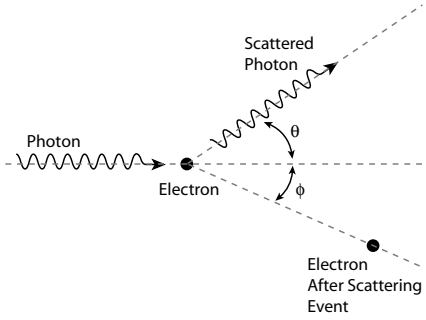

Figure 5: Compton Scattering

$$E = \frac{1}{\frac{(1 - \cos\theta)}{mc^2} + \frac{1}{E_0}}$$

where E is the energy of the scattered photon, E_0 is the energy of the incident photon, θ is the angle through which the photon is scattered, m is the mass of the electron, and c is the speed of light. As shown in the equation[4] above, if we set the scattering angle to 180 degrees, we can maximize the energy transfer from the photon to the scattering media. This results in a "Compton edge" in the final spectrum acquired by a gamma camera.

A gamma ray may also undergo coherent scattering, in which it changes direction but not energy. At nuclear medicine energies, coherent scattering events make up only a few percent

of the total amount of scattered photons[3]. Both of these types of scattering events result in the degradation of the contrast in nuclear medicine images. In addition, photons may interact with or scatter within the collimator or detector itself, producing both a Compton continuum and one or more escape peaks in the final spectrum.

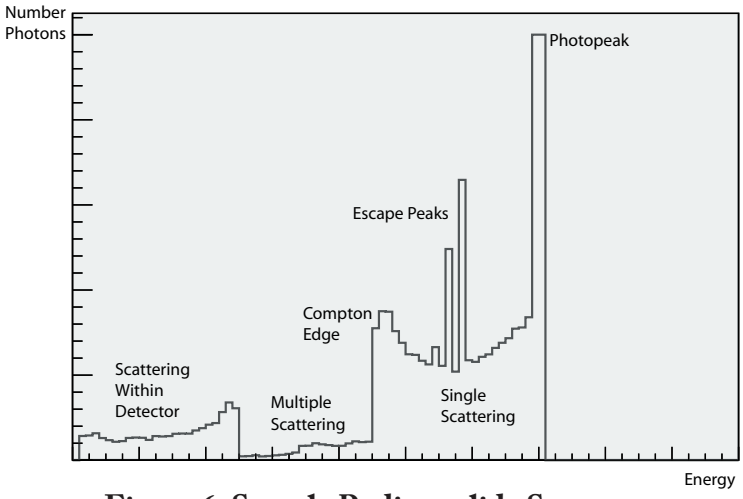

Figure 6: Sample Radionuclide Spectrum

To partially eliminate the contribution of scattered photons to the final image, we can use the fact that the total output of a gamma camera is dependent on energy. Because it is known that Compton scattering involves the above noted shift in photon energy, most researchers in nuclear medicine employ this knowledge by ignoring photons which fall outside of a window around a radioisotope's emission photopeak. This energy discrimination, known as energy windowing, increases the contrast of the acquired image at the expense of system sensitivity.

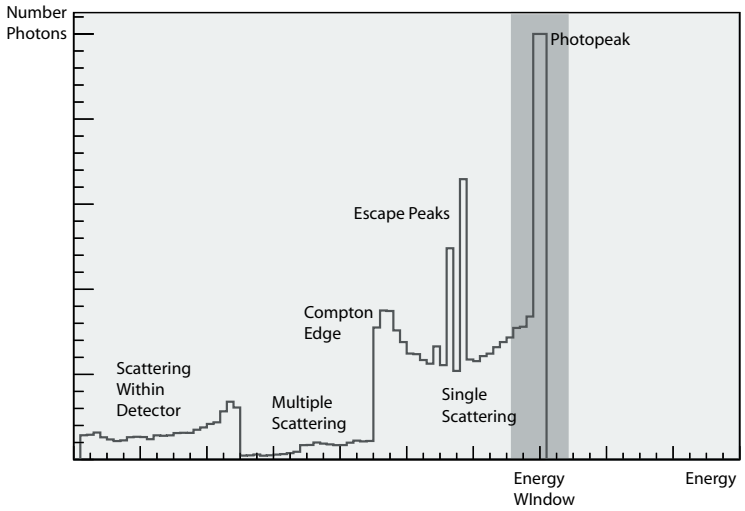

Figure 7: Energy Windowing

In addition, energy windowing allows us to discriminate between photons emitted from different radioactive isotopes if the primary photopeaks of the two isotopes differ significantly in energy. This very valuable property of SPECT imaging allows us to gather data about two or more biological entities simultaneously, which greatly simplifies the analysis relating to correlations between them (as discussed above). This is especially advantageous in medical or biological applications which employ measurements in living organisms to investigations such as the influence of risk factors on disease potential.

II.IV Dual-Isotope SPECT Imaging

Practically speaking, to assess the relative amounts of two radionuclide tracers taken up by a particular volumetric region using SPECT imaging, it is desirable to discriminate between the two tracers when they arrive at the SPECT detector and before they are reconstructed into three-dimensional tomograms. As discussed above, this discrimination is most commonly done on the basis of photon energy because SPECT acquisition is by nature energy-dependent. In addition, we must account for the fact that photons

may lose energy during a scattering interaction in either the imaging subject, or the detector itself. The amount of energy lost in such a scattering event is highly variable and, notwithstanding the possibility of multiple scattering events, may result in higher-energy photons being detected as lower-energy photons. This crosstalk may lead to misquantitation of radionuclide data, and so it is desirable to characterize our imaging system in order to minimize or compensate for such errors.

Because we are using energy to discriminate between radioisotopes, we will characterize the response of the imaging detector in the energy regimes pertinent to the isotopes used in each experiment; in our case, this will include energies ranging from 0 to 150 keV. The first step in any energy calibration must be the calibration and characterization of the response of radiation detector itself; to do this, we must therefore find and decode the raw (unprocessed) data from the detector. The location, decoding, and subsequent processing of the raw data format comprise the bulk of this chapter.

III. Methods

The energy calibration presented here was done on the single gamma camera present in our X-SPECT system (Gamma Medica Ideas, Northridge, CA). The raw data produced by the gamma camera used in the X-SPECT system may also be referred to from this point on by the commonly used term *list-mode data*. Although the software provided by the manufacturer of the X-SPECT can produce list-mode data, no tools are provided with which to edit the calibrations used to produce SPECT images and no method is provided to examine the raw data itself. For this reason, it was chosen to examine the raw data

manually and develop custom methods to decode and process the list-mode format of the unprocessed files. The development of custom methodology also allowed the capabilities of the X-SPECT system to be extended in order to include such functions as simultaneous dual-isotope imaging, which are not currently commercially available at this time. This chapter will begin with locating and formatting the raw data.

III.I Location of the X-SPECT's Raw Data

Before any calibration could be developed on our system, the format of the raw data had to be deciphered. Gamma Medica Ideas, the manufacturer of the X-SPECT system, was able to provide information that the location of the raw data was the LMData folder in the SPECT computer, but they were not forthcoming with much additional information. Inspection of the LMData folder, however, revealed that the X-SPECT stores raw SPECT data in separate files; and there is a one-to-one correspondence between the number of files and the number of projections. Each projection file was found to have a name of the form

Tomo_15_49_31_001.bin

The word *Tomo* designates a tomographic scan, and may be replaced by the word *Dyn* in the event of a dynamic (planar) scan or *GTomo* in the event of a cardiac-gated tomographic scan. Observation indicates that the next three numbers are a time stamp indicating the local time when the experiment began. In addition, the last number appears to represent a relative value corresponding to the image frame number; in the case of tomographic data, it represents the projection number.

III.II Elucidation of the X-SPECT's raw data format

Because our gamma camera consists of a sodium iodide scintillator coupled to an array photomultipliers tubes, it was hypothesized that Anger logic would govern the positioning of photon interaction within the detector and thus suspected that the raw data corresponding to each photon would be stored as a group of four numbers. To illustrate, let us represent each of these groups of four integers as

$$\text{photon} = [x_1, x_2, y_1, y_2]$$

With this format, two dummy variables *x* and *y,* may be calculated using Anger logic to represent an approximate location of interaction between an incoming photon and the detector's scintillator as follows:

$$x = x_1 / (x_1 + x_2)$$

$$y = y_1 / (y_1 + y_2)$$

III.III Look-Up Tables

Next, it was suspected that this crude calculation of incident photon position would require a correction for distortion, and hence would also require a detector-specific look-up table. After some judicious searching, a likely candidate was found in one of the calibration directories: a table called LUT_140.bin. It was assumed that this table was created for the 140-keV photon emitted from the commonly-used radioisotope technetium-99m (^{99m}Tc). Based on the LUT_140.bin file size (524,288 bytes) and on knowledge supplied by the X-SPECT manufacturer concerning detector geometry (square geometry, divided into 54

x 54 pixels), it was hypothesized that the look-up table was composed of 512 x 512 signed integers (524,288 = 512 x 512 x 2, 2 bytes for a signed integer) corresponding to pixel addresses. This hypothesis also correlated with the expected number of distinct values contained within the table (54 x 54 + 1 = 2917 distinct values). As shown in the results section, inspection of the LUT_140.bin data confirms that this guess is likely correct.

In addition, the discovery that the LUT_140.bin data was stored in signed integer format suggested two modifications to the list-mode processing methodology above. First, because the LUT_140.bin file contained 512 x 512 entries, the above calculation approximating the *x* and *y* detector position values was scaled as follows:

$$x = 511 * x_1 / (x_1 + x_2)$$

$$y = 511 * y_1 / (y_1 + y_2)$$

where each raw *x* and *y* value is scaled from 0 to 511. This method assumes that all of the data in the LUT_140.bin file is used to represent the entire detector in the X-SPECT and that none of the data is used to represent a header or other type of information. Again, the image of the LUT file is consistent with this interpretation of the data.

III.IV Elucidation of Time Stamp Encoding

The knowledge that the LUT_140.bin data was stored in signed integer form also suggested that the list-mode projection data might also be stored as signed integers. Presuming upon this idea, the encoding of other types of experimental information within the raw data set were determined as well. Gamma Medica claims that the X-SPECT had the capability

to acquire cardiac images which could be gated off an external electronic trigger from a rodent electrocardiogram (ECG) monitor. This information suggested that two types of recognizable signals occurring within the list-mode projection data may be found: a time stamp, and an ECG stamp. Moreover, given that the average mouse's heart beats about 600 times every minute and that it would be expected that the rate of time sampling be even greater than the rate of incoming ECG triggers, it was also expected that the time stamp and ECG stamp patterns would be the most common types of information contained within the raw data file. Therefore, to ferret out these signals the data was plotted from an ECG-gated list-mode file (acquired from an ECG gated study of a rat) as a histogram.

Noting the two most common values in the histogram, the data was inspected for patterns corresponding to time or other information; after all, each function unit of data in the Anger logic format commonly used with this type of gamma camera contains four numbers, not one. In addition, it was noted that these two values were the only negative values in the entire data set and that all other values encountered were positive, another indication that these particular values had special significance. (Initially, every fourth value in the data set was negative, but this was due to a wiring error which the manufacturer repaired after learning of it. It is surmised that this particular positive/negative format is used in SPECT systems with two or more gamma cameras as a means of identifying which camera recorded each event.) Wiring errors aside, further inspection of the data revealed that the time stamp values always occur in groups of three, and it was also observed that the ECG stamp value always occurred in the presence of a group of three time stamp values. Furthermore, it was observed that this combination never occurred in the absence of an

ECG trigger's presence during an experiment. In addition, comparison of the number of these time stamp signals with known values of heart rate (approximately 400 beats per minute) as measured by the rodent ECG monitor during the experiment suggests that a time stamp is recorded every millisecond during the course of an experiment, which was deemed a reasonable value for such a parameter.

III.V Choice of a Reading Frame

Based on these observations, it was decided to write custom IDL code to use the *[time stamp, time stamp, time stamp, value]* combination to denote the reading frame and process the list-mode data from the X-SPECT. To determine the reading frame accurately, in our code no data within the raw data file is processed until a time/ECG stamp is encountered; this is due to the observation that data present prior to an ECG stamp is often incomplete (as indicated by a nonintegral multiple of four entries which is expected for Anger logic). After this stamp has been found, the reading frame is set to that of the time/ECG stamp and is used to process all subsequent data. Exceptions to this rule are noted in the next section.

III.VI Removal of Truncation Errors

Employing the above method to process and parse the raw data must be done with some care, however. In our experience, the X-SPECT does not always record the raw data in groups of four integers (i.e., sometimes there are six or ten integers between time stamps) and therefore it is easy to misread the data due to a frameshift type of error. The

manufacturer was contacted regarding the apparent discrepancy, but they claimed that they have never observed this type of error and did not wish to continue the discussion. Therefore, whenever a nonintegral multiple of four integers is encountered between successive time or ECG stamps, it was chosen to discard the entire millisecond of data rather than try to discern the reading frame between the time stamps. The reading frame is then reset to that of the time/ECG stamp following the error and this relative frame is used until the next error is encountered. The resultant loss of data due to this feature of our data processing is on the order of 1% or less.

It was also observed that the *value* parameter contained in a *[time stamp, time stamp, time stamp, value]* combination does not always increase in increments of unit value. Occasionally, the increment jumps wildly, with consecutive values exhibiting differences of several thousand. Although sometimes an apparently idiopathic condition, the discrepancies seem to correspond to events in which the experimenter or other user switched control between the SPECT acquisition software window and another window during data acquisition (*i.e.*, when another application was started to transfer data from the SPECT computer to the CT computer in the middle of an experiment). Furthermore, data sets which had relatively large errors of this type did not appear to have increased or decreased numbers of incoming photons recorded compared to data sets with few or no errors. Therefore, this error was interpreted as a small bug in either multithreading or record keeping, as opposed to a large one in which the X-SPECT did not record any data for an unknown span of time. Accordingly, if this error did not also result in a reading frame error, the timing error was noted but the data were treated as though only one millisecond elapsed between

successive time frames.

III.VII Development of Custom Code to Parse and Process List-Mode Data

Using the methodology described above, custom IDL code was developed to parse the list-mode data for each projection into time stamps, ECG stamps, and what is apparently photon data. The photon data is processed according to Anger logic as described previously and the equations above are used to compute values for *x* and *y* (repeated here for clarity)

$$x = 511 * x_1 / (x_1 + x_2)$$

$$y = 511 * y_1 / (y_1 + y_2)$$

Next, the program locates the address of the scintillator pixel corresponding to the interaction location. This address is calculated using the LUT_140.bin look-up table and has a value ranging from -1 to 2915. If I read the LUT_140.bin data in as a 512 x 512 signed integer matrix, I find that

$$\text{Address} = \text{LUT\_140}[511*x + y]$$

Pixel locations corresponding to 0 through 2915 are written to an output file along with the uncalibrated Anger-logic energy value E

$$E = x_1 + x_2 + y_1 + y_2$$

for further processing. Pixel locations corresponding to -1 are discarded, as it is assumed that they correspond to locations at the edge of the detector where it is difficult to determine the exact position of photon interaction within the scintillator. This IDL code was later

converted to C# in light of cost and portability considerations. The C# compiler is free, works on all Windows systems updated with Service Pack 2, and C# code can be written with any text editor such as Notepad. In addition, conversion to C# allows us to implement a Windows interface, which is more accessible to users without advanced computer skills. At the time of conversion from IDL to C#, the program's functionality was expanded, as described in the following sections.

III.VIII A Simple Method of Energy Calibration

Next, the program attempts to eliminate photon scatter and other noise from the data. This can be done on the basis of energy, but first the data from each pixel must be calibrated. To determine the energy calibration, a large data set of photons emitted from a rectangular flood tank filled with activity is collected to ensure adequate sampling; this is accomplished by placing a sample of approximately 5-10 millicuries of radionuclide activity in the scanner and acquiring data over a period of 12 hours (or overnight). Using this data set, a simple energy calibration is performed in which the software first processes the raw data corresponding to photons into raw energy values and pixel locations as described above. Next, a histogram for each pixel is constructed using these uncalibrated energy values. To screen out some of the noise, the histogram is then smoothed with a running mean filter, and the spectrum peak (in raw energy units) is recorded. Exceptionally high peaks corresponding to noise at either end of the spectrum are ignored. Finally, an energy calibration value, which shall henceforth be called an EPT value, is calculated from the raw energy spectrum peak as

EPT = (known photopeak energy in keV) / (measured raw energy peak value)

For example, if pixel 1004 registered a photopeak measured at 127 raw detector units for an experiment utilizing ^{99m}Tc (with a known photopeak at 140 keV), the EPT value for this pixel would be calculated as

$$EPT_{1004} = 140 / 127 = 1.1 \text{ keV / detector unit.}$$

This EPT value is tabulated for each pixel as a floating point value in an EPT.bin file which is also created by our software. Although the X-SPECT does produce a similar EPT table for its own calibration purposes, it was unable to be used to produce an effective energy calibration (as evidenced by the production of nonuniformities during processing of projection data and the corresponding ring artifacts in the reconstructed images). Therefore, the EPT.bin file created by the software is the only EPT table used during the processing of all subsequent SPECT data presented in this document.

III.IX Production of Uniformity Correction Tables

After the completion of the energy calibration, the software next produces a uniformity calibration table using data taken from a flood phantom (this is often the same data set used to construct the original energy calibration but can also be a separate data set) and the EPT.bin data calculated above. Per the X-SPECT manufacturer's recommendation, ^{99m}Tc photons will henceforth be considered "good" or "unscattered" data if their energy is measured to be within -10% or +15% of the 140-keV photopeak. (Should another energy window be desired, the graphical interface developed for the software allows these values

to be changed.) The software next reprocesses the original flood data using the previously calculated EPT values, and it records the total number of "good" photons in each pixel as an image. Again, photons corresponding to pixel address -1 are discarded. The uniformity image is then renormalized to its median value and stored as a uniformity calibration table called UCT.bin. The UCT.bin file is then used as a correction file during projection image data processing as discussed in the following section.

III.X Processing of Projection Data

The software uses high-count calibration data stored in the EPT.bin and UCT.bin files to process projection data, which often suffers from low count statistics. Each projection file is processed separately from every other projection file, although all projections from a given experiment are corrected with the same EPT.bin and UCT.bin files. First, the raw projection data from each file is parsed into photons, ECG stamps, and time stamps as described above. Energies corresponding to photon interactions are calculated for pixel addresses between 0 and 2915 and the photon is counted as "good" if its energy is within the energy window used to construct the UCT.bin file. These good photons are tabulated, and a projection image is formed from the total number of good photons for each pixel. Next, the number of good photons in each pixel is adjusted to reflect the system sensitivity using the UCT.bin data using the formula below:

(adjusted # good photons) = (measured # good photons) / (UCT value)

This correction is done on a pixel-by-pixel basis to ensure that an image of a uniformly-active object is uniform, and can be tested using data from a uniform flood tank phantom: by

dividing the image of the uniform phantom by the UCT table, the uniformity correction can be verified on a pixel-by-pixel basis. Finally, in the event that SPECT data is acquired over a long period of time, each projection data set is corrected for radioactive decay. Each pixel in a given projection has its value adjusted to account for the time elapsed during the course of the experiment and for the corresponding decay of activity during that time. *I.e.*,

$$\text{(decay-corrected \# good photons)} = \text{(adjusted \# good photons)} / \exp(-(\ln 2) * t / T_{1/2})$$

where t is the time elapsed since the start of the projection image acquisition, $T_{1/2}$ is the half life of the radioisotope used during the experiment, and the adjusted # of good photons is the uniformity-corrected number obtained in the above equation. This corrected image is then stored and used to produce tomographic images using an iterative maximum likelihood reconstruction algorithm developed by either Andrew Hwang or Tobias Funk.

IV. Results

IV.I Look-Up Table Data

A graphical representation of the data in the LUT_140.bin file is presented below. This image of the look-up table assumes that the table is composed of 512 x 512 signed integers corresponding to scintillator pixel addresses.

Inspection of the LUT_140.bin data demonstrates that each value within the table ranges from -1 (black) to 2915 (white) and that similar values are clustered together, which is consistent with the known geometry of a 54 x 54 array of detector pixels numbered in

sequence from 0 at the top left to 2915 at the bottom right (2915 = 54 x 54 - 1). Photons which appear to interact with the edges of the detector are assigned an address of -1, indicating that the exact location of interaction is difficult to determine; for this reason, data corresponding to pixel address -1 are discarded and no further calculations are performed on them. All other pixel addresses, specifically those corresponding to distinct scintillator pixels, are represented in gray levels. Pixels with similar gray levels are grouped together, indicating that they correspond to the same or neighboring pixels in the scintillator crystal. In addition, from the scalloped appearance of the edge of the grayscale "good" area of the detector, it is hypothesized that there are 5 x 5 photomultiplier tubes underneath the scintillator crystal which collect light produced from photon interactions. For example, in the scalloped edge, each encroachment of the black area into the grayscale center can be thought to correspond to the division between adjacent photomultiplier tubes—each photomultiplier is more sensitive at the center than at the edges—and because there are four encroachments on each side of the colored area, it is therefore inferred that there must be five photomultiplier tubes in each dimension of the photomultiplier tube array underneath the scintillator.

Figure 8: Look-Up Table (LUT)

IV.II Raw Data Value Histogram

A histogram of the raw data values corresponding to a gated cardiac study in a normal Sprague adult rat (weight > 300 grams) is presented here to illustrate the method of time and ECG stamp encoding.

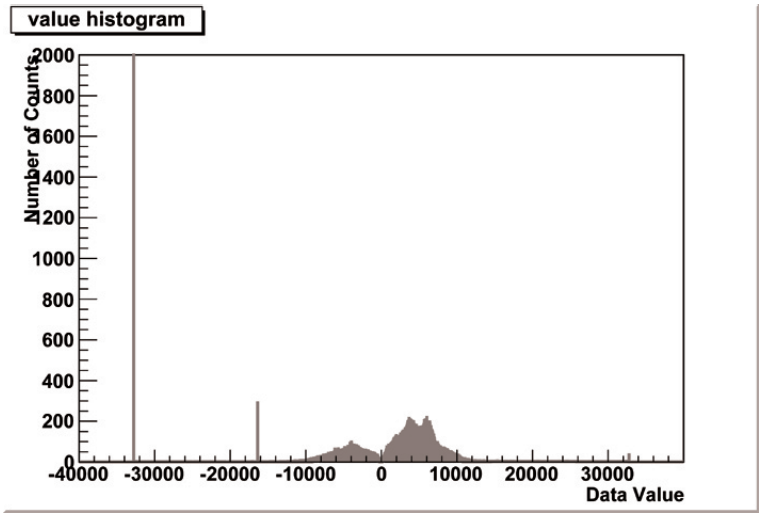

Figure 9: Raw Data Value Histogram

The most common value in the histogram is -32,768 and the next most common value is -16,384. In addition, it is notable that these two values occur as peaks and that all of the other values occur as part of a wider distribution, which is also an indication that these particular values have special significance. (As mentioned above, a service call from the vendor also yielded information when the vendor reported that they had fixed some faulty wiring in the detector, rendering all of the negative *distributed* values positive. This left the peaks at -32,768 and -16384 as the only remaining negative values in the entire data set, again suggesting that these values were special.) Further inspection reveals that the -32,768 values always occur in groups of three, suggesting that a time stamp is encoded in the list-mode data as

$$\text{time stamp} = [-32768, -32768, -32768, \text{value}]$$

and where it is assumed that time stamps occur more frequently than ECG stamps. Consistent with this hypothesis was the observation that each successive *value* parameter recorded was exactly equal to the last *value* parameter plus one:

$$\text{value}_{\text{current}} = \text{value}_{\text{last}} + 1$$

which also indicated that the *value* parameter would be a reasonable candidate for a time stamp. It was observed that this value ranges from 0 to 32,767; when 32,767 is reached the value parameter returns to 0 once again. The starting value of this parameter seems to be arbitrary but likely corresponds to the start time in milliseconds of the experiment.

It was also observed that the -16,384 value always occurred in the presence of a group of three -32,768 values. Furthermore, it was noted that this combination never occurred in the absence of an ECG trigger's presence during an experiment. Together, this suggested that the ECG trigger signal was encoded in the list-mode data as

$$\text{ECG trigger} = [-32768, -32768, -32768, -16384].$$

Comparison of the number of these time stamp and ECG stamp signals with known values of anesthetized rat heart rate (approximately 400 beats per minute) as measured by the rodent ECG monitor during the experiment suggests that a time stamp is recorded every millisecond during the course of an experiment.

IV.III Pixel Spectra

Using the above results, the idea that the code developed accurately parses and manipulates the list-mode data from the X-SPECT system can be partially validated by the appearance of individual pixel spectra obtained with known sources of known isotopes. As described above, the first step in this process is choosing a reading frame, followed by parsing the data into groups of four integers which represent time stamps, ECG stamps, and photons. At this point, the data corresponding to each photon is compiled into individual pixel spectra. Representative ^{99m}Tc and ^{125}I spectra from different areas of the detector are shown in the figure below.

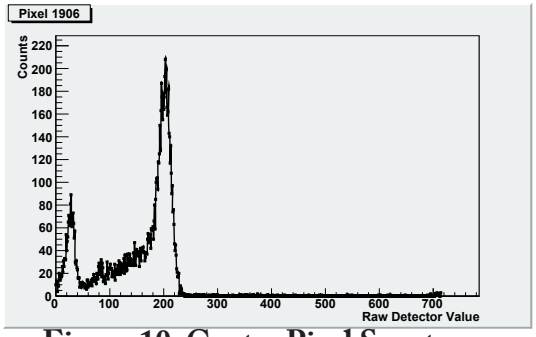

Figure 10: Center Pixel Spectrum

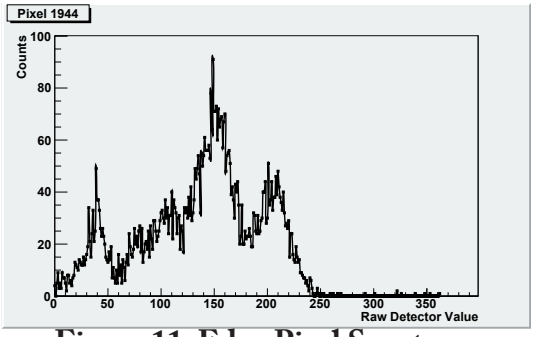

Figure 11: Edge Pixel Spectrum

Spectral quality varies widely based on the location of the pixel within the detector; for example, centrally located pixels tend to exhibit well-defined relatively narrowly-peaked spectra, whereas pixels located near the detector edge often exhibit poorly-defined or multiply-peaked spectra. The figure demonstrates this effect for pixel 1906 and pixel 1944, using a flood source composed of ^{99m}Tc and ^{125}I. Pixel 1906 is located near the center of the detector and exhibits a typical clean spectrum with well-defined photopeaks. However, near the edge of the detector, pixel 1944 exhibits some difficulty resolving the spectrum and hence the final measurement suffers due to high sensitivity to noise.

IV.IV Photopeak Identification and Assignment of EPT Value

The location of the measured photopeak in raw detector units was determined by smoothing the spectrum for each pixel as described above and finding the maximum value in the photopeak region. As shown below, photopeak location for ^{99m}Tc is plotted versus pixel address. The periodic rise and fall of the curve is due to varying sensitivity across the detector face caused by tiling of photomultiplier tubes. Each photomultiplier tube is most sensitive to the scintillator's light output when the light originates near the center of the photomultiplier tube. This same information is also summarized graphically below for ^{99m}Tc, in which each pixel is placed at its geometric location within the scintillator crystal and the photopeak location (value) for that pixel is encoded by grayscale value.

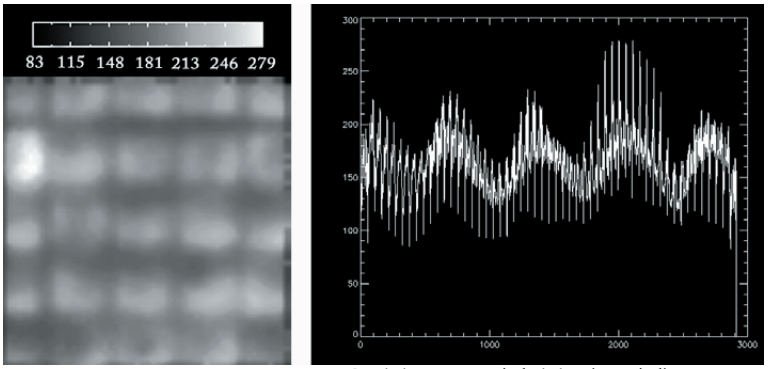

Figure 12: Energy Calibration Table (EPT)

In this representation it is clear that the gamma camera is comprised of an array of 25 photomultiplier tubes arranged in a 5 x 5 array, as had been surmised from the appearance of the LUT_140.bin data earlier. More interestingly, at the left edge of the detector near the top, an area corresponding to a refurbished photomultiplier tube can be discerned. The gain on this photomultiplier tube has been increased relative to the other (new) photomultiplier tubes and this can be visualized in the figure by the increased values of photopeak locations

in the scintillator pixels overlying this photomultiplier tube. Also visible are a number of edge pixels which exhibit noisy spectra. These pixels can be visualized at the top, right, and bottom edges of the detector as a border two pixels thick which exhibits this difficulty. At the right edge of the detector, there is a border of four pixels. Although at this time the discrepancy has not been explained, these noisy pixels are undesirable but do not present a large problem for SPECT imaging because they are located far from the center of the field of view, and hence contribute minimally to the final (reconstructed) tomographic image. Therefore, these errors will be ignored from this point onward.

IV.V Uniformity (UCT) Correction Tables

Using these EPT values and choosing an energy window of [-10%, +15%] of the 140-keV ^{99m}Tc photopeak, a UCT correction value is calculated by the software for each pixel which accounts for the differing sensitivity across the detector surface to incoming photons. The figure below illustrates a sample UCT table taken using this energy window and a 1.0-mm pinhole collimator. Similar to the figures above, a periodic variation of UCT values across the detector face can be visualized. Noisy edge pixels may also be seen in this graphical representation. Although the refurbished photomultiplier tube exhibits altered calibration parameters, the reader may note that this difference is accounted for using the above methodology.

In addition to the intrinsic sensitivity difference across the detector face as seen in the EPT tables, there is also an effect caused by the presence of the pinhole collimator itself, which exhibits a characteristic central area of high sensitivity.

Figure 13: Uniformity Correction

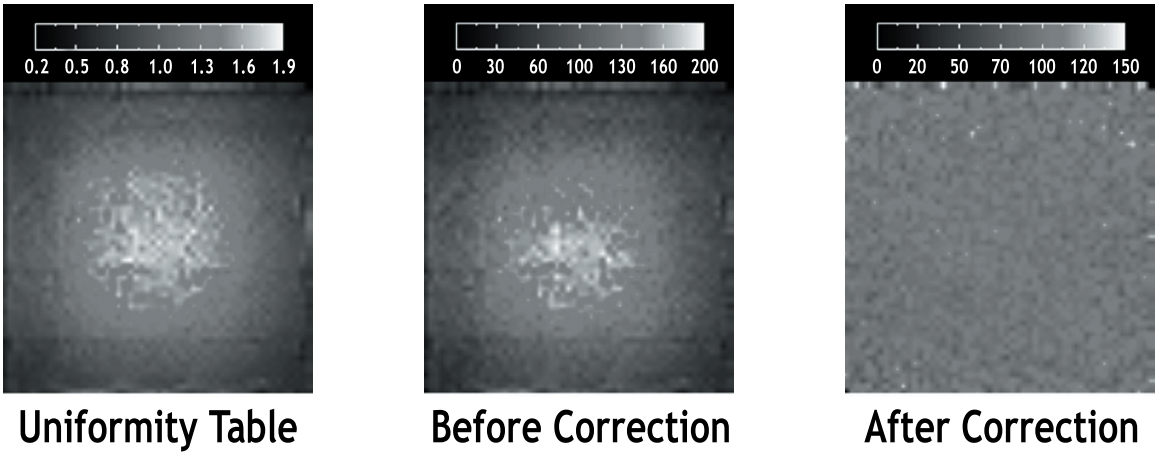

Also shown in the figure is an additional image of a flood tank before and after correction using this UCT table. The uniformity correction transforms this image into one which is uniform across the field of view, which is appropriate for a rectangular container of uniform thickness filled with uniformly distributed ^{99m}Tc activity. After uniformity correction, the image averages 108.4 counts per pixel and has a standard deviation of 10.8 counts per pixel, which is approximately what would be expected for the ideal case exhibiting Poisson statistics.

IV.VI Use of LUT, EPT, and UCT Tables in Projection Data Processing

To verify that the above tables can be used to process projection data taken from a typical SPECT experiment, phantom experiments using a cylindrical flood tank filled with ^{99m}Tc ($Na^{99m}TcO_4$) were performed. Shown below are sample projection images produced by the code developed here. In this experiment, the flood tank was nearly full but contained a small air bubble which can be seen as a "hole" of low activity at the top edge of the visible uniform activity in the tank.

The code developed here was used to produce and process these raw projection images and combine them into a single file; ML-EM algorithms obtained from A. Hwang were used to reconstruct the data tomographically. A sample tomogram and its corresponding line profile are also shown in the figure below. The tomogram shown is a single slice, not an average.

Figure 14: Sample Projections and Tomogram of Cylindrical Flood

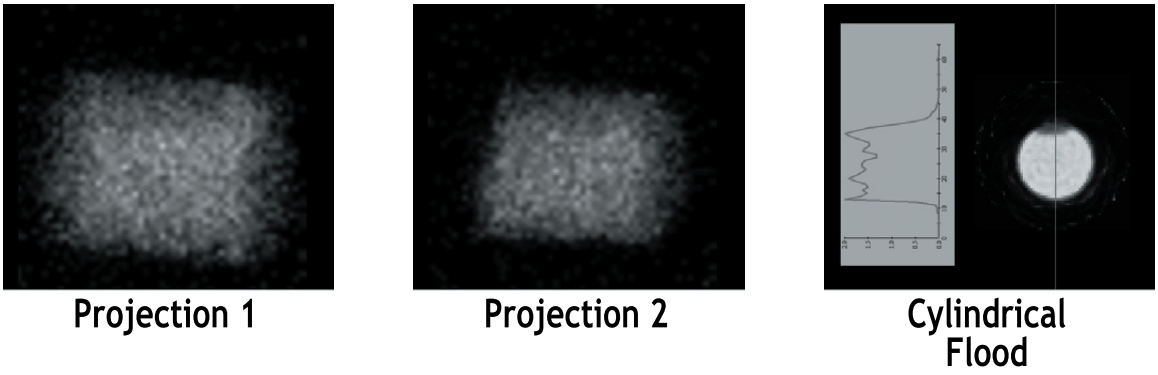

The area of apparent low activity at the top of the tank in the tomogram is again caused by the presence of a small air bubble within the tank. The efficacy of the uniformity correction can be visualized by the smooth activity distribution throughout the flood tank. A poor uniformity correction would produce light and dark rings in the reconstructed images, a feature which is lacking in our reconstruction. In addition, the features of the reconstructed image match those of the phantom which was imaged: uniform activity throughout the phantom, except in the presence of a small bubble which is visible at the top of the phantom. Attenuation correction was not performed in this experiment.

To verify that my code was sufficient to generate images of localized uptake as well, a similar experiment using hematocrit tubes filled only with ^{99m}Tc ($Na^{99m}TcO_4$) were

performed. Shown below are the resultant tomograms produced by my code and a line profile through one of the hematocrits for each energy window. In addition, it was noted that there is some downscatter from the ^{99m}Tc signal into the ^{125}I energy window, enough to form a ghost image. The issue of this crosstalk and its sources will be discussed in the next chapter.

Figure 15: Hematocrit Tomograms and Line Profiles

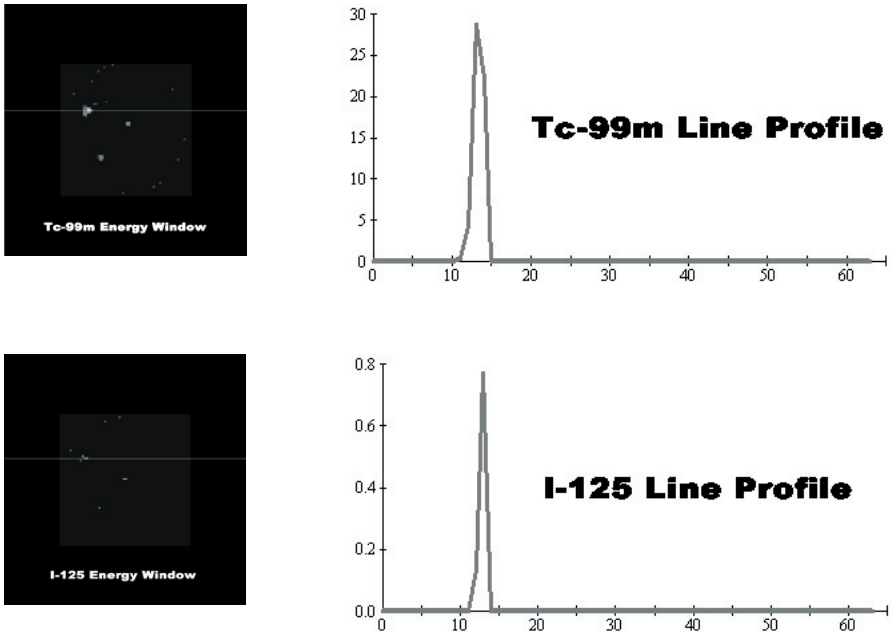

V. Discussion

The format of the raw list-mode data from the X-SPECT system has been successfully decoded. Custom IDL and C# code has been generated to process this list-mode data and to produce projection data which can be reconstructed using algorithms developed by Andrew Hwang. The code developed here assumes that the raw data in each projection file are stored as signed integers, with each functional unit of data comprised by a group of four consecutive integers. Most number groups represent a photon interaction with the

scintillator crystal, but some groups represent a time stamp or a trigger from and external source, such as an electrocardiogram (ECG) monitor. No data from the file is processed until a time/ECG stamp is encountered in the data. Then the reading frame for a list-mode data acquisition is determined by this first time/ECG stamp encountered in the raw file. All subsequent data is processed using this reading frame unless an error occurs (as evidence by a nonintegral multiple of four entries between time stamps) or the end of the file is reached. If an error occurs, all of the data for the preceding millisecond is discarded and the reading frame is reset to that of the subsequent time stamp. Most errors appear to be caused by operator shifting the focus from one window to another during data acquisition.

Anger logic is used to transform data corresponding to photons into physical locations of photon interaction with the detector scintillator. Large number of interactions corresponding to an individual pixel are collected and a spectrum is generated from the data. Then an energy calibration value is calculated for each pixel by smoothing the histogram with a running average and taking the ratio of the known photopeak to the peak raw value, producing a calibration factor with units of keV/(raw detector unit). This method assumes that the function mapping raw units to keV may be approximated by a linear function with intercept zero, at least in the [-10%, +15%] energy window surrounding the ^{99m}Tc 140-keV photopeak. Although this method produces images which may be corrected for uniformity and radiative decay, and which may be reconstructed tomographically, it is acknowledged that a more sophisticated method for energy calibration, possibly including corrections for noise and nonlinear dependence of energy (keV) on raw detector output may be developed

and implemented. However, at this juncture it is felt that the results here are acceptable, and as such this methodology will continue to be used throughout the remaining chapters of this work. In addition, the addition of multiple calibration points, especially that of the volatile and long-lived ^{125}I, complicates daily use of the methods developed here. The utility of a simple calibration involving just a single calibration point and a well-behaved ^{99m}Tc isotope is another practical reason to leave the methodology the way it is presented here. After all, if this procedure is too complicated for routine use, it is unlikely to benefit the science as a whole.

Finally, some crosstalk between the two isotopes was noted, specifically crosstalk from ^{99m}Tc into the ^{125}I image was observed. This issue of crosstalk, which occurs during the simultaneous acquisition of data from two radioisotopes, is explored further in the next chapter.

VI. References

1. Hasegawa BH, Iwata K, Wong KH, Wu MC, Da Silva AJ, Tang HR, Barber WC, Hwang AH, Sakdinawat AE. *Dual-modality imaging of function and physiology.* Acad Radiol. 2002 Nov;9(11):1305-21

2. Hasegawa BH, Wong KH, Iwata K, Barber WC, Hwang AB, Sakdinawat AE, Ramaswamy M, Price DC, Hawkins RA. *Dual-modality imaging of cancer with SPECT/CT.* Technol Cancer Res Treat. 2002 Dec;1(6):449-58

3. Cherry SR, Sorenson J, Phelps M. *Physics in Nuclear Medicine.* Saunders; 3 edition (July 18, 2003)

4. Griffiths D. *Introduction to Electrodynamics.* Benjamin Cummings; 3rd edition (December 30, 1998)

Chapter 3

Dual-Isotope ^{99m}Tc / ^{125}I Phantom Studies in the X-SPECT

I. Introduction

In medically-oriented single photon emission computed tomography (SPECT) studies, there is often the need to also quantitate the correlation between the uptake of one radionuclide with that of another[1]. In the preclinical environment, many SPECT studies use small animals such as mice and rats as disease models. Two commonly available radionuclides, ^{99m}Tc and ^{125}I, lend themselves to small animal studies by virtue of their relative ease of availability and low cost. Unfortunately at the present, many small animal SPECT systems are sold without much software dedicated to the area of dual-isotope imaging. Therefore, it is the focus of this chapter to explore and develop the abilities of the X-SPECT microSPECT/microCT imaging system for technetium-99m (^{99m}Tc) / iodine-125 (^{125}I) dual-isotope studies. In addition, we will characterize the crosstalk between the two isotopes and evaluate several methods of correction: isotope ratio limitation, energy windowing, subtraction, and iterative reconstruction techniques.

II. Background

In medically-oriented fields, there is often the need to not only quantitate the uptake of a given radionuclide within the body, but to also quantitate the correlation between the uptake of one radionuclide with that of another. This is the case in studies of related physiological factors such as the relationship of cardiac perfusion to cardiac innervation;

it is also the case in pharmaceutical efficacy trials, such as those in which we wish to determine the effect and location of uptake of a new drug on the bloodflow supplied to a tumor. Because many of these types of studies will be undertaken in small animals, there is therefore a role for the development and improvement of simultaneous dual-isotope techniques in the microSPECT environment. Although correlative information can be obtained indirectly from serial pharmaceutical measurements of uptake of single tracer molecules, biological and medical studies can benefit from the direct measurement of the relative amounts of uptake of two or more radionuclide tracers in the same subject and at the same point in time. Simultaneous data acquisition techniques allow researchers to obtain data that is unbiased due to variations between individuals, and has the added benefit of reducing the cost of the study in terms of the number of subjects required and the amount of time needed to take measurements from each of them. In particular, studies involving etiology or pathophysiology, in which it is the relationships between biological entities of interest that are the main focus, will benefit from the simultaneous acquisition of two types of data in a single organism.

II.I Introduction to Radionuclides

SPECT tracers employ radionuclide labels as imaging agents. Radionuclides are unstable isotopes of elements. This instability is often produced by an imbalance in the ratio of protons to neutrons in the nucleus of the radioactive atom. Often an imbalance of this type results in a state of increased energy relative to the atom's nonradioactive counterpart. If permitted, the atom will eventually evolve from its high-energy state to a lower energy state via rearrangement of its nuclear composition and release of excess energy in the form

of radiation; a reaction of this type is interesting to the field of nuclear medicine when the excess energy, called the transition energy, can be collected by an imaging system in the form of a high-energy photon.

By nature, the assessment of meaningful physiological correlations using radionuclide probes often necessitates the acquisition of two distinct types of data at a single point in time. Nuclear medicine, as we saw in the last chapter, lends itself to energy discrimination as a means of differentiation between two simultaneously acquired sets of data. In order to perform this discrimination in practice, however, it is desirable to first understand the mechanism of gamma ray production by radionuclides and the mechanism of data acquisition in a modern gamma camera. We will begin with the discussion of ^{125}I and ^{99m}Tc, two radioisotopes which are often used to label physiological molecules of interest.

II.II Choice of Radionuclides for Dual-Isotope Studies

Two commonly available radionuclides, technetium-99m (^{99m}Tc) and iodine-125 (^{125}I) isotopes, were chosen for the investigation of simultaneous data acquisition via SPECT imaging because they are relatively cheap and easy to obtain, exhibit chemistry amenable to labeling a variety of substances, and because they can be used in small animals, which are models of choice in the study of human disease.

II.III Choice of ^{99m}Technetium (^{99m}Tc)

^{99m}Tc is one of the most common radioisotopes used for medical and biological measurements today. In particular, ^{99m}Tc-labeled pharmaceuticals have been found to be

reliable markers of blood flow to a tissue (perfusion)[2]. This important property translates to many thousands of clinical assessments of heart and brain viability via myocardial and cerebral perfusion studies. In addition, ^{99m}Tc-labeled pharmaceuticals are also used in oncological evaluations, due to their tendency to accumulate in tissues which exhibit high levels of metabolic activity.

Figure 16: ^{99m}Tc Decay Scheme

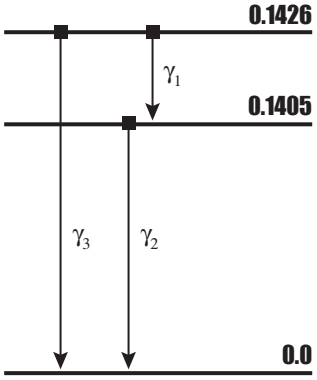

^{99m}Tc is a radioisotope which exists in a relatively long-lived metastable state; it has a half-life of 6.02 hours, during which it decays primarily by isomeric transition. The most common outcome of this is the emission of a 140-keV gamma ray, which may be used for imaging.

Table 1: ^{99m}Tc Decay

Radiation	y $(Bq \cdot s)^{-1}$	E (MeV)
ce-M, γ 1	9.14×10^{-1}	1.749×10^{-3}
ce-N^{+}, γ 1	7.57×10^{-2}	2.174×10^{-3}
ce-K, γ 2	8.79×10^{-2}	1.194×10^{-1}
ce-L_1, γ 2	9.67×10^{-3}	1.374×10^{-1}
ce-L_2, γ 2	6.10×10^{-4}	1.377×10^{-1}
ce-L_3, γ 2	3.01×10^{-4}	1.378×10^{-1}
ce-M, γ 2	1.92×10^{-3}	1.400×10^{-1}
ce-N^{+}, γ 2	3.71×10^{-4}	1.405×10^{-1}
ce-K, γ 3	6.91×10^{-3}	1.216×10^{-1}
ce-L_1, γ 3	1.17×10^{-3}	1.396×10^{-1}
ce-L_2, γ 3	2.43×10^{-4}	1.399×10^{-1}
ce-L_3, γ 3	7.40×10^{-4}	1.400×10^{-1}
ce-M, γ 3	4.19×10^{-4}	1.422×10^{-1}

Table adapted from Cherry, Sorenson, and Phelps[3].

II.IV Choice of ^{125}Iodine (^{125}I)

In contrast to ^{99m}Tc, ^{125}I is not commonly used in a clinical setting due to the high attenuation in tissue of its low energy emissions. However, this is not a large limitation for small animal imaging, in which there is comparatively little tissue to attenuate the signal. In addition, low cost, long half life, and ready availability of ^{125}I make it an attractive label for research purposes. Moreover, its use can easily be transitioned to the clinic with the use of the high-energy emitting isotope ^{123}I.

Figure 17: ^{125}I Decay Scheme

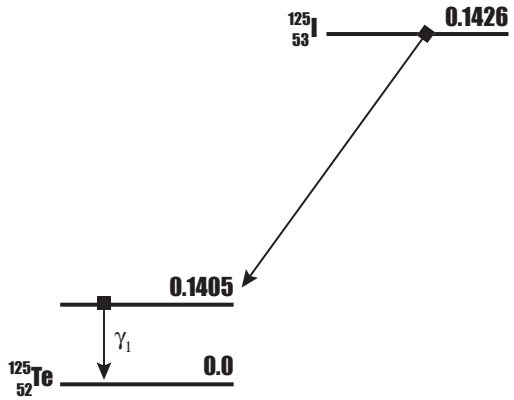

^{125}I decays by electron capture. It has a relatively long half life of 60.14 days, and it emits gamma rays which have an average energy of around 27.5 keV.

Table 2: ^{125}I Decay

Radiation	y $(Bq \cdot s)^{-1}$	E (MeV)
γ 1	6.67×10^{-2}	3.549×10^{-2}
ce-K, γ 1	8.03×10^{-1}	3.678×10^{-2}
ce-L_1, γ 1	9.52×10^{-2}	3.055×10^{-2}
ce-L_2, γ 1	7.64×10^{-3}	3.088×10^{-2}
ce-L_3, γ 1	1.91×10^{-3}	3.115×10^{-2}
ce-M, γ 1	2.09×10^{-2}	3.467×10^{-2}
ce-N^+, γ 1	4.96×10^{-3}	3.549×10^{-2}
$K\alpha_1$, X-ray	7.41×10^{-1}	2.747×10^{-2}
$K\alpha_2$, X-ray	3.98×10^{-1}	2.720×10^{-2}
$K\beta_1$, X-ray	1.40×10^{-1}	3.100×10^{-2}
$K\beta_2$, X-ray	4.30×10^{-2}	3.171×10^{-2}
$K\beta_3$, X-ray	7.20×10^{-2}	3.094×10^{-2}
$K\beta_5$, X-ray	1.44×10^{-3}	3.124×10^{-2}

Table adapted from Cherry, Sorenson, and Phelps[3].

III. Methods

III.I Demonstration of Crosstalk Between ^{99m}Tc and ^{125}I Emissions

As another example of the utility of this technique, a drug delivery phantom was constructed. A dual isotope experiment using ^{99m}Tc to represent a perfusion tracer and ^{125}I to represent a radiolabeled drug which affect perfusion was performed using two 2-mL microcentrifuge tubes and one 50-mL conical centrifuge tube were used in this experiment. Microcentrifuge tubes contained 0.1 mCi of ^{125}I *meta*-iodobenzylguanidine (mIBG) in 1.5 mL water (~0.1 mCi/mL) were employed to simulate localized uptake of the drug within a given tissue, and the 50-mL conical was filled with 45 mCi ^{99m}Tc sodium pertechnetate in 45 mL water (~1 mCi/mL) to simulate generalized perfusion throughout the tissue. The microcentrifuge tubes were vortexed to ensure mixing and then placed inside the conical tube, which was also vortexed to ensure mixing of the sodium pertechnetate solution. The conical tube was then placed on its side in the X-SPECT scanner, and 64 SPECT projections were acquired using a 1.0 mm pinhole, 90 sec/projection, and a radius of rotation of 4.80 cm, yielding approximately 573,000 counts per projection. Projection data were processed, corrected, and reconstructed as described in Chapter 2.

III.II Measurement of Crosstalk Between ^{99m}Tc and ^{125}I Emissions

To quantitate the downscatter from ^{99m}Tc to ^{125}I, a phantom experiment was conducted. 1.5 mL microcentrifuge tubes were filled with solutions of ^{99m}Tc $Na^{99}mTcO_4$. Activity concentrations in each microcentrifuge tube varied from 1 mCi/mL to 10 mCi/mL. The total volume of liquid in each phantom was brought up to 1.0 mL using tap water and

a pipet, and each tube was vortexed to ensure adequate mixing of radionuclide samples. Microcentrifuge tubes were placed in the patient bed of the imaging system and secured with a cardboard coaster for imaging. SPECT scans were acquired at 4 minutes, 98 minutes, 229 minutes, 332 minutes, and 1221 minutes post-mixing to provide a range of activity concentrations for measurement. SPECT scans were acquired with a 1.0 mm pinhole collimator and 64 projections over 360 degrees, with approximately 500,000 counts acquired per projection (approximately 90 seconds per projection). Projection data were processed, corrected, and reconstructed as described in Chapter 2.

III.III Monte Carlo Simulation of Detector Response to ^{99m}Tc and ^{125}I

To add insight into potential sources of crosstalk interactions, the detector response of the X-SPECT to ^{99m}Tc and ^{125}I was first simulated using Monte Carlo methods. Monte Carlo simulations were obtained using an application created with the package Geant4, version Geant4.8.0.p01. Physics processed were configured for nuclear medicine studies using the low-energy options for scattering and energy loss. For each simulation, one million photons were emitted isotropically from a point source located 1.5 cm from the front face of a sodium iodide detector. Potential processes which could give rise to crosstalk in an Anger camera were investigated in the following order: pixelation of the sodium iodide scintillator, decreasing the thickness of the sodium iodide scintillator, the presence of glass behind the scintillator (e.g., light guide, front face of the photomultiplier tube), presence of lead shielding behind the Anger camera, presence of lead shielding in the rest of the imaging apparatus, and the presence of scattering media surrounding the photon source. The pixelation effect in the X-SPECT's photomultiplier tube detector was simulated using

a sensitive detector associated with an 11.6 cm x 11.6 cm slab of sodium iodide which was pixelated into between 1 and 2916 equally-sized equally spaced crystals with Teflon reflectors between the pixels. The total cross-sectional area of the Teflon reflectors in each pixelation was fixed at 17.633% of the total detector area, which matches that of our X-SPECT detector. The effect of detector thickness was tested using a detector pixelated into 54 x 54 pixels; detector thickness ranged from 1-6 mm. The addition of a slab of borosilicate glass and then of lead behind the scintillator was employed to simulate the effect of backscatter off the photomultiplier tube face or lead detector housing in the presence of a 54 x 54-pixel, 6-mm-thick detector. Similarly, the addition to the setup of a slab of lead on the side of the photon source opposite that of the detector was simulated to evaluate the effect of lead shielding surrounding the imaging apparatus. Finally, scattering in the presence of animal or other tissue was simulated with the addition of a sphere of water of radius ranging from 0.00001 cm to 1.5 cm centered on the point source to the existing geometry.

III.IV Correction of ^{99m}Tc Scatter Into ^{125}I Energy Window

Several methods were investigated to correct the crosstalk between our isotopes.

The first and simplest method investigated is isotope ratio limitation. This method is very accessible to the experimenter because the amount of injected activity can easily be adjusted at the time of delivery. Because the major source of crosstalk was found to be ^{99m}Tc photons appearing in the ^{125}I energy window, we measured the crosstalk as a function of ^{99m}Tc concentration. We then employed this information to determine the maximum

concentration ratio of ^{99m}Tc to ^{125}I which would produce an error in ^{125}I of 5% or less in the projection data. Following the manufacturer's recommendation, ^{125}I photons were considered "good" (unscattered) if their calculated energy was measured within -66% to +66% of the 30-keV ^{125}I photopeak. This method was tested with another microcentrifuge tube phantom composed of three microcentrifuge tubes. The first microcentrifuge tube contained 0.59 mCi ^{99m}Tc, the second contained 0.79 mCi ^{99m}Tc and 0.113 mCi ^{125}I, and the third contained 0.112 mCi ^{125}I. The volume of each microcentrifuge tube was brought up to 1.5 mL using tap water and a pipet, and each tube was vortexed to ensure good mixing of the contents. 19 sequential 1-hour dynamic SPECT projections were acquired with a 1.0 mm pinhole collimator to produce a range of activities for evaluation.

A subtraction method was developed next. In this method, a simple mathematical correction was implemented to correct the downscatter from ^{99m}Tc into the ^{125}I energy window. Using the measured value of the downscatter, crosstalk activity in the ^{125}I projection images was suppressed by subtracting a fraction of the counts in the ^{99m}Tc projection image, weighted by the expected downscatter distribution of counts, from the ^{125}I projection images. Again following the manufacturer's recommendation, ^{125}I photons were considered "good" (unscattered) if their calculated energy was measured within -66% to +66% of the 30-keV ^{125}I photopeak. The above microcentrifuge tube data was used to test this idea.

Energy windowing was investigated next. We investigated the option of narrowing the ^{125}I energy window to improve the ratio of ^{99m}Tc photons to ^{125}I photons within it. We first investigated narrowing the energy window symmetrically from the original ±66% to ±50%, ±40%, ±30%, ±15%, ±10%, and ±5%. Next, due to the asymmetry in distribution

across the energy window observed in the Monte Carlo estimation of downscatter, we also chose to narrow the window asymmetrically. Energy windows including all asymmetrical combinations of the above values were studied for this purpose. This method was tested using images of a uniform flood filled with either ^{99m}Tc or ^{125}I. The mean number of counts obtained in each energy window along with the variance was tabulated for each energy window and the values for each isotope were compared.

IV. Results

IV.I Demonstration of Crosstalk Between ^{99m}Tc and ^{125}I Emissions

Tomographic SPECT scans from our drug delivery phantom are shown below. In the first

Figure 18: Drug Delivery Phantom

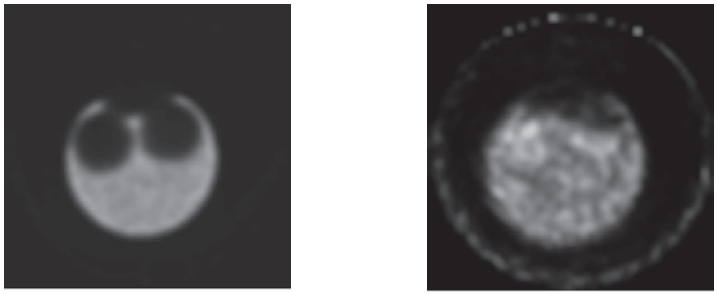

image, which shows the ^{99m}Tc energy window, the area corresponding to that occupied by ^{99m}Tc activity is well defined. Most of the cross section through the 50-mL conical is uniformly bright, and there are two "holes" near the top of the conical which correspond to the microcentrifuge tubes containing ^{125}I activity. However, the ^{125}I energy window does not exhibit such clean results. Although there is only ^{125}I activity present within the microcentrifuge tubes, the ^{125}I energy window image shows activity distributed throughout

the 50-mL conical. This indicates that the presence of ^{99m}Tc may obscure the localization and quantitation of ^{125}I activity during the course of a dual isotope experiment. In our hypothetical study of drug delivery, the localization of the drug uptake would be lost, and hence the measurement of drug efficacy could suffer due to this effect.

IV.II Measurement of Crosstalk Between ^{99m}Tc and ^{125}I Emissions

Tomograms of the microcentrifuge tubes, line profiles through the tomograms, and measurements quantitating the downscatter from ^{99m}Tc into the ^{125}I energy window are shown below. Although no ^{125}I was used in this experiment, an image is still obtained if data is collected using the ^{125}I energy window. It was also noted that the crosstalk was localized to areas where ^{99m}Tc activity was present, suggesting that detector scatter was the likely crosstalk mechanism. However, the low number of photons which contributed to the crosstalk are evidenced by the increased noise and lack of microcentrifuge tube definition in the ^{125}I energy window image.

Figure 19: Crosstalk Illustration

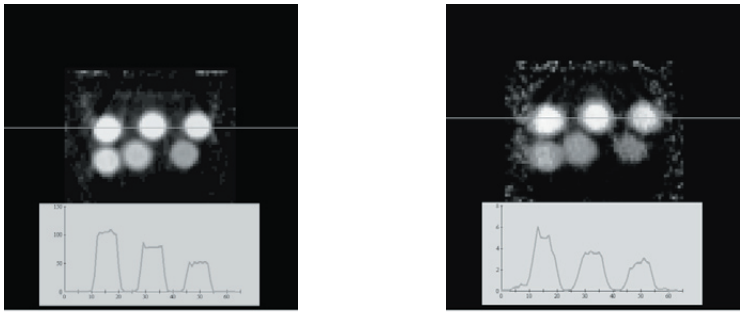

In addition, as confirmed by the Monte Carlo simulations, the downscatter is linear with

respect to ^{99m}Tc activity concentration. Moreover, if we fit the data to a line, we find that

$$^{125}\text{I counts/voxel} = 0.50 * [^{99m}\text{Tc}]$$

where $[^{99m}Tc]$ is in units of mCi/mL. If we compare this value to

$$^{99m}\text{Tc counts/voxel} = 10.9 * [^{99m}\text{Tc}]$$

where $[^{99m}Tc]$ is again in units of mCi/mL, we find that the measured crosstalk from ^{99m}Tc to the ^{125}I energy window is 4.6% of the total number of photons emitted. Alternatively, if the activity concentrations of ^{99m}Tc and ^{125}I in a tissue are equal, then 4.6% of the photons detected in the ^{125}I window should actually have been detected as ^{99m}Tc activity.

Figure 20: Quantitation of Crosstalk

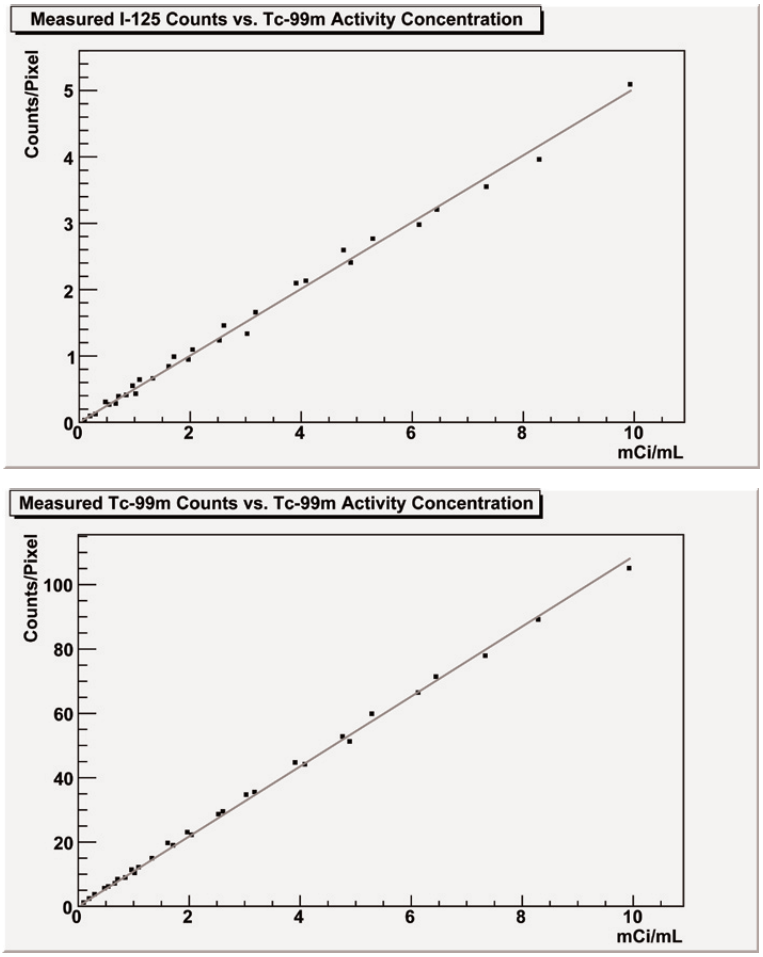

IV.III Monte Carlo Simulation of Detector Response to ^{99m}Tc and ^{125}I

Insight into the physical mechanisms of the crosstalk between ^{99m}Tc and ^{125}I can be found through the use of Monte Carlo simulations. To provide a baseline measurement, a control simulation was performed using a point source and an 11.6 cm x 11.6 cm sodium iodide detector slab 0.6 cm thick, which matches the dimensions of our gamma camera. In this experiment, 3.3% of the ^{99m}Tc photons are recorded in the ^{125}I energy window, which is a little less than the measured 4.6% from our phantom experiments. All of the ^{125}I photons detected were present in this window.

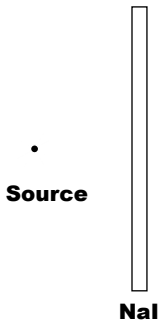

Figure 21: Initial Simulation

The effect of detector pixelation on the acquired spectra was tested next. The above control case scintillation was divided into a number of ranging from pixels from 1 large pixel up to 2916 smaller pixels separated by Teflon spacers. As shown, variation in the number of pixels from 1 (black) to 9 (green) to 100 (blue) to 2916 (red) causes an increase in the amount of scattering observed in the ^{99m}Tc spectra, although the total cross-sectional area of the crystal was held constant. As shown in the final spectrum below, energy deposition due to scattering in the Teflon spacers between the crystals results in photons detected in the sodium iodide which exhibit energies ranging from approximately 95 keV to 140 keV. In addition, iodine escape peaks are present within this range at approximately 110 keV. Scattering in the sodium iodide crystals themselves results in energies deposited between 0 keV and 45 keV, rasing the percentage of ^{99m}Tc detected in the ^{125}I window to 4.5%. In contrast to the ^{99m}Tc case, increasing the number

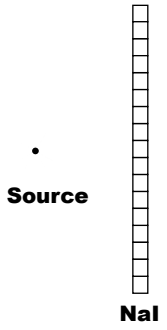

Figure 22: Pixelation

of pixels from 1 to 2916 causes a small increase in the amount of scattering observed in the ^{125}I spectra, but does not affect the number of photons detected. In these and in all spectra which follow, the height of the primary photopeaks at 140 keV and 30 keV have been truncated to demonstrate these effects more clearly.

Figure 23: Pixelation Spectra

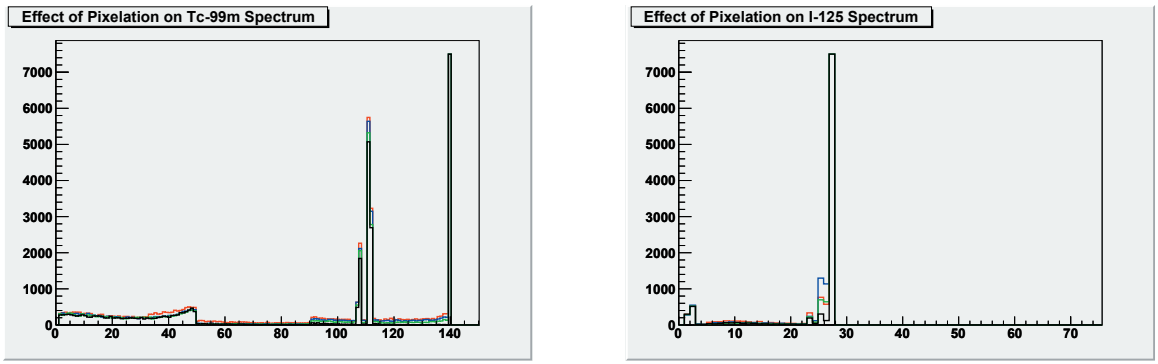

Next, the effect of reducing the thickness of the sodium iodide scintillator was investigated. Using the 54 x 54 pixelated detector configuration described above, the thickness of the scintillator was reduced from 0.6 mm (black) to 0.4 mm (green) to 0.2 mm (blue) to 0.1 mm (red). In the case of ^{99m}Tc, decreasing the detector thickness produced fewer detected photons in the range of 95-140 keV and approximately the same number of photons in the range of 0-45 keV. Almost no effect was demonstrated in ^{125}I spectra.

Figure 24: Scintillator Thickness

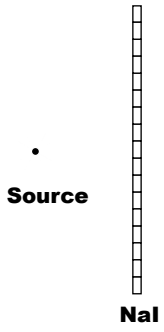

Figure 25: Scintillator Thickness Spectra

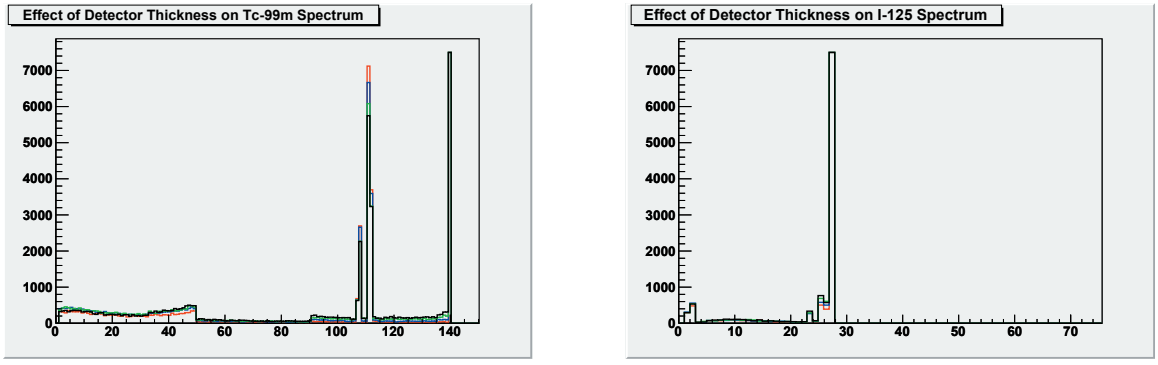

The effects of backscatter off various parts of the Anger camera were investigated next. First, borosilicate glass was placed 0.2 cm behind our 0.6-mm-thick sodium iodide detector which was pixelated into 54 x 54 pixels. The thickness of the glass was increased from 0.0 cm (not present, black) to 0.2 cm (green) to 0.5 cm (blue) to 1.0 cm (red). In the ^{99m}Tc spectra, the presence of borosilicate glass representing the photomultiplier tube is primarily manifested as an increase in the backscattering component of the spectrum, which lies in the range of 95-118 keV. A 24% increase in the number of downscatter photons in the ^{125}I energy window was also produced, which is 4.3% of the photons present in the photopeak. Again, the ^{125}I spectrum is largely unaffected.

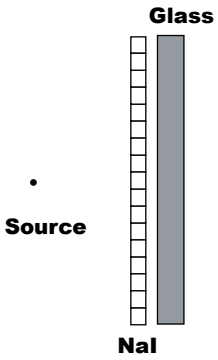

Figure 26: Borosilicate Glass

Figure 27: Borosilicate Glass Spectra

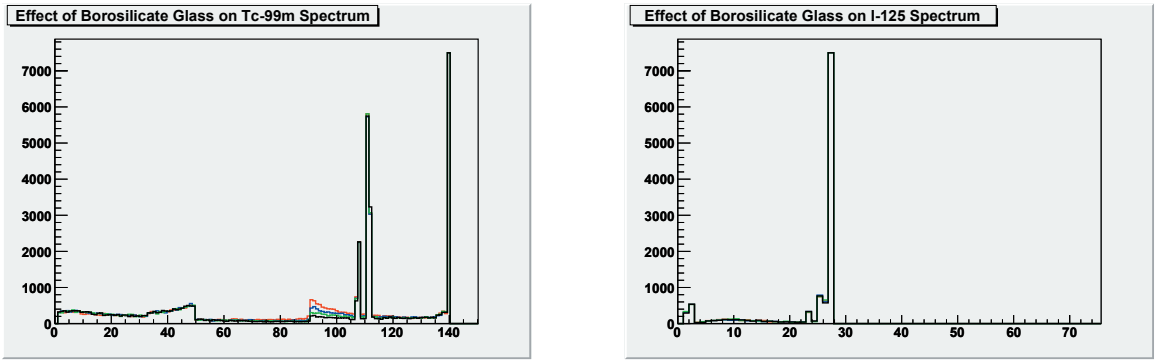

The addition of borosilicate glass was followed by a secondary addition of a lead plate located behind the glass to simulate the lead bucket which shields the detector itself. This plate was placed 0.5 cm behind the borosilicate glass, and it thickness was increased from 0.1 cm (black) to 0.2 cm (green) to 0.5 cm (blue) to 1.0 cm (red). This produces additional peaks in the ^{99m}Tc spectrum around 80 keV which correspond to lead x-rays. Once again, the effect of lead behind the borosilicate glass on the ^{125}I spectrum is minimal in these simulations.

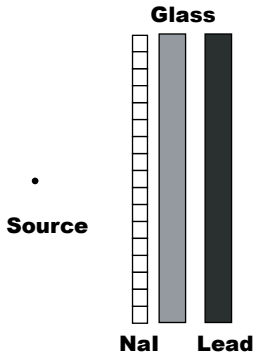

Figure 28: Detector Shielding

Figure 29: Detector Shielding Spectra

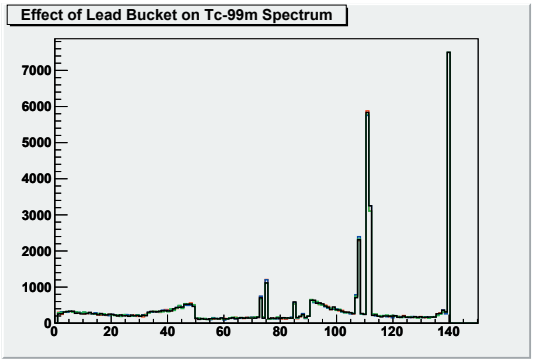

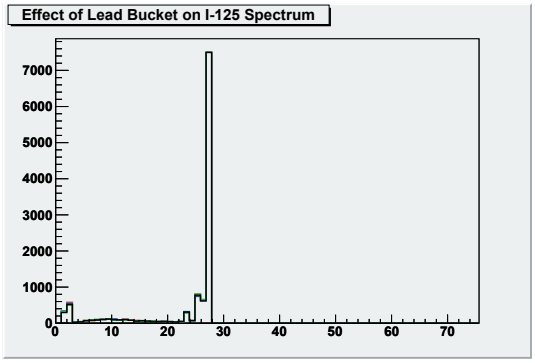

The effect of lead shielding present in the rest of the imaging system was investigated also. An additional lead plate was placed 1.5 cm from the point source on the side of the source opposite the detector. The thickness of the plate was increased from 0.1 cm (black) to 0.2 cm (green) to 0.5 cm (blue) to 1.0 cm (red). Again, the addition of lead produces an increase in the x-ray peaks near 80 keV. Moreover, these 80 keV photons produce an iodine

Figure 30: System Shielding

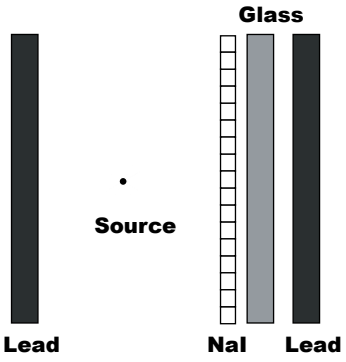

escape peak from the sodium iodide detector in the spectrum near 50 keV, increasing the crosstalk to 5.8%. The ^{125}I spectrum also shows the presence of a peak around 10 keV, which is due to a lead x-ray. This leads to a 2% increase in the ^{125}I counts recorded from the ^{125}I source.

Figure 31: System Shielding Spectra

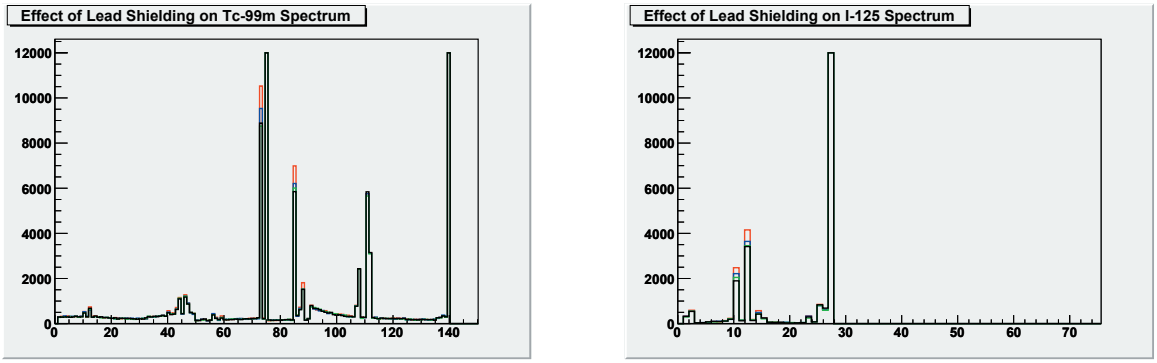

Finally, the effect of scattering in the object of interest on the crosstalk between ^{99m}Tc and ^{125}I was investigated. The radius of the water sphere was increased from 0.0 cm to 1.0 cm. Scattering of ^{99m}Tc photons in the object produces additional counts in the detector with energies ranging from approximately 95 keV to 140 keV (single-scattering events) and from 55 keV to 95 keV (multiple scattering events). Crosstalk into the ^{125}I energy window is increased to 6.3%. In addition, scattering of ^{125}I photons results in a 5% reduction in measured counts.

Figure 32: Scattering

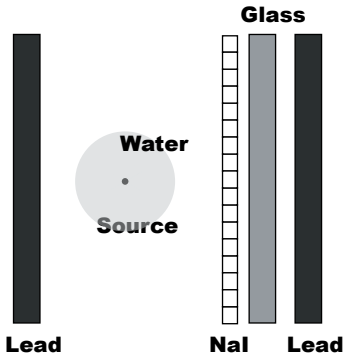

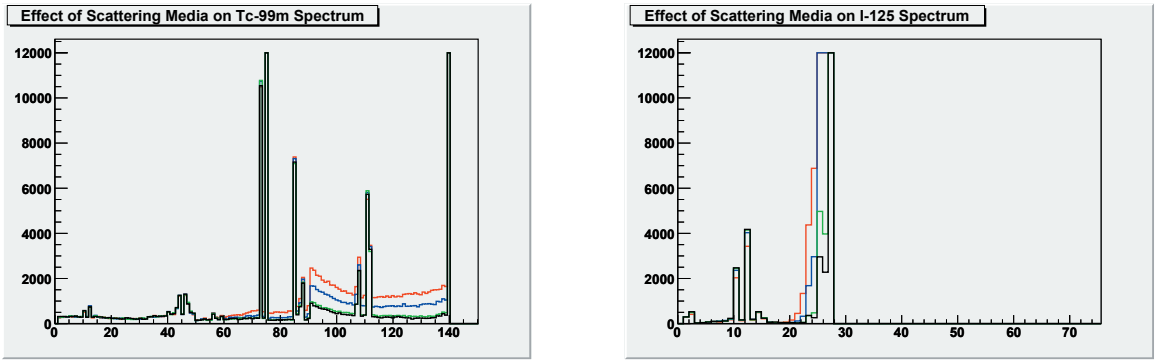

Figure 33: Scattering Spectra

To summarize, the results of these simulations are tabulated for both ^{99m}Tc and ^{125}I below.

IV.IV Summary of Monte Carlo Simulation Results For ^{99m}Tc

Table 3: Simulation Results in the ^{99m}Tc Energy Window

Additional Simulation Factors Source: Tc-99m Photons Emitted at 140 keV	Number of Photons Recorded in 10-50 keV Window	Percentage of Control Downscatter	Percentage of Primary Photopeak
Control	9789	100 %	3.3 %
Pixelate Detector Slab Into 54 x 54 Pixels	12496	128 %	4.5 %
Reduce Detector Thickness to 0.1 cm	9869	101 %	13.2 %
Add 1-cm Thick Borosilicate Glass Behind Scintillator	12105	124 %	4.3 %
Add 1-cm Thick Lead Shielding Behind Borosilicate Glass	12360	126 %	4.4 %
Add 1-cm Thick Lead Shielding Behind Point Source	16078	164 %	5.8 %
Add 1-cm Radius Water Scattering Media Around Point Source	15607	159 %	6.3 %

IV.V Summary of Monte Carlo Simulation Results For ^{125}I

Table 4: Simulation Results in the ^{125}I Energy Window

Additional Simulation Factors Source: I-125 Photons Emitted at 27.5 keV	Number of Photons Recorded in 10-50 keV Window	Percentage of Control Case	Percentage of Dual-Isotope Total Assuming Equal Injection Activities
Control	359556	100 %	97.3 %
Pixelate Detector Slab Into 54 x 54 Pixels	365781	102 %	96.6 %
Reduce Detector Thickness to 0.1 cm	335667	93.4 %	97.1 %
Add 1-cm Thick Borosilicate Glass Behind Scintillator	366350	102 %	96.7 %
Add 1-cm Thick Lead Shielding Behind Borosilicate Glass	365532	102 %	96.6 %
Add 1-cm Thick Lead Shielding Behind Point Source	374046	104 %	95.7 %
Add 1-cm Radius Water Scattering Media Around Point Source	341568	95 %	95.4 %

The 6.3% crosstalk factor shown in the ^{99m}Tc results summary for an ideal Monte Carlo detector matches reasonably well with our actual gamma camera, which records a crosstalk factor of 4.6%. We attribute the difference in this case to other factors of our system which were not modeled, such as the shape of the pinhole collimator and the blurring due to the shaping electronics in our system. Alternatively, our physical detector could be slightly thicker than 6.0 mm, which could also easily explain this difference.

IV.VI Situations In Which a Crosstalk Correction Is Merited

Crosstalk from ^{99m}Tc activity into the ^{125}I energy window will be most pronounced when there is a large ratio of ^{99m}Tc activity to ^{125}I activity in a given volume of tissue. Sample ratios and the errors produced in ^{125}I quantitation are shown below.

Table 5: Simulation Results in the ^{99m}Tc Energy Window

Ratio of ^{99m}Tc to ^{125}I	Percent Error in ^{125}I Measurement
1 : 1	4.6 %
2 : 1	9.2 %
5 : 1	23 %
10 :1	46 %
25 : 1	115 %
50 : 1	230 %
100 : 1	460 %

This implies that a correction may be useful in situations that are likely to exhibit ratios of ^{99m}Tc to ^{125}I of 2 : 1 or greater. This will be verified in the next section.

IV.VII Correction of ^{99m}Tc Scatter Into ^{125}I Energy Window

Based on the Monte Carlo results and on the downscatter result, it was expected that the easiest and quickest method of reducing the downscatter would be simply to limit the amount of ^{99m}Tc activity relative to that of ^{125}I. In practice this is a good method of reducing the crosstalk because is it often quite easy for the experimenter to limit the amount of each radiotracer used at the time of injection. This experiment was performed to verify that the addition of ^{99m}Tc activity did not interfere with the detection of ^{125}I in the projection data. In each one-hour frame, a 510-pixel region of interest was drawn around each of the microcentrifuge tubes and the number of counts within the region of interest was totaled. As expected, the amount of ^{125}I counts detected in each projection does not appear to depend on the varying amounts of ^{99m}Tc activity present nearby, indicating that isotope ratio limitation is an effective means of limiting crosstalk in a dual-isotope experiment. Sample projections and a table summarizing the results are shown below.

Figure 34: Projection Data for Experimental Crosstalk Measurement

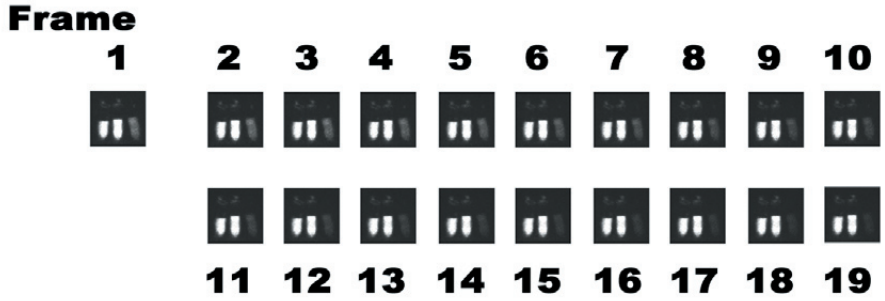

Table 6: Experimental Crosstalk Results

Frame	Tube #1: ^{125}I Only (Percentage of Counts Recorded in Left Tube Containing ^{125}I Only)	Tube #2: ^{99m}Tc + ^{125}I (Percentage of Counts Recorded in Left Tube Containing ^{125}I Only)	Tube #3 : ^{99m}Tc Only (Percentage of Counts Recorded in Left Tube Containing ^{125}I Only)
1	100 %	140.3 %	34.6 %
2	100 %	138.8 %	31.8 %
3	100 %	135.7 %	28.8 %
4	100 %	133.4 %	25.8 %
5	100 %	131.3 %	23.4 %
6	100 %	128.9 %	21.0 %
7	100 %	127.0 %	18.7 %
8	100 %	125.4 %	17.1 %
9	100 %	125.1 %	15.7 %
10	100 %	123.4 %	14.1 %
11	100 %	122.2 %	13.0 %
12	100 %	121.3 %	11.6 %
13	100 %	119.1 %	10.8 %
14	100 %	120.5 %	10.0 %
15	100 %	118.4 %	9.1 %
16	100 %	119.4 %	8.4 %
17	100 %	118.2 %	7.6 %
18	100 %	118.1 %	7.2 %
19	100 %	116.8 %	6.6 %

The above data were then corrected with a subtraction algorithm. Using the measured value of the downscatter (4.6%), crosstalk activity in the ^{125}I projection images was suppressed by subtracting a fraction of the counts in the ^{99m}Tc projection image, weighted by the expected downscatter distribution of counts, from the ^{125}I projection images. As shown, this suppresses 45-60% of the crosstalk, depending on the original amount of crosstalk.

Figure 35: Corrected Projection Data

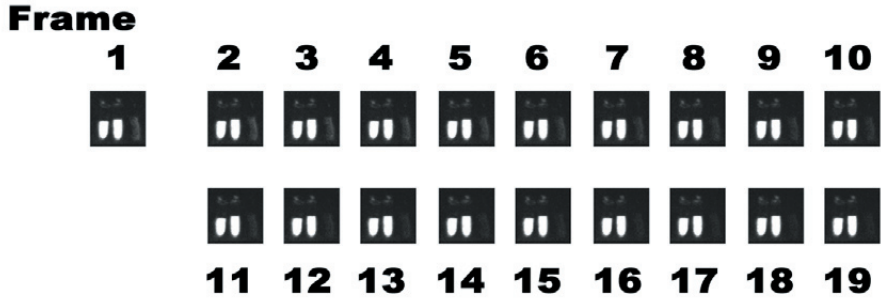

Table 7: Corrected Crosstalk Results

Frame	Tube #1: ^{125}I Only (Percentage of Counts Recorded in Left Tube Containing ^{125}I Only)	Tube #2: ^{99m}Tc + ^{125}I (Percentage of Counts Recorded in Left Tube Containing ^{125}I Only)	Tube #3 : ^{99m}Tc Only (Percentage of Counts Recorded in Left Tube Containing ^{125}I Only)
1	100 %	107.5 %	13.6 %
2	100 %	107.9 %	12.6 %
3	100 %	107.1 %	11.5 %
4	100 %	106.6 %	10.7 %
5	100 %	105.8 %	9.8 %
6	100 %	105.0 %	8.9 %
7	100 %	104.1 %	7.9 %
8	100 %	103.2 %	7.3 %
9	100 %	103.6 %	6.9 %
10	100 %	102.9 %	6.3 %
11	100 %	102.3 %	6.1 %
12	100 %	102.3 %	5.5 %

13	100 %	100.8 %	5.2 %
14	100 %	102.2 %	4.9 %
15	100 %	101.4 %	4.7 %
16	100 %	103.1 %	4.4 %
17	100 %	102.6 %	4.1 %
18	100 %	103.1 %	3.9 %
19	100 %	102.3 %	3.7 %

Next the dependence of crosstalk on energy window was investigated. Mean values for an image of a uniform flood are shown in the table below.

Table 8: Dependence of Crosstalk on Energy Window

Energy Window	^{125}I / ^{99m}Tc Count Ratio	Mean ^{125}I Counts / Pixel (% +66. -66 Window)	Mean ^{99m}Tc Counts / Pixel (% +66. -66 Window)	Std Dev ^{99m}Tc Counts / Pixel (% +66. -66 Window)
+5, -5	2.99	14.4 %	4.8 %	3.9 %
+5, -10	3.38	22.3 %	6.6 %	5.1 %
+5, -15	3.64	30.0 %	8.2 %	4.4 %
+5, -30	3.12	47.0 %	15.1 %	6.0 %
+5, -66	1.52	104.3 %	68.4 %	24.2 %
+10, -5	2.60	17.3 %	6.6 %	4.3 %
+10, -10	2.99	24.9 %	8.4 %	4.5 %
+10, -15	3.26	33.0 %	10.1 %	4.7 %
+10, -30	2.96	50.2 %	17.0 %	6.5 %
+10, -66	1.54	108.8 %	70.5 %	24.6 %
+15, -5	2.27	19.1 %	8.4 %	4.3 %
+15, -10	2.63	26.7 %	10.2 %	4.6 %
+15, -15	2.90	34.7 %	12.0 %	4.9 %
+15, -30	2.76	52.1 %	18.8 %	6.9 %
+15, -66	1.53	110.8 %	72.7 %	24.9 %
+30, -5	1.51	21.1 %	13.9 %	5.6 %
+30, -10	1.82	28.6 %	15.7 %	5.8 %
+30, -15	2.08	36.5 %	17.6 %	6.2 %
+30, -30	2.19	53.6 %	24.4 %	8.2 %
+30, -66	1.38	109.6 %	79.3 %	26.3 %
+66, -5	0.71	21.3 %	29.9 %	9.7 %
+66, -10	0.90	28.5 %	31.8 %	10.1 %
+66, -15	1.07	36.0 %	33.7 %	10.5 %
+66, -30	1.29	52.4 %	40.6 %	12.5 %
+66, -66	1.00	100.0 %	100.0 %	31.4 %

As shown above, increasing the width of the energy window increases the amount of downscatter observed. It is also notable that the dependence of downscatter on energy window is not symmetric with respect to positive and negative increases in width. For example, the +5%,-66% energy window contains 68.4% of the +66%,-66% downscatter photons, but the +66%,-5% energy window contains only 29.9% of those same photons, and a -66%,+30% window contains only 40.6%. This suggests that an asymmetrical energy window may be best for rejection of downscatter.

A similar trend may be observed in primary counts from ^{125}I. But by comparing the ratios of accepted counts for each isotope, it can be seen that an energy window of +15%,-30% appears to have the best properties. Approximately 50% of the ^{125}I photons are retained, and 80% of the downscatter from ^{99m}Tc is rejected.

Although the average number of counts per pixel appears to be more than 100% for some subsets, this is likely to be due to an artifact in the calculation of the mean value. Pixels which do not have enough counts to produce a peak in the energy spectrum above a certain threshold have their value set to zero in the image. This zero is not used in the calculation of the mean pixel value. Therefore, the average value may appear artificially high.

V. Discussion

Dual-isotope experiments using ^{99m}Tc and ^{125}I isotopes were performed on the X-SPECT MicroSPECT/CT imaging system, and custom software was developed to discriminate between data pertinent to each isotope on the basis of energy. Although a small amount of

downscatter from ^{99m}Tc to the ^{125}I energy window was detected, it was found that the level of crosstalk contamination could easily be limited through simple experimental procedures such as limitation of the amount of isotope used and adjustment of the ^{125}I energy window used during acquisition.

This methodology allows us to employ several commonly-used radiotracers to study interactions between biological entities of interest using simultaneous acquisition of data from two sources. For example, there are currently many ^{99m}Tc-labeled pharmaceuticals which can be used to measure perfusion and viability; one common such tracer is ^{99m}Tc-methoxybutylisonitrile (^{99m}Tc-sestamibi). We expect that most studies using these types of pharmaceuticals will exhibit widespread staining of many tissues, including the heart, most of which will uptake fairly large amounts of activity. Moreover, we expect that the activity concentration will also be relatively high in the heart, leading to short image acquisition times and good statistics within the images. This is one of the advantages of tracers such as ^{99m}Tc-sestamibi and is in part responsible for this drug's popularity in cardiac viability evaluations in the hospital.

In addition, ^{125}I is often employed as an experimental radiolabel for its cost and long half-life for preclinical studies in small animals. In our myocardial perfusion example, it is very possible that ^{125}I will be used to label an experimental pharmaceutical for drug/perfusion correlation tests in small animals. The methodology developed here will allow the correlation between drug uptake and perfusion to be studied in the same animal at the same time, lending strength to the conclusions which may be drawn from the data obtained.

We have characterized the crosstalk between ^{99m}Tc and ^{125}I in a small animal SPECT/CT imaging system. Although the energy difference between the emissions of the two radionuclides are quite different, we have characterized a small amount of crosstalk between them; we believe that the source of this crosstalk is Compton scattering in the sodium iodide scintillator employed in our detector. This error may easily be reduced through limitation of the amounts of isotopes used. However, we can envision a situation in which we would like to measure a low concentration of ^{125}I (the drug) in the presence of a relatively high concentration of ^{99m}Tc (the perfusion marker). Moreover, we expect that this type of scenario may be encountered as the field of molecular pharmacology develops and evolves. As such, we acknowledge that the most widely applicable crosstalk correction could be obtained with an iterative algorithm such as ML-EM.

At this time, due to the size of the uncorrected downscatter component (5%), the extra computing time necessary for advanced correction methods was deemed largely unnecessary although it may be warranted in extreme cases. Based on our analysis of the effects of isotope use limitation and energy window on crosstalk contamination of ^{125}I images, we instead recommend limiting the amount of ^{99m}Tc activity to less than the amount of ^{125}I activity and utilization of a +15%,-30 energy window to reject downscatter while still maintaining acceptable numbers of counts in the ^{125}I image. However, in a count-starved experiment, a window of +66%,-66% may be used to boost the count statistics at the expense of downscatter contamination in the image.

VI. References

1. Slart RH, Bax JJ, van Veldhuisen DJ, van der Wall EE, Dierckx RA, Jager PL. *Imaging techniques in nuclear cardiology for the assessment of myocardial viability.* Int J Cardiovasc Imaging. 2006 Feb;22(1):63-80

2. Jain D. *Technetium-99m labeled myocardial perfusion imaging agents.* Semin Nucl Med. 1999 Jul;29(3):221-36

3. Cherry SR, Sorenson J, Phelps M. *Physics in Nuclear Medicine.* Saunders; 3 edition (July 18, 2003)

Chapter 4

Preparations for *In Vivo* Imaging Studies

I. Introduction

As discussed in Chapter 1, in addition to our interest in dual-isotope studies, we will also discuss the modification of SPECT/CT imaging hardware and equipment which will allow us to test our methodology ***in vivo*** and which will enhance the quality and accuracy of perfusion-related measurements by better accommodating the physiological needs of small animals. Although the imaging community has done a considerable amount of work in specializing SPECT and CT imaging hardware to be compatible with sizes relevant to small animals[1-4], much of the current focus has been on the imaging hardware itself (such as enhanced detector systems); correspondingly less work has been done in areas pertaining to support of the animal's physiology during the course of data acquisition. For example, many imaging systems are available without capabilities for maintenance of an animal under anesthesia; furthermore, maintenance of anesthesia often requires that the animal's vital signs be monitored and adjusted to ensure that physiology relevant to the study is not disrupted. This is an area which could be improved in imaging systems. Because this physiological monitoring will almost certainly be an important consideration for any functional imaging measurement of a biological process, we will investigate the incorporation of anesthesia, physiological monitoring systems, and imaging agent delivery systems within the microSPECT/CT imaging environment. These additional capabilities will decrease the effect of the imaging system on the physiology under study and make

the data acquired more comparable to that acquired with more conventional methodology. This increased reproducibility and comparability will have the advantage of increasing the utility and relevance of small animal imaging measurements to the medical community.

In addition, we will take the time here to test and verify the properties of several imaging agents which may be used as part of our dual-isotope studies. Preparation and verification using normal animals is essential for trouble-free imaging of disease cases, in which a mistake could be costly in terms of both time and animal models.

II. Background

II.I Anesthesia Considerations

Because small animal SPECT requires long acquisition times, it is necessary to take precautions to avoid motion errors which may degrade the quality of physiologic measurements. In the case of small animals, motion is best reduced through the application of restraint or anesthesia; anesthesia is the humane choice because prolonged immobilization produces high amounts of stress in rodents, leading to complications ranging from increased heart rate to stomach ulcers[5]. Because the X-SPECT system is delivered without a means to deliver anesthesia, a custom system must be implemented to accommodate live animal studies.

Anesthetics used for imaging can generally be procured as either injectable liquids or inhalable gases. Injectable liquid anesthetics are more traditional, can be conveniently administered prior to image acquisition, and have the added benefit of being either local

or general in scope. They also have significant drawbacks such as addiction formation, less experimental flexibility, and formal documentation requirements[6]. For example, many injectable anesthetics are found on drug schedules, and hence are considered controlled substances. In addition, if an animal has a bad reaction to an injectable anesthetic after it is delivered, it is impossible to reduce the concentration of the anesthetic at that point and there is sometimes little an experimenter can do to prevent the bad reaction from escalating. This is due in part to the dose of an injectable anesthetic being calculated based on the weight of the animal; in cases such as heart failure, the animal's weight can fluctuate greatly over a short period of time due to the combined effects of edema and appetite, making the appropriate dose difficult to calculate.

Inhalant anesthetics, on the other hand, have a very quick washout due to their method of delivery, usually on the order of a few seconds. Thus, if an animal has a bad reaction to an inhalant anesthetic, the reaction can be quickly mitigated by a reduction in the rate of anesthetic delivery. The quick washout also allows more even dosing of the animal and the ability to regulate the precise amount of drug delivered during the course of the experiment, reducing the chance of an accidental euthanasia. This additional flexibility comes at a price, however; the anesthesia delivery system must be incorporated into the imaging system without affecting the quality of the data obtained.

II.II Temperature Control of the Imaging Chamber

Long SPECT acquisition times and prolonged anesthesia have a depressant effect on several physiologic systems, including that which regulates core body temperature[7, 8]. Although

a moderate decrease in core body temperature may be acceptable for some measurements, it has various effects on tracer uptake and metabolism[7] and therefore must be controlled if any meaningful comparisons are to be drawn between our data and that of other researchers. Temperature fluctuations are not permissible especially in the cardiovascular section of this work. Even a mild decrease in core body temperature will activate the sympathetic nervous system in an attempt to compensate, affecting our ability to quantify the sympathetic nerve density in the heart; a continued decrease in temperature will eventually induce motion artifacts into our image data by triggering shivering. Moreover, heart rate is dependent on temperature; fluctuations in temperature will produce corresponding fluctuations in heart rate, affecting our ability to average over several heart beats during the course of image production should we wish to perform a gated study. Because our X-SPECT system did not contain a method for heating anesthetized animal subjects, we have investigated several methods of maintaining the animal's core body temperature under anesthesia for the purposes of SPECT and CT image studies. In addition to the evaluation of traditional benchtop heating systems (infrared lamp, warm air circulation) commonly employed in such applications as surgery, we have developed a novel carbon-fiber heating system which is tailored to the specific needs of our small animal system.

II.III Tail Vein Injection/Catheterization

Many SPECT and CT imaging agents must be delivered directly into the circulatory system in order to function properly. In addition, some agents such as iothalamate (CT contrast agent) must be delivered at the precise time of imaging due to rapid washout; others such as ***meta***-iodobenzylguanidine (mIBG, SPECT agent for imaging sympathetic

nerve endings) must be delivered over a period of time due to toxicity. These factors are especially important in small animals, which have faster metabolisms and less physical reserves to mitigate the effects of any errors in agent delivery. The small size of the mouse also presents an experimental challenge to the experimenter's technique; a small error in positioning can make the difference between success and failure of an injection, or even precipitate a small radioactive spill. To address these potential complications, we have implemented a catheter and syringe pump delivery system which can deliver imaging agents to anesthetized rodents in a reproducible way.

II.IV Validation of Imaging Agents in Normal Animals

There are several clinically-available SPECT and CT agents for the evaluation of disease in humans. Due to their utility, noninvasiveness, and accurate portrayal of function, cardiovascular agents are responsible for approximately 40% of all nuclear medicine studies performed in hospitals[9]. The most common use of cardiovascular SPECT agents is in the evaluation and management of perfusion abnormalities in the heart. In addition, there are always new preclinical agents being evaluated in the research setting, providing us with several opportunities to evaluate and compare new drugs to older ones.

In addition, at the time of evaluation of these agents, the China Basin facility had just been opened, and no onehad any experience dealing with anesthesia, tail vein injection, or any other procedure associated with live animals. Moreover, no one knew how to get radioactivity or animals into the building either, and so I did a lot of administrative work to even make attempting the evaluation possible. However, it was desirable to work out

the details of in vivo imaging ahead of time to avoid technical complications relating performing complex procedures for the first time. Although ideally we would have liked to concentrate on just two SPECT imaging agents, our search for an acceptable mouse model led us to evaluate many more. As part of the proposals generated as end-point possibilities for this thesis, we have tested the imaging properties of following six agents in preparation for biological studies in small animals:

1) ^{99m}Tc-sestamibi, used clinically for evaluation of cardiac perfusion

2) ^{125}I-***meta***-iodobenzylguanidine (mIBG), a preclinical imaging agent which localizes to sympathetic nerve terminals

3) ^{99m}Tc-methylene diphosphonate (MDP), a clinical agent which is used to detect new bone formation, usually in the context of cancer metastasis

4) Iothalamate, a conventional CT contrast agent

5) Fenestra VC, a novel long-lived vascular contrast agent for use in small animals

6) Fenestra LC, a novel long-lived liver contrast agent targeted at tumor detection

^{99m}Tc-sestamibi is one of the most common clinical SPECT agents. Sestamibi is a member of the isonitrile family of chemical compounds; its chemical name is hexakis 2-methoxyisobutyl isonitrile. Due to its nonpolarized chemical structure, ^{99m}Tc-sestamibi is cell-membrane permeant; due to its overall positive charge, it tends to accumulate in areas of low membrane potential (most often inside the cell or its mitochondria). Therefore, ^{99m}Tc-

sestamibi injected intravenously tends to accumulate in tissues which are metabolically active and receive adequate blood flow. This quality makes it a valuable agent for evaluating cardiac perfusion: areas of the myocardium which are ischemic (have inadequate blood flow) or contain large amounts of scar tissue exhibit relatively less uptake of the radiotracer than their healthy counterparts[9].

^{125}I-***meta***-iodobenzylguanidine (mIBG) is a preclinical imaging agent which localizes to sympathetic nerve terminals. Receptors on these terminals bind to and package ^{125}I-mIBG into vesicles at the nerve terminal due to its chemical similarity to epinephrine, or adrenaline. Once ^{125}I-mIBG is taken up by sympathetic nerves, its similarity to epinephrine ends; ^{125}I-mIBG is not able to be metabolized properly by normal cells. Instead, it retained in the nerves until an outside force stimulates the nerves to release adrenaline; ^{125}I-mIBG washout is dependent on sympathetic nerve activity[10].

^{99m}Tc-methylene diphosphonate (MDP) is a clinical agent which is used to detect new bone formation, usually in the context of cancer metastasis. Indeed, for the detection of metastatic tumors to the bone, ^{99m}Tc-MDP imaging is the method of choice. Mechanistically speaking, ^{99m}Tc-MDP is a hydroxyapatite analog and is incorporated during the formation of new bone, allowing us to image areas of bone turnover and formation. In addition to its valuable use as a skeletal imaging agent, ^{99m}Tc-MDP can also be used to label red blood cells. In this context, thombi, emboli, hemorrhages, and hemangiomas may be identified[9].

Iothalamate is a conventional CT contrast agent. Although it is used clinically, the high osmolarity of the contrast solution given to patients pulls water from the surrounding tissues

and red blood cells into the blood vessels, causing heat and pain during dose administration. In addition, the hyperosmolar nature of the contrast solution is also associated with quick washout by the renal system and often concomitant acute renal failure. To compensate for this the base sugar molecule of iothalamate has a ring structure containing two side chains; an iodine atom is covalently bonded to each side chain. The side chains increase the polarity of the molecule, enhance its solubility in water, and hence reduce the toxicity of this agent. There are additional complications in murine studies due to the viscosity of the agent and the high doses delivered, namely difficulties related to flow through the narrow-bore needles required for tail vein injection and difficulties related to cardiac arrhythmia due to toxicity[11].

Fenestra VC and LC contrast agents have recently appeared on the market for use in small animals. Instead of being based upon an iodinated sugar, these agents mimic the structure and biological properties of a chylomicron. This has the advantage of long vascular retention and lowered toxicity, an ideal combination for small animal CT imaging, which may require as much as 30 minutes for data acquisition[12].

III. Methods

III.I Anesthesia

The issue of anesthesia implementation was addressed first. Although the X-SPECT system could physically accommodate the placement of a rodent inside the imaging chamber, no means for keeping the animal still during the imaging session was provided with the

system itself. Therefore we consulted with the local IACUC (institutional animal care and use committee) for suggestions and ultimately decided to implement a gaseous isoflurane anesthesia system obtained from Summit Medical.

The basic system consists of an oxygen source, an oxygen flowmeter, an isoflurane vaporizer, a patient breathing circuit, and a waste-gas scavenging device[13]. Potential system options for the overall system were evaluated on the basis of system versatility and projected use, which we expected to expand, and on cost. The patient breathing circuit was also of special interest to us. As explained by the manufacturer, the patient circuit has four functions: deliver oxygen to the patient, deliver anesthetic to the patient, remove carbon dioxide produced by the patient, and provide a means for ventilation (if needed)[13]. In addition, we required that the patient circuit accommodate the needs of our imaging system, namely the need to be functional when the machine was closed and fully shielded, and the need to avoid interfering with the rotating motion of the gantry of the imaging system.

III.II Tail Vein Injections: Catheter Implantation and Syringe Pump Use

Imaging agent delivery was tackled next. During the course of iothalamate and ^{125}I-mIBG administration (see results below), it was noted that rapid delivery of the imaging agent was associated with cardiac arrhythmias and sudden death. In addition, it was noted that iothalamate exhibited a very rapid washout, one which was generally too fast to allow sufficient time for data acquisition. Finally, as a novice to tail vein injection and with no one in the lab available to teach the technique, I received a very high radiation dose to the hands (but still technically within acceptable limits) during initial experiments using

^{99m}Tc-sestamibi as exhibited by the reading on my finger ring. This resulted in a discussion with the local radiation safety official, Keith Cudaback, and a rethinking of imaging agent delivery.

To address these problems, a syringe pump and catheter delivery system was implemented. Catheters with small diameters capable of being inserted into murine tail veins were obtained from Strategic Applications (Libertyville, IL). These catheters contain 10cm of 28G (0.014" x 0.007") Dow Pellethane Polyurethane connected to 7" of (0.033" x 0.014") and 23G thin wall needle[14]. The also contain a small guide wire which may be used to support the catheter during implantation. A suitable syringe pump model BSP was obtained from Braintree Scientific (Braintree, MA). This pump contains an interchangeable mechanical motor which drives the plunger of a syringe at a known rate. Should another rate be desired, either the type of syringe used for delivery may be varied or the motor may be replaced by one which operates at a different speed. The pump was fitted with a custom motor which delivers agents at the rate of 34 microliters per minute and was also bought from Braintree. This rate was chosen so that a typical injection volume of 200-400 microliters could be delivered over the course of approximately ten minutes.

This system was evaluated on the basis of its ability to consistently and slowly deliver imaging agents to the mouse, and on its ability to provide a hands-free dose delivery which would reduce radiation dose to the experimenter during the course of injection, even if the experimenter required several minutes to locate the tail vein and successfully implant a catheter or syringe needle.

III.III Control of Core Body Temperature

To address the issue of animal heating during image acquisition, several methods were tested inside the X-SPECT imaging environment. Core body temperatures of animals were measured to within 0.1°C using a TCAT-2 temperature controller (Braintree Scientific) and heat application was controlled by active feedback from an animal rectal probe (not shown). A rectal probe provides feedback to the heating system, and the heating system is powered by a 120V AC outlet.

Warm air, infrared (IR), and carbon fiber heating systems were implemented in this manner to maintain an animal's temperature. The conventional warm air and IR systems work by regulating the flow of hot air or IR light to the animal in response to the feedback system. A carbon-fiber heating pad was obtained from Thermion Systems International (Stratford, CT). These pads can also be powered by and AC outlet, produce heat resistively in response to electrical current flowing through them, and are normally employed in various applications from de-icing airplane wings to heating car seats.

We also evaluated a gel pack heating system. Gel pack heating systems sold for surgical applications supply energy in the form of heat to an animal by virtue of a chemical reaction. We purchased a Deltaphase Isothermal Heating Pad gel pack from Braintree Scientific. The animal was placed directly on top of the gel pack and the surface area common to both was maximized to maximize heat transfer to the animal. In addition, to aid the efficiency of the procedure, the gel pack can often be placed on top of an insulating surface to help direct the available heat to the animal and not to the lab bench. After use, the gel pack

was recharged with the use of hot water or a microwave.

We evaluated the heating systems for their ability to maintain rodent core body temperature in the imaging system over extended lengths of time (up to 3 hours) without interfering with the movement of the imaging collimator. The animal's chest was banded with hook and loop fasteners to minimize respiratory movement during data acquisition as part of a lung tumor detection study.

III.IV Validation of Imaging Agents in Normal Animals

The following imaging agents were evaluated in the X-SPECT imaging system to verify their imaging properties and to troubleshoot any unexpected complications before proceeding with imaging investigations of pathology. Injection was done in mice under anesthesia to prevent distress due to immobilization. During injection, the anesthetized mice were kept warm using either an IR lamp or a carbon-fiber heating system receiving feedback from a rectal probe. Data was reconstructed using either the algorithm supplied by the manufacturer or, after the dual-isotope methodology was developed, processed with this methodology and reconstructed using an iterative ML-EM algorithm obtained from A. Hwang.

III.V ^{99m}Tc-sestamibi

Clinical imaging protocols were followed to image ^{99m}Tc-sestamibi in mice. Between 1 and 5 mCi (200-500 microliters) were injected over the course of 5-10 minutes. The mouse was then returned to the anesthesia induction box, given food and water, and allowed to

recover from anesthesia. After a delay of 30-45 minutes, the mouse was then anesthetized and placed on the scanner for imaging. 64-128 SPECT projections were acquired over 360° using a 1.0 mm pinhole.

III.VI ^{125}I-mIBG

Between 0.25 and 1 mCi ^{125}I-mIBG (300-700 microliters) were injected over the course of 10-20 minutes. Due to toxicity concerns, injection was halted at the first sign of cardiac arrhythmia. The mouse was then returned to the anesthesia induction box, given food and water, and allowed to recover from anesthesia. After a delay of 15-20 minutes, the mouse was then anesthetized and placed on the scanner for imaging. 64 SPECT projections were acquired over 360° using a 1.0 mm pinhole.

III.VII ^{99m}Tc-MDP

Between 3 and 25 mCi ^{99m}Tc-MDP (300-700 microliters) were injected over the course of 10-20 minutes. Due to toxicity concerns, injection was halted at the first sign of cardiac arrhythmia. The mouse was then either maintained under anesthesia or returned to the anesthesia induction box, given food and water, and allowed to recover from anesthesia. After a delay of 1-4 hours, the mouse was then anesthetized and placed on the scanner for imaging. 64 SPECT projections were acquired over 360° using a 1.0 mm pinhole.

III.VIII Iothalamate

Between 200 and 900 microliters of iothalamate (300 mg I / mL) were injected over the course of 10-20 minutes. Due to toxicity concerns, injection was halted at the first sign of cardiac arrhythmia. The mouse was then placed on the scanner for imaging. 256 or 512 CT projections were acquired over 360º using an x-ray operating voltage of 50 kVp and 600 microamps current.

III.IX Fenestra VC and LC

Following the manufacturer's recommendation, 400 microliters of Fenestra VC or LC were injected over the course of 2-5 minutes. The mouse was then returned to its cage, given food and water, and allowed to recover for 1-4 hours. The mouse was then reanesthetized and placed on the scanner for imaging. 256 or 512 CT projections were acquired over 360º using an x-ray operating voltage of 50 kVp and 600 microamps current.

IV. Results

IV.I Anesthesia

A diagram of the full system obtained from Summit Medical[13] is shown below.

For our oxygen source, we chose to use H-tanks, which contain 6900 liters of oxygen, due to our anticipation of increasing use requirements. We purchased both the oxygen flowmeter and the anesthesia vaporizer from Summit Medical, and also a wheeled stand

which allowed us to move the anesthesia system from the X-SPECT system to the Mohawk system in the event that our Mohawk system became ready for animal experiments.

To avoid respiratory acidosis caused by rebreathing waste carbon dioxide, we chose a Bain style patient breathing circuit. This circuit is pictured below in an image taken from Summit Medical's Principles of the Anesthetic Machine[13].

Figure 36: Components of the Anesthesia Machine

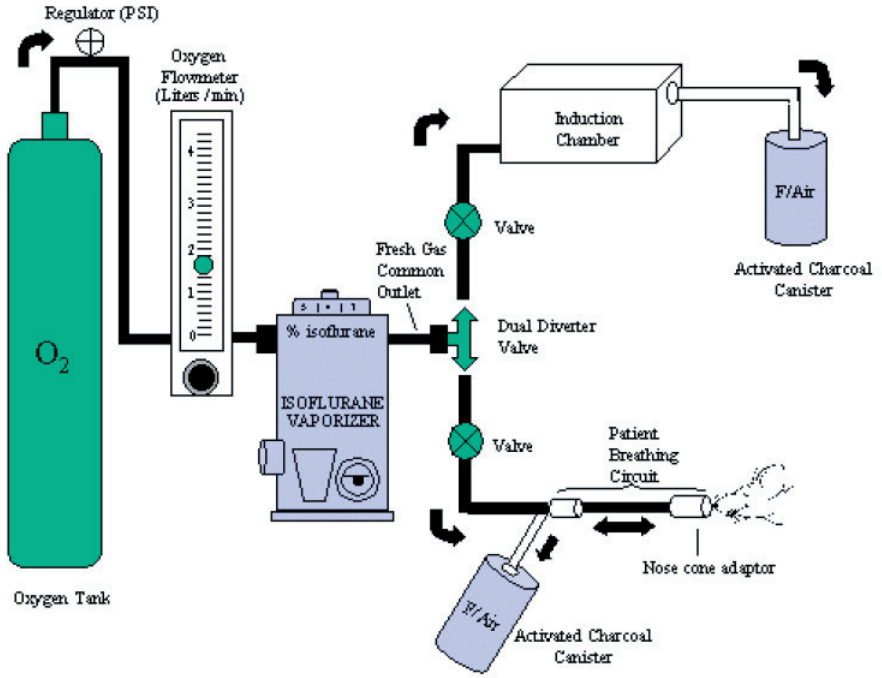

As shown above, fresh oxygen and anesthetic are delivered to the patient via the small tube connected to the rodent nose cone in the center of the Bain apparatus. Different sized nose cones are provided to ensure that the area surrounding the patient's nose and mouth is not too large, which would allow rebreathing. Waste gases, such as carbon dioxide and unused anesthetic, exit the mouse via the larger scavenging tube. Because the system relies on passive gas flow, this scavenging tube is significantly larger than the fresh gas delivery

tube to ensure that waste gases are removed efficiently. The manufacturer of the X-SPECT does provide two lengths of tubing for anesthesia purposes, but these tubes have an average diameter of less than 0.25 inches, and they are the same size. In light of rebreathing and passive flow system (pressure) concerns, this tubing was bypassed and the Bain system was implemented in its place.

Figure 37: Patient Breathing Circuit (Bain Style)

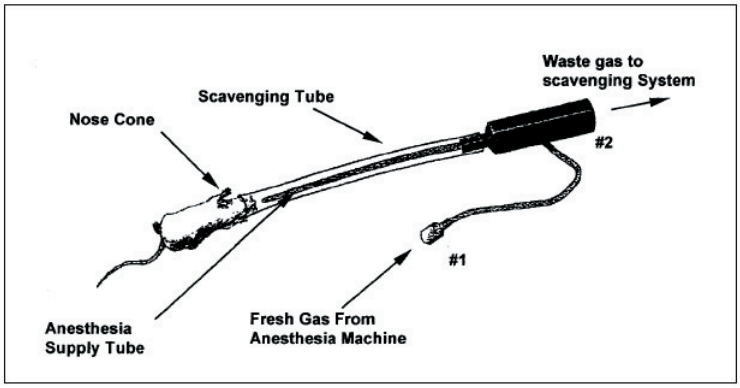

We purchased a flowmeter and vaporizer from Summit Medical. Because we are imaging rodents, we deemed that we would require between 0.5 and 2 liters per minute[13]. The flowmeter and vaporizer chosen are capable of reliably delivering 1-5% isoflurane at 0.3-5 liters per minute oxygen flow, which should be enough to meet the needs not only of the X-SPECT, but also the Mohawk imaging system, should both systems be operational at the same time. Waste gases are scavenged using the lab's snorkel system instead of charcoal.

In light of cost considerations, the options to include a manifold (to regulate flow to more than one mouse separately), a heater (to help prevent mice from becoming hypothermic), and a humidifier (to prevent nasal and other membranes from desiccating) were not implemented at this time. However, the system was chosen to be flexible enough to

accommodate these additions should they be deemed necessary at a later date.

IV.II Tail Vein Injections: Catheter Implantation and Syringe Pump Use

A syringe pump and catheter delivery system was implemented to assist with agent delivery. An image of this catheter obtained from the manufacturer's website[14] is shown here.

To use these catheters, they must first be flushed with saline. Although they encompass very little volume, we have unintentionally verified experimentally that there is enough air inside the catheter to cause an embolism during agent delivery in a mouse. In addition, the addition of heparin at 2 units per milliliter in the saline will prevent the formation of blood clots during and after implantation. To implant the catheter, it is removed from the included needle, and a small hole is made in the surface of the tail, just enough to allow access to the vein. A large hole will allow bleeding, which makes it difficult to see. With the guide wire inside the catheter for support and the flap of skin covering the hole held aside, the catheter may be inserted into the tail vein. Care must be taken to ensure that the catheter is truly in the vein, and not merely into the subcutaneous region surrounding it. Correct implantation may be verified by the withdrawal of the guide wire; a successful attempt can be verified by the presence of blood propelled by blood pressure of the animal into the catheter bore.

Figure 38: Rodent Catheter

After catheter implantation, the dose was delivered at a rate of 34 microliters per minute to

the mouse using the BSP syringe pump. An image of the syringe pump obtained from the manufacturer's website[15] is shown here.

This method of catheter implantation allows the researcher to locate the tail vein and prepare it for agent delivery without accumulating radiation dose due to handling a syringe full of activity. In addition, the implementation of a syringe pump allows slow, even delivery of the agent without the dose complication. Taken together, these components provide a method for radiotracer delivery to the vascular system of the mouse in which the only doses necessary to the experimenter are that related to removing bubbles from the dose syringe (to avoid embolism) and that related to transfer of the syringe from the lead pig to the syringe pump itself. This represents a minimization of dose to the experimenter.

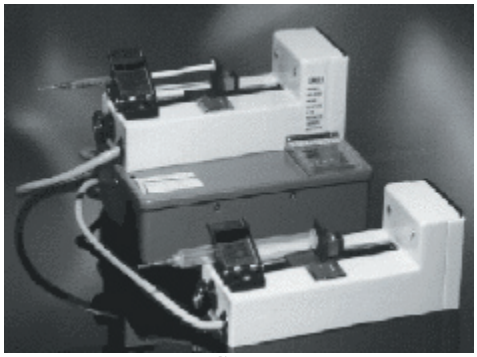

Figure 39: Syringe Pump

IV.III Control of Core Body Temperature

We adapted several conventional (infrared heat lamp, warm air circulation, microwaveable gel pack) heating systems for use in the X-SPECT microSPECT/CT imaging system. The gel pack system cooled quickly (<30 minutes) and to accommodate geometrical limitations

Figure 40: Heating Systems

imposed by the pack's thickness, the collimator's radius of rotation had to be increased during imaging. Hot air and infrared heat lamp systems performed well with respect to temperature regulation (<1.0°C variance from 37°C), were compatible with collimator positioning, and produced minimal attenuation; however, these systems also produced a small amount of noise in the detector electronics which can be seen in the figure. The images are taken over time as heat from an infrared lamp is applied to maintain the mouse's body temperature; for comparison, the background corresponding to areas marked by colored rectangles in

Figure 41: Temperature Induced Detector Noise

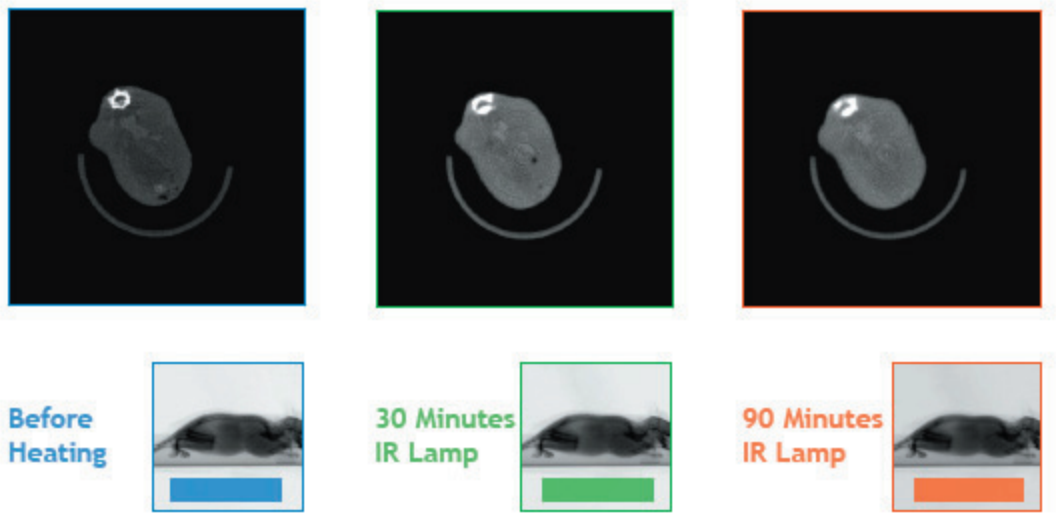

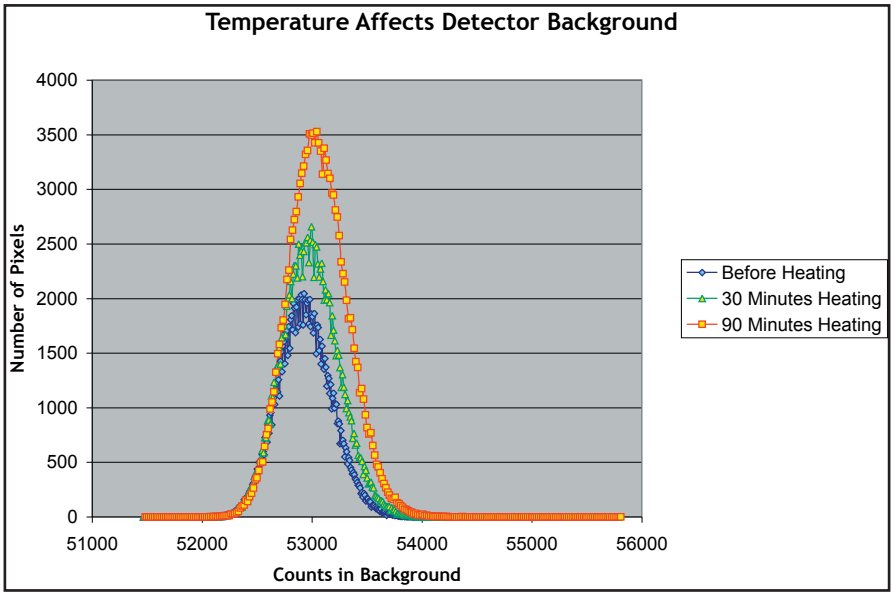

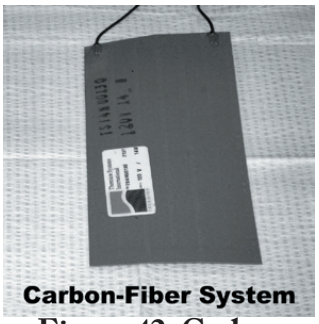

Figure 42: Carbon Fiber System

the projection data above is plotted below. Microwaveable gel packs did not exhibit this effect.

Carbon fiber pads, shown at left, were successfully utilized to maintain core body temperatures of rodents to within 1.0°C during imaging. The image of an anesthetized rat in the X-SPECT system (below left) illustrates the carbon-fiber heating pad geometry. CT images of mice demonstrate minimal effects of the heating system on image quality. Shown in the center is an axial CT section through a mouse's thorax with the heater removed. At the right is an axial section through a mouse's thorax with the heater located underneath the patient bed. The flexible composition of the pad and its sub-millimeter thickness allow it to conform to the cylindrical geometry of the mouse bed while avoiding geometrical conflicts with the imaging collimator.

Figure 43: Carbon Fiber System Geometry During Imaging

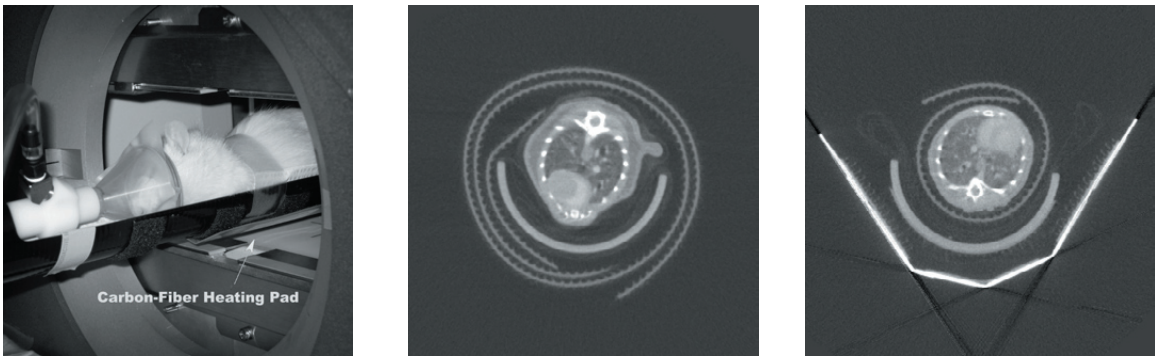

IV.IV Validation of Imaging Agents in Normal Animals

IV.V ^{99m}Tc-sestamibi

^{99m}Tc-sestamibi yielded good views of the left ventricular myocardium for all levels of injected dose, as expected. No adverse effects were noted either on agent administration or during imaging. Shown here are results from an exploratory study performed in collaboration with Alana Welm. The SPECT data (color) is coregistered and overlayed upon data obtained from a CT study (grayscale) performed shortly after the SPECT acquisition was completed, and the combined data are presented here to give the reader a sense of anatomy which is often lacking in SPECT data presented separately.

Figure 44: ^{99m}Tc Sestamibi Normal Uptake

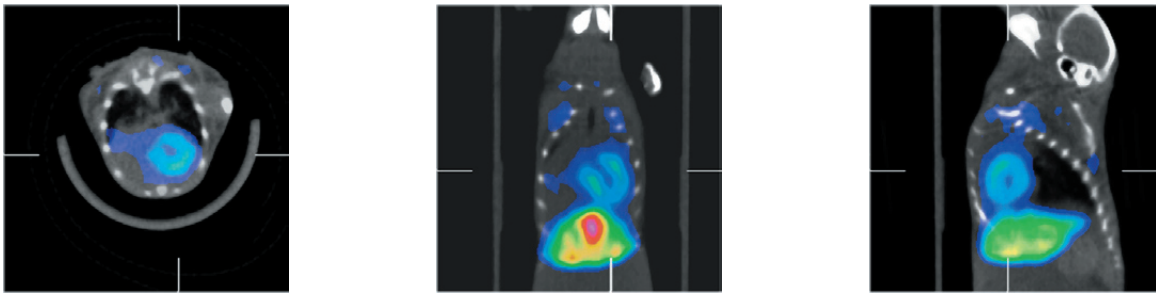

This mouse not only exhibited excellent uptake in the myocardium, but also exhibited a tumor in the left upper lobe of the lung which took up the agent quite well. This image spawned a tumor detection study using ^{99m}Tc-sestamibi which will be discussed further in the next chapter. Also visible in these sections are the liver and gallbladder, which represent the normal excretion pathway for this drug. Should it be desired, the administration of cholecystokinin (CCK) could be employed to empty the gallbladder and decrease the uptake in these regions.

IV.VI ^{125}I-mIBG

Figure 45: ^{125}I Sestamibi Normal Uptake

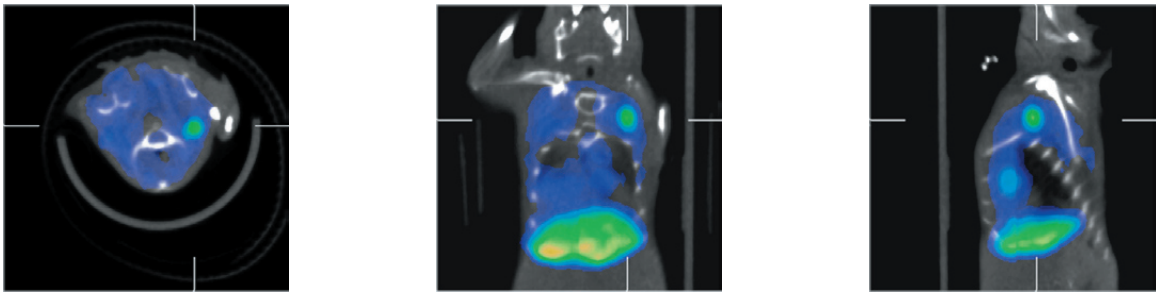

In contrast to ^{99m}Tc-sestamibi, ^{125}I-mIBG proved to be a difficult imaging agent to utilize. Upon administration, ^{125}I-mIBG produced an increase in heart rate in all subjects, a feature likely due to its chemical similarity to adrenaline. In practice, appearance of this feature was quickly followed by cardiac arrest and death. In addition, administration of this agent appeared to be irritating to soft tissues, as evidenced by the tail twitching and movement. Occasionally this movement was so great that the catheter or syringe needle was dislodged, leading to the need for reimplantation and spill containment (blood leaking from the tail now contained a source which would be radioactive for the next two years). In addition, because injection was halted at the first sign of cardiac irritability, it was quite difficult to inject enough activity into the mouse in order to yield definable images. Moreover, even when definable images of the myocardium were obtained, most of the activity localized to the liver and intestines due to the high density of sympathetic nerve terminals located there. The discrepancy is so large that the heart is often not visible in ^{125}I-mIBG SPECT projections, and its location must therefore be inferred from the position of the liver in the imaging field of view before the onset of data acquisition. As shown below, injection of 0.9 mCi of ^{125}I-mIBG produces recognizable images of the heart, but injection of only 0.25

mCi ^{125}I-mIBG results in a cardiac image very much obscured by noise. In this instance, the heart cannot even readily be differentiated from the pulmonary tissue surrounding it.

Figure 46: 0.9 mCi ^{125}I-mIBG Injected Dose, Overlayed SPECT/CT Data

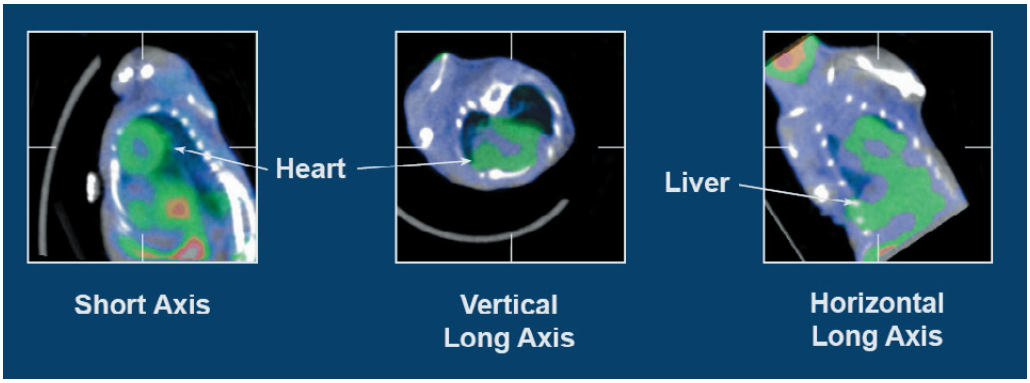

Figure 47: 0.25 mCi ^{125}I-mIBG Injected Dose, SPECT Data Only

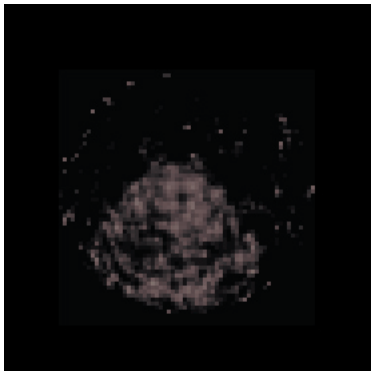

IV.VII ^{99m}Tc-MDP

^{99m}Tc-MDP yielded good SPECT images of the skeleton, as expected. No adverse effects were noted either on agent administration or during imaging, although a concern had been raised due to toxicity related to cardiac irritability due to calcium scavenging properties of this agent. Shown here are results from an exploratory study performed in collaboration with Alana Welm. The SPECT data is a tomogram through the skull of the mouse. This region was chosen for imaging because it was hoped that the new mouse model of breast cancer being developed would metastasize to this location, similar to the process in humans.

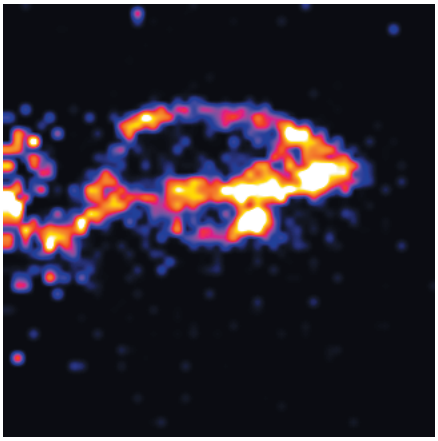

Figure 48:
99mTc-MDP Normal Uptake

Although this mouse exhibited excellent uptake in the skeletal system, preliminary attempts yielded less desirable results. It was noticed that longer delays between injection and imaging (4 hours) produced much better skeletal uptake than shorter delays (2 hours). In addition, excretion of this drug is through the urinary system, and longer washout times increased the probability that the mouse would void, lowering the background activity in the bladder. Poor skeletal uptake was also noted for mice that remained under anesthesia during drug washout. Finally, the first subject studied received a dose which had begun to dissociate (labeling is stable only for a matter of hours) and showed notable uptake in the stomach and GI tract.

IV.VIII Iothalamate

Iothalamate also proved to be a difficult imaging agent to use in practice. Its administration was complicated by the induction of arrhythmias which were often fatal. In addition, the rapid washout (a few seconds) proved to be quicker than our image acquisition hardware could handle (20 minutes per acquisition). Therefore the catheter and syringe pump delivery system mentioned above was implemented. This allowed a steady dose of contrast agent to be delivered to the mouse throughout the course of the experiment. The resulting images are shown below.

Figure 49: Contrast-Enhanced CT Using Iothalamate

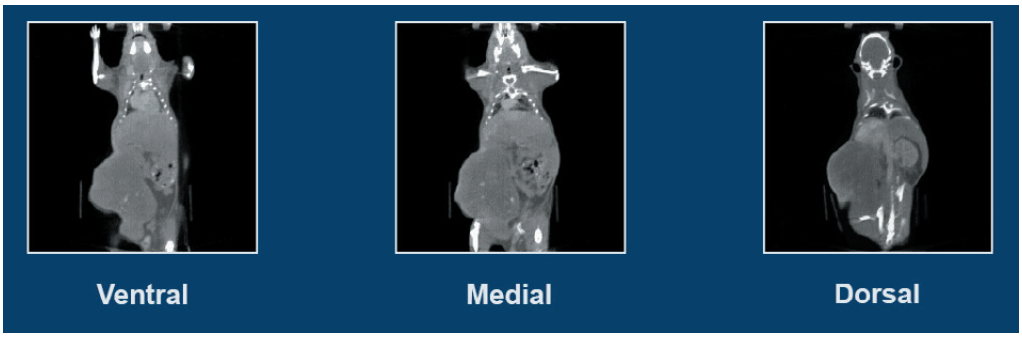

One kidney and the inferior vena cava can be seen quite clearly in these images. However, the arterial system is less distinct due to washout of the drug from the vascular system. Finally, the ventral part of the large mammary tumor evident exhibits more enhancement than the dorsal section, suggesting that this part of the tumor is better pefused. This led to the idea of using contrast media to estimate perfusion levels in a tumor, an idea which is explored in a later chapter.

IV.IX Fenestra VC and LC

Fenestra VC and LC were in practice the easiest to use of all the agents studied. Dosing was simple due to the manufacturer's specification especially for mice. In addition, no adverse effects were noted upon administration, even with relatively rapid injections (<1 min). Furthermore, every experiment performed with these agents exhibited excellent soft tissue contrast at all levels within the mouse. As shown below, this agent produced reliable and dramatic soft tissue contrast in the heart, abdomen, and limbs. The only drawback noted was the apparent inability of transgenic mice from a collaboration with Darya Soto (genotype proprietary at the time) to metabolize the agent. These mice died or were euthanized 48 hours post-imaging due to complications associated with minimal GI mobility. The manufacturer was contacted regarding this issue, and the agent was returned, but the manufacturer was unable to provide an adequate explanation. We acknowledge the possibility that this may be a function of the genetic modification of the mice themselves.

Figure 50: Contrast-Enhanced CT Using Fenestra

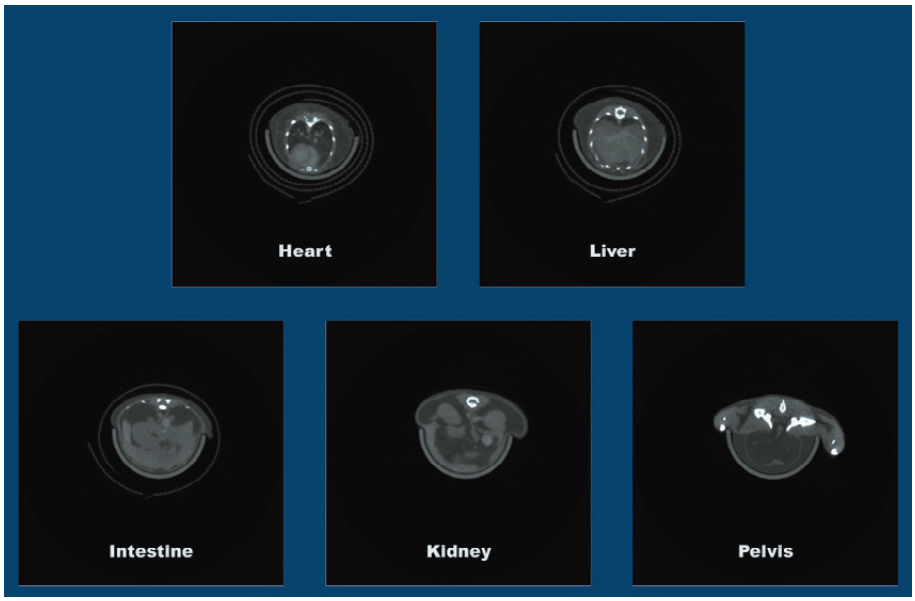

V. Discussion

We have successfully implemented several physiologic monitoring systems within the X-SPECT imaging system. First, we implemented a gaseous isoflurane anesthesia system, which allowed us to immobilize murine subjects of study humanely for up to eight hours. In addition, the system plumbing could easily be modified to accommodate two imaging systems simultaneously, should both scanners in our laboratory be operated simultaneously. Second, we implemented a catheter and syringe pump delivery system to aid in the administration of noxious imaging agents. The added advantage of slow and steady agent delivery translates to reduced risk of sudden death during agent administration. This delivery system also reduces radiation dose to the experimenter by virtue of removing the need to hold the syringe during tail vein access and agent delivery. Third, we tested several heating systems for maintenance of patient core body temperature during imaging. Gel pack systems were found to cool too quickly for long imaging sessions and their bulk interfered with the imaging collimator. Warm air and IR systems heated the animal adequately, due to a feedback system which received data from a rectal probe. However, these systems also heated the detector electronics, producing noise in the final images acquired. Finally, a novel carbon-fiber heating system was developed which was connected to the feedback system. This configuration produced stable temperature regulation (<1°C variance from 37°C) and its slim profile did not interfere with the motion of the imaging collimator.

We also successfully imaged several SPECT tracers and CT contrast agents in normal mice. Successful images of the murine heart were obtained with ^{99m}Tc-sestamibi and ^{125}I-mIBG, although images from ^{125}I-mIBG exhibited high background in the liver and

GI tract. We also investigated the ability of ^{99m}Tc-MDP to image the murine skeleton. The best bone images were obtained with ^{99m}Tc-MDP using long washout times, short labeling to injection times, and high injection activities. Finally we explored various CT contrast agents for use in mice. Iothalamate, a conventional CT contrast agent, was found to produce soft tissue contrast, but was difficult to implement in our system due to its rapid washout. Fenestra VC and LC, in contrast, were quite simple to use and provided excellent contrast over a range of 1-4 hours post-administration.

With these studies completed, we are now equipped to move on to studying biological correlations in more interesting mouse models of human disease.

VI. References

1. Funk, T., et al., ***A multipinhole small animal SPECT system with submillimeter spatial resolution***. Med Phys, 2006. 33(5): p. 1259-68.

2. Zaidi, H., ***Recent developments and future trends in nuclear medicine instrumentation***. Z Med Phys, 2006. 16(1): p. 5-17.

3. Metzler, S.D., et al., ***Molecular imaging of small animals with a triple-head SPECT system using pinhole collimation***. IEEE Trans Med Imaging, 2005. 24(7): p. 853-62.

4. Beekman, F.J., et al., ***U-SPECT-I: a novel system for submillimeter-resolution tomography with radiolabeled molecules in mice***. J Nucl Med, 2005. 46(7): p. 1194-200.

5. Pare, W.P. and G.B. Glavin, ***Restraint stress in biomedical research: a review***. Neurosci Biobehav Rev, 1986. 10(3): p. 339-70.

6. Stimpfel, T.M. and E.L. Gershey, ***Selecting anesthetic agents for human safety and animal recovery surgery***. FASEB J, 1991. 5(7): p. 2099-104.

7. Buggy, D.J. and A.W. Crossley, ***Thermoregulation, mild perioperative hypothermia and postanaesthetic shivering***. Br J Anaesth, 2000. 84(5): p. 615-28.

8. Kaiyala, K.J. and D.S. Ramsay, ***Assessment of heat production, heat loss, and core temperature during nitrous oxide exposure: a new paradigm for studying drug effects and opponent responses***. Am J Physiol Regul Integr Comp Physiol, 2005. 288(3): p.

R692-701.

9. Zeissman, H.A., O'Malley, J.P., Thrall, J.H., ***Nuclear Medicine: The Requisites, Third Edition***. 3 ed. (Requisites in Radiology). 2005: Mosby.

10. Flotats, A. and I. Carrio, ***Cardiac neurotransmission SPECT imaging.*** J Nucl Cardiol, 2004. 11(5): p. 587-602.

11. Almen, T., ***Contrast media: the relation of chemical structure, animal toxicity and adverse clinical effects.*** Am J Cardiol, 1990. 66(14): p. 2F-8F.

12. Badea, C.T., et al., ***4-D micro-CT of the mouse heart.*** Mol Imaging, 2005. 4(2): p. 110-6.

13. ***Principles of the Anesthetic Machine***, S. Medical, Editor.

14. ***Part Number MTV-01.*** [cited; Available from: http://www.sai-infusion.com/content/view/308/360/.

15. ***Braintree Scientific syringe pump.*** [cited; Available from: http://www.braintreesci.com/SyringePumps.htm#single.

Chapter 5

Dual-Isotope Cardiac Studies In Mice

I. Introduction

As discussed in Chapter 1, chronic diseases such as cancer are among the leading causes of death in industrialized nations such as the United States[1]. In this country, approximately one out of every five people who die this year will die of heart disease. Furthermore, it is becoming increasingly evident that these conditions depend upon a number of risk factors, many of which interact, and most which are poorly understood. For example, one such factor which is common to many chronic conditions is blood flow, or perfusion, and there is a large body of study devoted to the improvement of our understanding of the molecular mechanisms involved in the evaluation of tissue perfusion and the factors which influence its evolution.

In response to the importance placed on noninvasive small animal studies at the biological and medical research fronts, and given the advantages of imaging studies listed above, the focus of this work is on the advancement of imaging technologies which will augment and extend the current capabilities of combined SPECT/CT imaging systems. In particular, we will demonstrate the utility of dual-isotope techniques used to measure perfusion and those biological factors to which it is correlated. Using our microSPECT/CT imaging systems as a means of obtaining medically relevant physiologic and pathologic data, these investigations will highlight the advantage of simultaneous data acquisition from two sources for *in vivo* data collection and analysis.

II. Background

II.I Cardiovascular Disease

Cardiovascular disease is among the leading causes of death in industrialized nations such as the United States. Among the variations of cardiovascular disease, the most prevalent is ischemic heart disease (IHD)[2]. IHD is the leading cause of death in industrialized nations such as the United States; roughly two out of every five people who die this year will die as a result of IHD. Moreover, IHD disrupts the quality of life for many more Americans by interfering with any activity that places demands on the heart. With the growing number of people surviving into their 70s, and beyond, there is a corresponding growth in the need to study the pathogenesis and prevention of such conditions as IHD.

IHD designates a spectrum of diseases which all have one feature in common: impaired blood flow, or ischemia, to the myocardium. Since the myocardium is metabolically a very active tissue, prolonged or severe ischemia can rapidly lead to myocardial death, or infarction, due to both lack of oxygen and lack of nutrients. In more than 90% of cases[2], IHD is precipitated by the growth of atherosclerotic plaques in one or more of the coronary arteries which supply the heart muscle with blood; for this reason, IHD is often referred to as coronary heart disease.

Coronary heart disease is thought to begin in childhood or late adolescence with the formation of small atheromatous plaques in the elastic arteries of the body. These plaques are clinically silent for many decades, due to slow growth and minimal arterial obstruction. Later in the course of the disease, the first symptom of IHD is often angina, or chest pain,

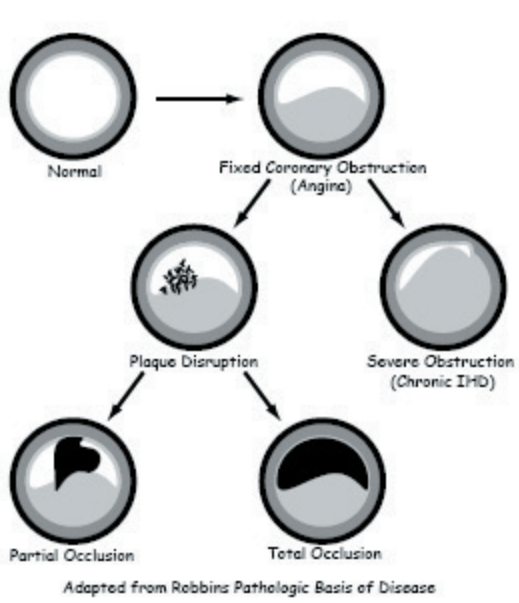

Figure 51: Atherosclerotic Plaque

during activities which require increased cardiac output. In these cases, angina is the result of the heart's increased demand for blood flow upon a compromised coronary artery system. In addition, angina is often the harbinger of chronic IHD or acute myocardial infarction (MI). Although chronic IHD is associated with chronic severe arterial obstruction, acute MI is most often associated with moderately-sized plaques that do not necessarily produce angina. This is because moderately-sized plaques are both dynamic and unstable, and because they often contain a soft necrotic core capable of initiating platelet aggregation. Moreover, the rupture of such a plaque can easily precipitate a catastrophic cardiac event: exposure of the plaque's soft core starts the chain reactions of platelet aggregation and thrombus, or blood clot, formation. In extreme cases, the thrombus may occlude a significant fraction of a main coronary artery, causing sudden death. Fortunately, with the advent of better therapeutics and screening option, we are finding that many of the risk factors for IHD are not only treatable but preventable. Even so, our understanding is incomplete; IHD causes an estimated 750,000 death in the United States each year[2].

II.II Cardiomyopathy

A cardiomyopathy is any disease which is intrinsic to the myocardium itself; it is not produced by such outside effects as atherosclerosis or toxins. Dilated cardiomyopathies are those which affect the myocardium in such as way as to produce a dilatation of the heart cavities. Usually the heart is enlarged and flabby in these cases and, as opposed to the case of hypertrophic cardiomyopathy, the ventricle walls are either of normal or reduced thickness relative to those of healthy individuals. Dilated cardiomyopathy occurs at any age, but it most commonly affect adults between the ages of 20 and 60 years. In the clinic, this condition presents as slowly progressive congestive heart failure, with end-stage disease resulting in ejection fractions below 25% (normal ejection fraction is 55% or better). Following diagnosis, 50% of dilated cardiomyopathy patients die within 2 years; 75% within 5 years. Death in these cases is usually attributable to progressive cardiac failure or arrhythmia, although embolism from mural thrombi (formed due to decreased wall motion of the failing heart) may also be responsible[2].

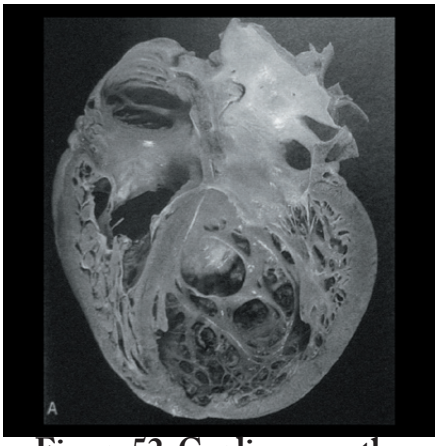

Figure 52: Cardiomyopathy Gross Pathology

Figure 53: Cardiomyopathy Histology

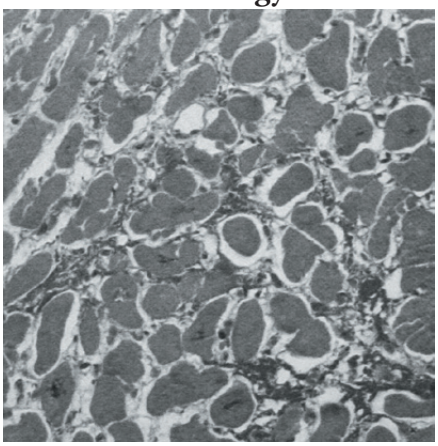

Although the gross pathology described above is well documented, it is associated with nonspecific histological abnormalities (myocyte hypertrophy, enlarged nuclei, and interstitial and endocardial

fibrosis), and these histological findings do not correlate well with either patient prognosis or physiological disfunction[2]. Therefore, there is much that we have yet to discover about the roots of this disease.

II.III ECG Acquisition, Placement of Leads, and Cardiac Gating

Because we are interested in the influence of the sympathetic nervous system of the generation of arrhythmias, it is useful to review the conduction of electrical impulses in the heart. The task of coordinating of the heart's pumping action is accomplished by a network of electrical fibers. Because a cardiomyocytes initiate contraction upon reaching a certain electrical potential across the cell membrane, coordinated electrical signals sent from a central location can induce the entire organ to contract nearly simultaneously.

As shown[3], the signal to pump is generated in a special region of the right atrium known as the sinoatrial (SA) node. From this location, an electrical impulse is relayed to the rest of the right atrium, to the left atrium, and to the atrioventricular (AV) node. A timing delay is built into the AV node so that it does not propagate the electrical signal it receives until the atria have finished contracting, filling the ventricles. After this delay, the AV node electrically excites the bundle of His and the bundle branches, which run through the ventricular septum and then out to Purkinje fibers in the ventricles. These fibers carry

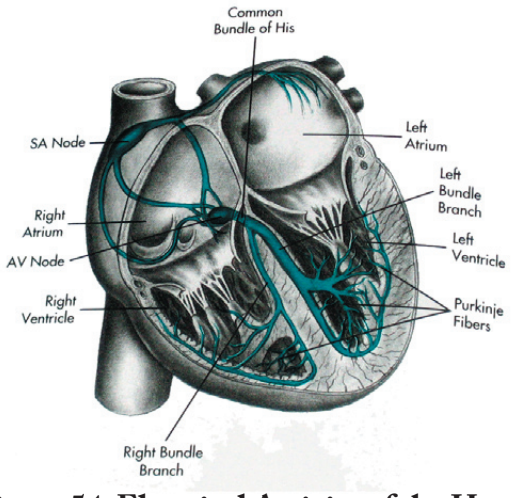

Figure 54: Electrical Activity of the Heart

the electrical impulse generated originally by the SA node to the rest of the ventricular conduction system, which stimulates the myocardium to contract as a whole to pump blood to the lungs and the rest of the body's tissues.

We can monitor the electrical activity of the heart using a set of sensitive electrical leads (electrocardiogram monitoring, or ECG). The simplest set of ECG leads is known as Einthoven's triangle, which is shown in the figure[3] below. Einthoven's triangle specifies the location of three augmented limb leads, which are designated aVR (placed at the right arm), aVL (placed at the left arm), and aVF (placed at the left leg). Calculating the voltage differences between the augmented limb leads yields the standard limb leads: the voltage difference between aVR and aVL is designated lead I, the voltage difference between aVR and aVF as lead II, and the voltage difference between aVL and aVF as lead III. Because lead II runs along the direction of the left ventricular axis, it receives a very good view of the left ventricular activity; it is also the most familiar trace on an ECG printout, which is shown below for a normal patient.

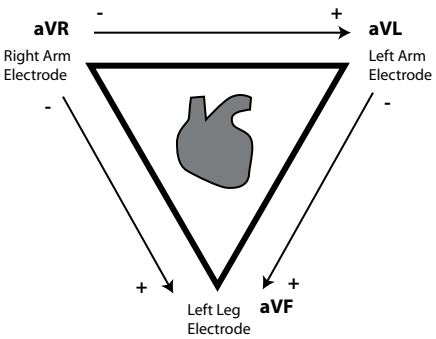

Figure 55: ECG Lead Placement

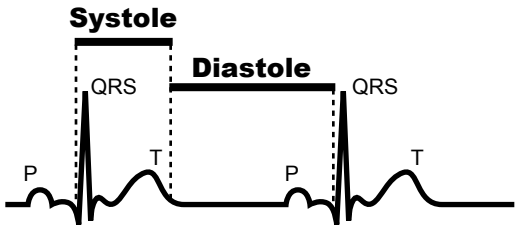

Figure 56: ECG Normal Appearance

Inspection of the ECG trace reveals several features of interest. At the beginning of the trace, a P wave can be seen. This P wave corresponds to electrical activity which stimulates atrial contraction. Next and most prominent, the QRS complex is visualized, which corresponds

to the electrical depolarization of the ventricles, triggering the start of contraction. Following the QRS complex is the T wave, which corresponds to the repolarization of the ventricles (atrial repolarization is not seen because it is hidden by the large ventricular signal). Although these electrical signals conduct quite rapidly, contraction of the heart muscle itself is relatively slow. As shown, ventricular systole (contraction) is sustained from the beginning of the QRS complex until near the end of the T wave. Ventricular diastole (relaxation) extends from the end of the T wave, through the P wave, and does not end until the beginning of the next QRS complex.

Maintenance of a regular pumping rhythm requires the musculoelectrical system of the heart to be healthy, with a ready blood supply (continual generation of the cardiomyocyte's electrical potential is an energy-intensive process). Electrical abnormalities commonly associated with cardiovascular disease—infarction, hypertrophy, or irritability—can alter the formation of the electrical potential within the cardiomyocytes or damage the conduction pathways in a larger region of the heart, which may lead to an arrhythmic heart beat, fibrillation, or even sudden cardiac death.

II.IV G-Protein Interactions and Their Relationship to Cardiovascular Disease

II.V The Conklin Mouse

The Conklin mouse model is a model of dilated cardiomyopathy which progresses to heart failure and eventually death through steps similar to those of many cardiovascular patients[4]. This mouse has been genetically engineered to express a cell-surface receptor

(Ro1) which activates the $G\alpha_i$-protein pathway in the heart using the myosin heavy chain promoter under control of tetracycline administration. As shown, this pathway counteracts the effects of the more commonly known $G\alpha_s$ pathway. The $G\alpha_s$ pathway is normally stimulated by increased activity of the β-adrenergic receptors in the myocardium. $G\alpha_s$ activation in turn activates the second messenger cAMP, which interacts with protein kinase A (PKA) to influence calcium metabolism within cardiac myocytes, increasing the heart's contractility and rate of contraction. This effect is often seen in heart failure,

Figure 57: G-protein Pathways in the Heart

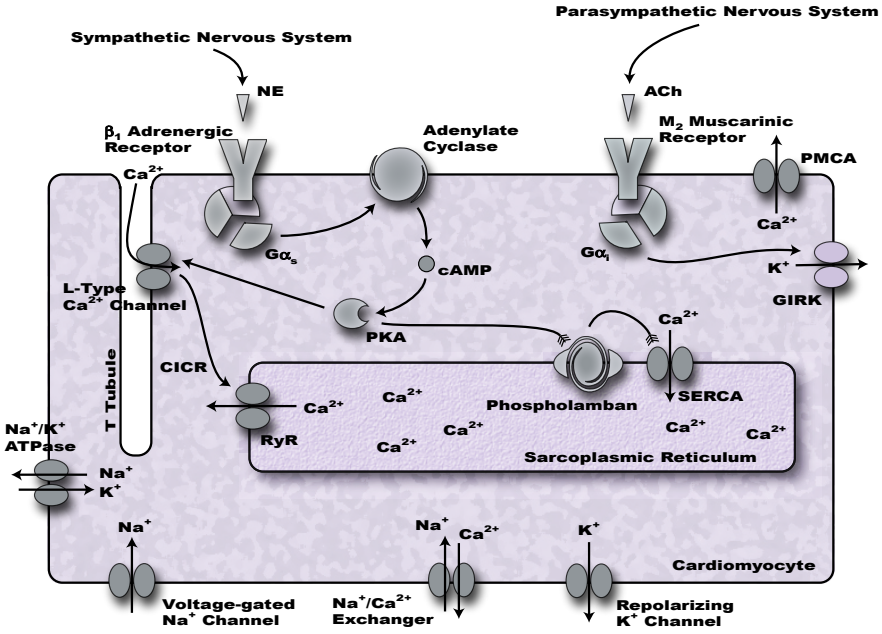

where it is considered a compensatory measure. The manipulations in the Ro1 mouse produce an animal which is phenotypically normal as long as its diet is supplemented with antibiotics such as tetracycline or doxycyline. Withdrawal of the antibiotics results in expression of the Ro1 receptor, activation of the $G\alpha_i$ pathway, and development of a severe dilated cardiomyopathy. If allowed to progress, this disease will result in heart failure accompanied by anasarca, arrhythmia, and eventually death, a common end point to many

forms of cardiovascular compromise. Therefore, this mouse provides a unique opportunity to study the initial events which lead to both dilated cardiomyopathy, heart failure, and the activation of the $G\alpha_s$ pathway via the sympathetic nervous system.

II.VI Overview of Radiopharmaceuticals: mIBG and Sestamibi

As discussed in Chapter 1, the ability to acquire data from two—or more—biological processes in just one imaging session is one of the great advantages of an imaging modality such as SPECT over other modalities such as computed tomography (CT) or positron emission tomography (PET), in which only a single measurement can be made at a time. The use of two SPECT tracers, ^{99m}Tc-sestamibi and ^{125}I-iodorotenone will be useful in the study of the Conklin Ro1 mouse.

As discussed in Chapter 4, ^{99m}Tc-sestamibi is one of the most common clinical SPECT agents. Sestamibi is a member of the isonitrile family of chemical compounds; its chemical name is hexakis 2-methoxyisobutyl isonitrile. Due to its nonpolarized chemical structure, ^{99m}Tc-sestamibi is cell-membrane permeant; due to its overall positive charge, it tends to accumulate in areas of low membrane potential (most often inside the cell or its mitochondria). Therefore, ^{99m}Tc-sestamibi injected intravenously tends to accumulate in tissues which are metabolically active and receive adequate blood flow. This quality makes it a valuable agent for evaluating cardiac perfusion: areas of the myocardium which are ischemic (have inadequate blood flow) or contain large amounts of scar tissue exhibit relatively less uptake of the radiotracer than their healthy counterparts[5].

As discussed in Chapter 4, ^{125}I-*meta*-iodobenzylguanidine (mIBG) is a preclinical imaging agent which localizes to sympathetic nerve terminals. Receptors on these terminals bind to and package ^{125}I-mIBG into vesicles at the nerve terminal due to its chemical similarity to epinephrine, or adrenaline. Once ^{125}I-mIBG is taken up by sympathetic nerves, its similarity to epinephrine ends; ^{125}I-mIBG is not able to be metabolized properly by normal cells. Instead, it retained in the nerves until an outside force stimulates the nerves to release adrenaline; ^{125}I-mIBG washout is dependent on sympathetic nerve activity[6].

III. Methods

As discussed in Chapter 4, injection was done in mice under anesthesia to prevent distress due to immobilization. During injection, the anesthetized mice were kept warm using either an IR lamp or a carbon-fiber heating system receiving feedback from a rectal probe. 64 SPECT projections were acquired over 360º using a 1.0 mm pinhole. Data was processed using the dual-isotope methodology presented earlier and reconstructed using an iterative ML-EM algorithm obtained from A. Hwang. ECG leads were placed at both arms and any arrhythmias which appeared were noted.

III.I Measurement of Cardiac Perfusion in Normal Animals

Following procedures developed in Chapter 4, clinical imaging protocols were followed to image ^{99m}Tc-sestamibi in mice. Between 1 and 5 mCi (200-500 microliters) were injected over the course of 5-10 minutes. The mouse was then returned to the anesthesia induction box, given food and water, and allowed to recover from anesthesia. After a delay of 30-45

minutes, the mouse was then anesthetized and placed on the scanner for imaging.

III.II Measurement of Cardiac Sympathetic Innervation in Normal Animals

Following procedures developed in Chapter 4, between 0.25 and 1 mCi ^{125}I-mIBG (300-700 microliters) were injected over the course of 10-20 minutes. Due to toxicity concerns, injection was halted at the first sign of cardiac arrhythmia. The mouse was then returned to the anesthesia induction box, given food and water, and allowed to recover from anesthesia. After a delay of 15-20 minutes, the mouse was then anesthetized and placed on the scanner for imaging.

III.III Simultaneous Measurement of Innervation and Perfusion in Normal Animals

In addition to the single isotope studies, one mouse also underwent a dual-isotope imaging study. 0.25 mCi ^{125}I-mIBG (300-700 microliters) was first injected over the course of 10-20 minutes. Due to toxicity concerns, injection was halted when signs of cardiac arrhythmia developed. The mouse was then returned to the anesthesia induction box, given food and water, and allowed to recover from anesthesia. After a delay of 15-20 minutes, the mouse was then anesthetized and placed on the scanner for imaging.

After imaging, 1 mCi ^{99m}Tc-sestamibi was then injected. The mouse was then again returned to the anesthesia induction box, given food and water, and allowed to recover from anesthesia. After a delay of 30-45 minutes, the mouse was then anesthetized and placed on the scanner for imaging. Data from each isotope were processed and separated as described in chapter 3. The image obtained using the ^{125}I window in the dual-isotope

case was compared to that in the single-isotope case.

IV. Results

IV.I Measurement of Cardiac Perfusion in Normal Animals

^{99m}Tc-sestamibi proved to be a very nice imaging agent, yielding good views of the left ventricular myocardium for all levels of injected dose, as expected. No adverse effects were noted either on agent administration or during imaging. The SPECT data (color) is coregistered and overlayed upon data obtained from a CT study (grayscale) performed shortly after the SPECT acquisition was completed, and the combined data are presented here to give the reader a sense of anatomy which is often lacking in SPECT data presented separately.

Figure 58: ^{99m}Tc-Sestamibi Uptake in a Normal Mouse

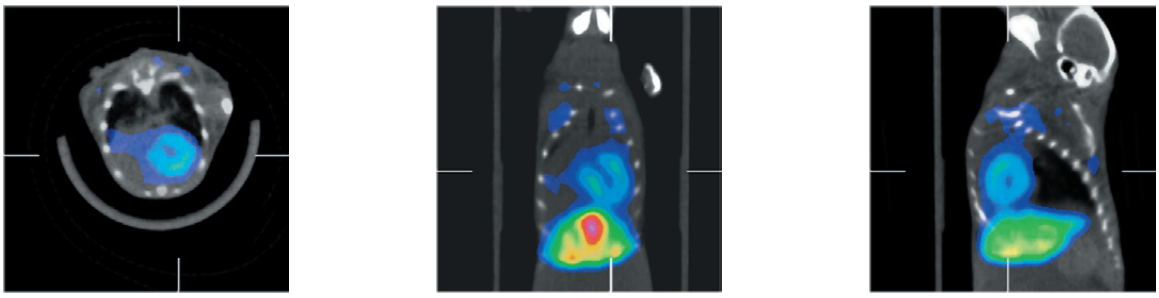

IV.II Measurement of Cardiac Sympathetic Innervation in Normal Animals

In contrast to ^{99m}Tc-sestamibi, ^{125}I-mIBG proved to be a difficult imaging agent to utilize. Upon administration, ^{125}I-mIBG produced an increase in heart rate in all subjects, a feature likely due to its chemical similarity to adrenaline. In practice, appearance of this feature was quickly followed by cardiac arrest and death. In addition, because injection was

halted at the first sign of cardiac irritability, it was quite difficult to inject enough activity into the mouse in order to yield definable images. As shown below, injection of 0.9 mCi of ^{125}I-mIBG produces recognizable images of the heart, but injection of only 0.25 mCi ^{125}I-mIBG results in a cardiac image very much obscured by noise. In this instance, the heart cannot even readily be differentiated from the pulmonary tissue surrounding it.

Figure 59: 0.9 mCi ^{125}I-mIBG Injected Dose, Overlayed SPECT/CT Data

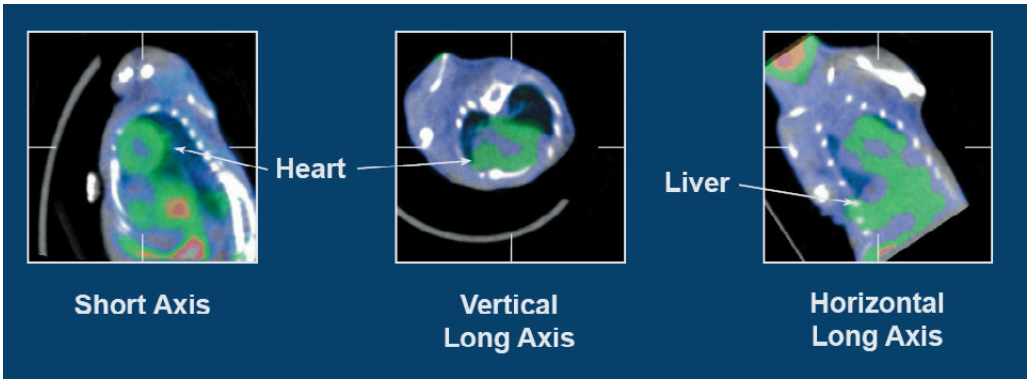

Figure 60: 0.25 mCi ^{125}I-mIBG Injected Dose, SPECT Data Only

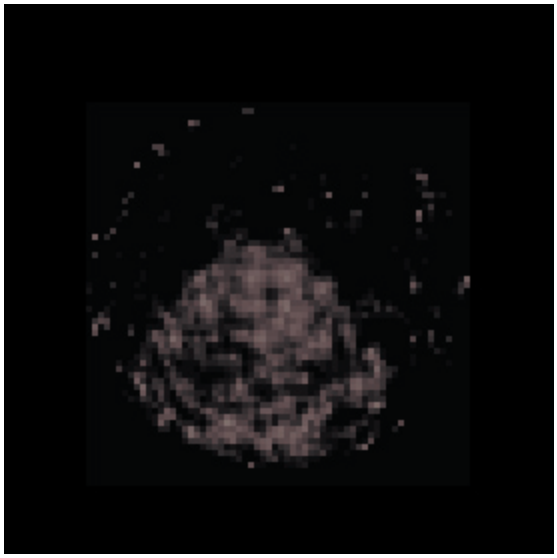

IV.III Simultaneous Measurement of Innervation and Perfusion in Normal Animals

In addition to the single isotope studies, one mouse also underwent a dual-isotope imaging study. Due to toxicity concerns, injection was halted when cardiac arrhythmia developed, resulting in a low injected dose of ^{125}I-mIBG. Shown here is an axial tomogram through the left ventricle from the single-isotope ^{125}I-mIBG SPECT image which demonstrates high noise due to low counting statistics.

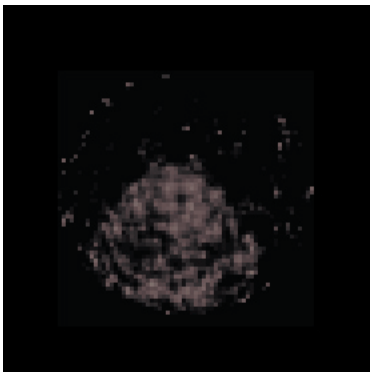

Figure 61: mIBG Only

Next, ^{99m}Tc-sestamibi was injected and a dual-isotope image was obtained using the methods described earlier. Shown below is an axial tomogram through a slice at the same level as the tomogram shown above. (It is not exactly the same slice because the mouse was removed from the imaging apparatus in order to allow the mouse to recover during ^{99m}Tc-sestamibi washout.) On the left is the expected ^{99m}Tc-sestamibi image, which demonstrates good delineation of the myocardium. At center, the ^{125}I-mIBG image obtained simultaneously still suffers from low count statistics. On the right is a rendering of the coregistered CT data.

Figure 62: Dual Isotope Imaging in Normal Mice

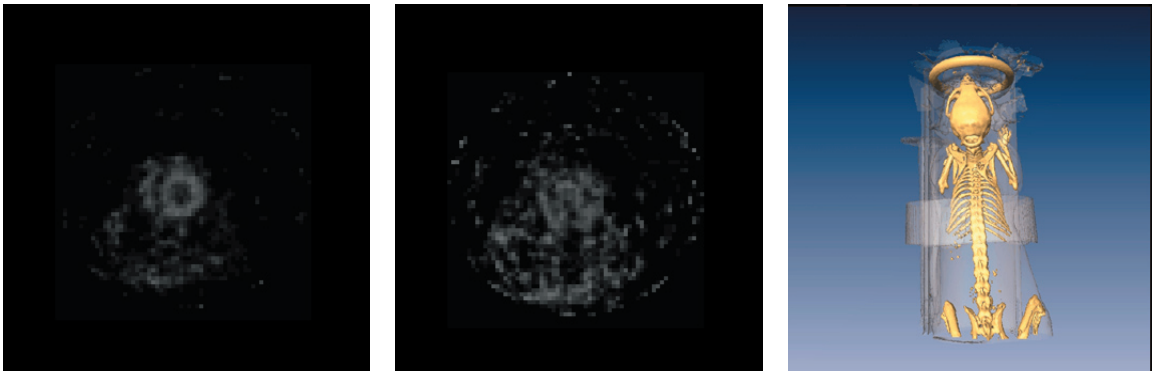

V. Discussion

With a little more effort, this study could be completed. All of the ground work has been done to make this study possible: the dual-isotope methodology has been created, and both of the agents in question have been imaged in the same mouse simultaneously. The only difficulties at this point are technical and these details can be smoothed out. On a more positive note, we have successfully demonstrated simultaneous in vivo imaging in mice using ^{99m}Tc and ^{125}I isotopes. In addition, we have demonstrated the utility of our software in separating the signals from each isotope and reconstructing each separately.

VI. References

1. Minino AM, Heron MP, Smith BL. *Deaths: preliminary data for 2004. Natl Vital Stat Rep.* 2006 Jun 28;54(19):1-49

2. Cotran RS, Kumar V, Collins T, Robbins SL. *Robbins Pathologic Basis of Disease.* W.B. Saunders Company; 6th edition (January 15, 1999)

3. Grauer K. *Practical Guide to ECG Interpretation.* Mosby; 2 edition (June 1, 1998)

4. Redfern CH, Degtyarev MY, Kwa AT, Salomonis N, Cotte N, Nanevicz T, Fidelman N, Desai K, Vranizan K, Lee EK, Coward P, Shah N, Warrington JA, Fishman GI, Bernstein D, Baker AJ, Conklin BR. *Conditional expression of a Gi-coupled receptor causes ventricular conduction delay and a lethal cardiomyopathy.* Proc Natl Acad Sci U S A. 2000 Apr 25;97(9):4826-31

5. Ziessman HA, O'Malley JP, Thrall JH. *Nuclear Medicine: The Requisites, Third Edition (Requisites in Radiology).* Mosby; 3 edition (December 21, 2005)

6. Flotats A, Carrio I. *Cardiac neurotransmission SPECT imaging.* J Nucl Cardiol. 2004 Sep-Oct;11(5):587-602

7. Jan S, Santin G, Strul D, Staelens S, Assie K, Autret D, Avner S, Barbier R, Bardies M, Bloomfield PM, Brasse D, Breton V, Bruyndonckx P, Buvat I, Chatziioannou AF, Choi Y, Chung YH, Comtat C, Donnarieix D, Ferrer L, Glick SJ, Groiselle CJ, Guez D, Honore PF, Kerhoas-Cavata S, Kirov AS, Kohli V, Koole M, Krieguer M, van der Laan DJ, Lamare F, Largeron G, Lartizien C, Lazaro D, Maas MC, Maigne L, Mayet F, Melot F, Merheb C, Pennacchio E, Perez J, Pietrzyk U, Rannou FR, Rey M, Schaart DR, Schmidtlein CR, Simon L, Song TY, Vieira JM, Visvikis D, Van de Walle R, Wieers E, Morel C. *GATE: a simulation toolkit*

for PET and SPECT. Phys Med Biol. 2004 Oct 7;49(19):4543-61

8. Tacke MB, Szymanowski H, Oelfke U, Schulze C, Nuss S, Wehrwein E, Leidenberger S. *Assessment of a new multileaf collimator concept using GEANT4 Monte Carlo simulations.* Med Phys. 2006 Apr;33(4):1125-32

9. Enger SA, Rezaei A, af Rosenschold PM, Lundqvist H. *Gadolinium neutron capture brachytherapy (GdNCB), a new treatment method for intravascular brachytherapy.* Med Phys. 2006 Jan;33(1):46-51

10. Jiang H, Wang B, Xu XG, Suit HD, Paganetti H. *Simulation of organ-specific patient effective dose due to secondary neutrons in proton radiation treatment.* Phys Med Biol. 2005 Sep 21;50(18):4337-53

11. Ballester F, Granero D, Perez-Calatayud J, Casal E, Puchades V. *Monte Carlo dosimetric study of best industries and Alpha Omega Ir-192 brachytherapy seeds.* Med Phys. 2004 Dec;31(12):3298-305

12. Segars WP, Tsui BM, Frey EC, Johnson GA, Berr SS. *Development of a 4-D digital mouse phantom for molecular imaging research.* Mol Imaging Biol. 2004 May-Jun;6(3):149-59

13. http://dmip.rad.jhmi.edu/people/faculty/Paul/Segars_research.htm#MOBY

Chapter 6

Dual-Isotope Cancer Studies In Mice

I. Introduction

As discussed in Chapter 1, chronic diseases such as cancer are among the leading causes of death in industrialized nations such as the United States[1]. In this country, approximately one out of every five people who die this year will die of cancer. Furthermore, it is becoming increasingly evident that disease conditions depend upon a number of risk factors, many of which interact, and most which are poorly understood. For example, one such factor which is common to many chronic conditions is blood flow, or perfusion, and there is a large body of study devoted to the improvement of our understanding of the molecular mechanisms involved in the evaluation of tissue perfusion and the factors which influence its evolution.

In response to the importance placed on noninvasive small animal studies at the biological and medical research fronts, and given the advantages of imaging studies listed above, the focus of this work is on the advancement of imaging technologies which will augment and extend the current capabilities of combined SPECT/CT imaging systems. In particular, we will demonstrate the utility of dual-isotope techniques used to measure perfusion and those biological factors to which it is correlated. Using our microSPECT/CT imaging systems as a means of obtaining medically relevant physiologic and pathologic data, these investigations will highlight the advantage of simultaneous data acquisition from two sources for *in vivo* data collection and analysis.

II. Background

II.I SPECT Imaging in the Management of Breast Carcinoma

One of the most common clinical applications of SPECT is the bone scan. The agents of choice for bone imaging are labeled with ^{99m}Tc and are characterized by P - C - P structure, in which P represents either pyrophosphate or diphosphonate and C represents carbon. ^{99m}Tc bone agents are taken up in the mineral phase of bone, most avidly in regions of amorphous calcium phosphate and less avidly in mature crystalline hydroxyapatite, where their accumulation is thought to represent areas of increased osteoblastic activity.

Because metastatic disease often affects the axial skeleton, SPECT imaging techniques employing bone agents can be a useful tool for cancer management. Metastatic invasion can be depicted as either hot or cold lesions on a bone scan, depending on the type of cancer involved. Metastases which produce bone lysis followed by reactive bone formation appear as localized hot spots corresponding to the margin of invasion on a bone scintigram; however, lesions produced by extremely aggressive metastases may appear cold (photon deficient) due to complete destruction of the bone matrix and its constituent cell types (most notably osteoblasts). Although many bone scans incorporate only planar images, cross sectional SPECT tomograms can often help to define the extent of involvement due to greater lesion contrast obtained (for both hot and cold lesions). In addition, the use of a pinhole collimator can produce magnified images, which are useful both in children and in evaluation of the hip for osteonecrosis.

In a similar method to clinical cardiovascular studies, the ability of ^{99m}Tc-sestamibi to

localize within areas of high metabolic activity has also been utilized with variable success to visualize tumor locations within the body. This agent is readily taken up by many active tumors, but suffers from it tendency to be removed from the cell by the expression of the multidrug resistance gene. Expression of this gene is also associated with the ability of tumors to resist chemotherapeutic drugs and ^{99m}Tc-sestamibi imaging is also being investigated as a prognostic tool in this respect.

II.II Macrophage-Stimulating Factor and Its Relationship to Breast Tumor Metastasis

One molecular factor which has received much recent attention is macrophage stimulating factor (MSP). This molecule is related to epithelial cell survival and is postulated to have a role in development of carcinomas such as those of breast cancer. Our colleague, Alana Welm, is investigating the role of MSP in the metastasis of mammary carcinoma of the breast. She has developed an orthotopic model in which primary cells are removed from the mammary glands of a normal mouse; infected with a retrovirus carrying the genes for some combination of the polyoma middle T antigen (PyMT), dsRed, GFP, and macrophage stimulating protein (MSP); and returned to the cleared inguinal fat pad of the mouse. There, these cells form large primary tumors, and depending on the genes transferred to them, also metastasize to the lung and skeleton. Because the Welm model exhibits metastasis in addition to production of primary tumors, this is a unique opportunity to test the efficacy of these agents in a physiologic setting which is highly relevant to that of the human disease case.

III. Methods

Following procedures developed in Chapter 4, all injections in mice were done under anesthesia to prevent distress due to immobilization. During injection, the anesthetized mice were kept warm using either an IR lamp or a carbon-fiber heating system receiving feedback from a rectal probe. For each study 64 SPECT projections were acquired over 360° using a 1.0 mm pinhole collimator. Data was processed using the dual-isotope methodology presented in earlier chapters, and reconstructed using an iterative ML-EM algorithm obtained from A. Hwang.

III.I ^{99m}Tc-Sestamibi Imaging of Primary Breast Tumors and Metastasis to Lung

Clinical imaging protocols were followed to image ^{99m}Tc-sestamibi in mice. Between 1 and 5 mCi (200-500 microliters) were injected over the course of 5-10 minutes. The mouse was then returned to the anesthesia induction box, given food and water, and allowed to recover from anesthesia. After a delay of 30-45 minutes, the mouse was then anesthetized and placed on the scanner for imaging. 64-128 SPECT projections were acquired over 360° using a 1.0 mm pinhole. 4 normal and 5 tumor-bearing mice were used for this study.

III.II ^{99m}Tc-MDP Imaging

Following procedures developed in Chapter 4, between 3 and 25 mCi ^{99m}Tc-MDP (300-700 microliters) were injected over the course of 10-20 minutes. Due to toxicity concerns, injection was halted at the first sign of cardiac arrhythmia. The mouse was then either maintained under anesthesia or returned to the anesthesia induction box, given food and

water, and allowed to recover from anesthesia. After a delay of 1-4 hours, the mouse was then anesthetized and placed on the scanner for imaging. 8 normal mice and 6 tumor-bearing mice were used for this part of the study.

III.III Imaging Metastasis To Bone Using ^{99m}Tc-MDP

Following procedures developed in Chapter 4, mice were anesthetized and injected with 20 mCi ^{99m}Tc-MDP over the course of 10-20 minutes. The mouse was then returned to the anesthesia induction box, given food and water, and allowed to recover from anesthesia. After a delay of 4 hours, the mouse was then anesthetized for imaging. Given an estimate based on placing a euthanized mouse in the dose calibrator after an imaging experiment, we expected 20% uptake of ^{99m}Tc-MDP in the skeletal system of the mice. This estimate indicates that the ratio of ^{99m}Tc to ^{125}I in the animal is roughly 1:1, giving us an expected 5% crosstalk error in the ^{125}I image if the data set is uncorrected. 6 tumor-bearing mice were used for this study.

IV. Results

IV.I ^{99m}Tc-Sestamibi Imaging of Breast Tumors

Uptake of ^{99m}Tc-sestamibi in breast tumors was mixed. On our first attempt, a single metastasis in the upper left lobe of the lung was easily detected. The entire volume of the metastasis appeared to take up the drug uniformly and contrast with the surrounding lung tissue was excellent. Necropsy confirmed the presence of this tumor and that no other tumors were present in this animal. (The primary tumor had been previously removed

surgically after being allowed to grow for several weeks.)

Figure 63: ^{99m}Tc-Sestamibi Detection of Breast Cancer Metastasis

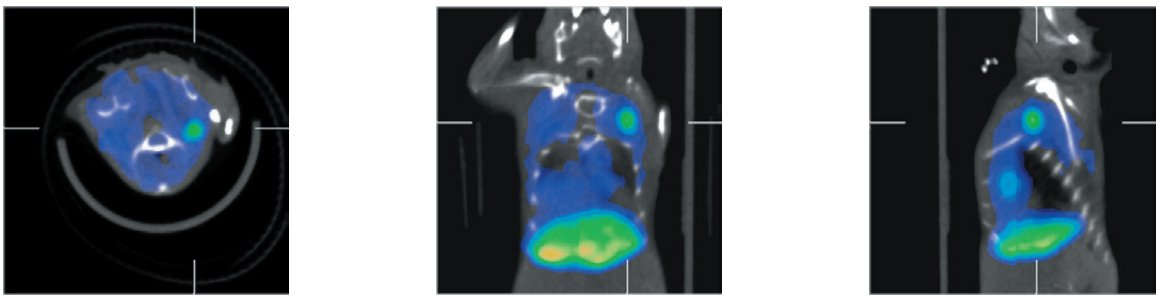

Every animal studied after the first exhibited poor uptake of ^{99m}Tc-sestamibi, both in the primary tumor and in metastatic lesions. In one animal, 3 small metastases were located on necropsy close to and below the heart, near the diaphragm. These tumors were not discerned on imaging, and we surmise that this is a function of low uptake and normal respiratory motion. In addition, as shown below, primary tumors exhibited staining consistent with a rim of viable tissue surrounding a large necrotic core. This is especially visible in the large primary tumor on the left side of the coronal section images (top). Correlated CT data

Figure 64: Rendering of CT Data Depicting Primary Breast Tumors

has been rendered using the Amira software package and is shown to illustrate the size and extent of tumors present in this mouse. Normal heart, liver, and gallbladder uptake are visible as well, although their appearance is distorted due to a colormap chosen to highlight low levels of tumor staining.

Figure 65: SPECT Data Depicting Primary Breast Tumors

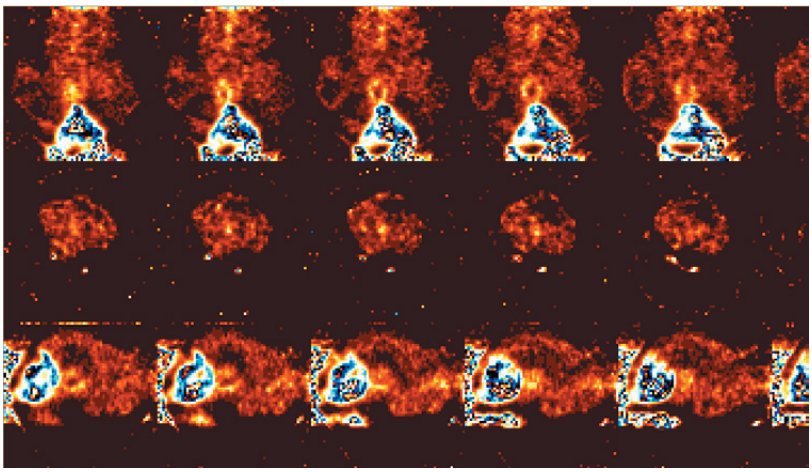

IV.II Imaging Using ^{99m}Tc-MDP

As discussed in Chapter 4, ^{99m}Tc-MDP yielded good SPECT images of the skeleton in normal mice, as expected. Shown here is a SPECT tomogram through the skull of the mouse. This region and the distal femur were chosen for imaging because it was hoped that the new mouse model of breast cancer being developed would metastasize to these locations, mimicking the process in

Figure 66: ^{99m}Tc-MDP Bone Uptake

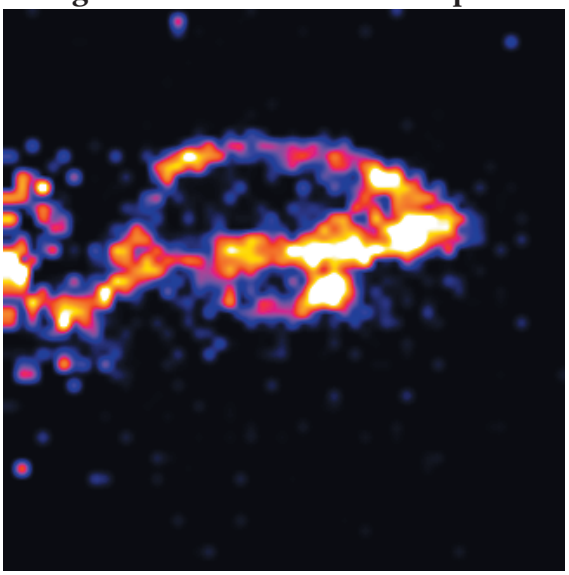

humans.

Although this mouse exhibited excellent uptake in the skeletal system, preliminary attempts yielded less desirable results. It was noticed that longer delays between injection and imaging (4 hours) produced much better skeletal uptake than shorter delays (2 hours). Bladder uptake was noted to obscure the discernment of the pelvic region. Poor skeletal uptake was also noted for mice that remained under anesthesia during drug washout. Similar results were also obtained for 2 rats in concert with Isra Saeed in Thomas Lang's lab. In addition, none of the tumor-bearing mice in this study exhibited metastatis to any part of the skeleton, as assessed by necrospy, indicating a low probability for metastasis despite a large primary tumor.

V. Discussion

We have used ^{99m}Tc-sestamibi to image breast tumors and metastases in mice with mixed results. One metastasis was detected easily due to high uptake and good retention of the drug. Other metastases were obscured due to poor uptake and respiratory motion. Primary tumors were also detected by this method, and exhibited a necrotic core surrounded by a thin rim of viable tissue. Skeletal uptake of ^{99m}Tc-MDP was also imaged in normal mice as preparation for a dual-isotope study which would image both soft tissue tumors and the consequences of their invasion of the skeletal system.

Dual-isotope studies involving tumor metastasis to the skeleton would have been interesting to perform in this model. For example, the imaging agent ^{125}I-iodorotenone was studied

in collaboration with A. Hwang. Briefly, ^{125}I-iodorotenone is derived from the chemical rotenone, which has been used as a fish poison. Its mechanism of uptake is similar to that of ^{99m}Tc-sestamibi in that is membrane permeant and relies on a negative membrane potential for cellular uptake. Once in the cell, ^{125}I-iodorotenone crosses the mitochondrial membrane, again due to the negative membrane potential, and it finally localizes to complex I of the electron transport chain. Because its ^{125}I label can be substituted by ^{123}I, which emits a gamma ray suitable for human imaging, ^{125}I-iodorotenone is under consideration as an alternative to ^{99m}Tc-sestamibi as a perfusion agent in the small animal arena. The use of this agent would allow us to simultaneously image a tumor metastasis to bone using ^{99m}Tc-MDP and the perfusion of the tumor using ^{125}I-iodorotenone. This would be an interesting area to pursue in the future.

VI. References

1. Minino AM, Heron MP, Smith BL. *Deaths: preliminary data for 2004.* Natl Vital Stat Rep. 2006 Jun 28;54(19):1-49

2. Ziessman HA, O'Malley JP, Thrall JH. *Nuclear Medicine: The Requisites, Third Edition (Requisites in Radiology).* Mosby; 3 edition (December 21, 2005)

3. Spanu A, Schillaci O, Madeddu G. *99mTc labelled cationic lipophilic complexes in malignant and benign tumors: the role of SPET and pinhole-SPET in breast cancer, differentiated thyroid carcinoma and hyperparathyroidism.* Q J Nucl Med Mol Imaging. 2005 Jun;49(2):145-69

4. Schillaci O, Spanu A, Madeddu G. *[99mTc]sestamibi and [99mTc]tetrofosmin in oncology: SPET and fusion imaging in lung cancer, malignant lymphomas and brain tumors.* Q J Nucl Med Mol Imaging. 2005 Jun;49(2):133-44

5. Taillefer R. *Clinical applications of 99mTc-sestamibi scintimammography.* Semin Nucl Med. 2005 Apr;35(2):100-15

6. Welm AL, Sneddon JB, Taylor C, Nuyten D, Van de Vijver MJ, Hasegawa BH, and Bishop JM. *Macrophage stimulating protein promotes metastasis of breast cancer: implications for prediction of clinical outcome in humans.* Data ahead of print

7. VanBrocklin HF, Hanrahan SM, Enas JD, Nandanan E, O'Neil JP. Mitochondrial

avid radioprobes. *Preparation and evaluation of 7'(Z)-[125I]iodorotenone and 7'(Z)-[125I]iodorotenol.* Nucl Med Biol. 2007 Jan;34(1):109-16

8. Marshall RC, Powers-Risius P, Reutter BW, Taylor SE, VanBrocklin HF, Huesman RH, Budinger TF. *Kinetic analysis of 125I-iodorotenone as a deposited myocardial flow tracer: comparison with 99mTc-sestamibi.* J Nucl Med. 2001 Feb;42(2):272-81

Chapter 7

CT Cancer Studies In Mice

I. Introduction

Chronic diseases such as cancer are among the leading causes of death in industrialized nations such as the United States[1]. In this country, approximately one out of every five people who die this year will die of cancer. Furthermore, it is becoming increasingly evident that disease conditions depend upon a number of risk factors, many of which interact, and most which are poorly understood. For example, one such factor which is common to many chronic conditions is blood flow, or perfusion, and there is a large body of study devoted to the improvement of our understanding of the molecular mechanisms involved in the evaluation of tissue perfusion and the factors which influence its evolution.

We would further like to extend the utility of our dual-isotope methodology to include complementary perfusion measurements made with CT. Although CT imaging is often used to help localize and enhance the physiological information provided by SPECT, it may be used to provide functional perfusion imaging in its own right[2-4]. Because many researchers tend to focus exclusively on the functional capabilities of one modality, the ability of dual-modality imaging to provide information about *physiological* correlations (as opposed to structural/physiological relationships) is often overlooked. The ability of CT to provide functional information about perfusion will also open up the possibility of using combined dual-isotope SPECT/CT to assess the effect of *interactions* between biological molecules on perfusion. Therefore, in addition to our evaluation of perfusion

correlations via SPECT agents, we will evaluate a new CT contrast agent, Fenestra VC, as a perfusion marker. Previous studies using CT contrast agents to evaluate perfusion have suffered from difficulties involving x-ray beam hardening and contrast agent washout during the experiment[5]. We believe that the use of this new contrast agent in mice will greatly reduce these difficulties, due to the small size of the mouse and the long vascular retention time of this agent. In addition, we will develop a new method of mathematical decomposition of CT images to provide quantitative data about the location and extent of soft tissue vascularity. Previous studies have made attempts to relate absolute image values to levels of vascularity in a tissue using inanimate calibration standards and solutions, and have met variable success. We believe that there is more utility in using measurements taken from the mouse's tissues themselves and will employ measurements of both the blood pool and poorly vascularized tissue in the place of inanimate calibrations.

This perfusion measurement will be relevant to cancer studies, in which the ability of a tumor to respond to chemotherapeutic drugs or radiation treatments often rests on its level of perfusion. In particular, there is much interest in the level of oxygen available to the tumor, which is dependent upon blood flow; hypoxia (a low level of oxygen) often confers radioresistance to certain areas of large tumors, making them difficult to treat. Again, although almost any mouse model of cancer could be used, the Welm model of mammary carcinoma would provide an excellent opportunity to test this idea *in vivo*.

II. Background

II.I Macrophage-Stimulating Factor and Its Relationship to Breast Tumor Metastasis

As mentioned in Chapter 6, one molecular factor which has received much recent attention is macrophage stimulating factor (MSP). This molecule is related to epithelial cell survival and is postulated to have a role in development of carcinomas such as those of breast cancer. Our colleague, Alana Welm, is investigating the role of MSP in the metastasis of mammary carcinoma of the breast. She has developed an orthotopic model in which primary cells are removed from the mammary glands of a normal mouse; infected with a retrovirus carrying the genes for some combination of the polyoma middle T antigen (PyMT), dsRed, GFP, and macrophage stimulating protein (MSP); and returned to the cleared inguinal fat pad of the mouse. There, these cells form large primary tumors, and depending on the genes transferred to them, also metastasize to the lung and skeleton. Because the Welm model exhibits metastasis in addition to production of primary tumors, this is a unique opportunity to test the efficacy of our methodology in a physiologic setting which is highly relevant to that of the human disease case[6].

II.II CT Imaging in Breast Cancer

Although conventional CT imaging is useful in the localization of metastatic lesions, it does not provide much information concerning the perfusion of the lesion or of the primary tumor itself. Both of these measurements are of interest to the study of treatment and prevention of the cancer. To address this need, we have developed a mathematical

method to decompose CT images into relative amounts of soft tissue and blood containing iodinated contrast agent. Due to its unique advantages of long retention in the blood stream, we will employ the new contrast agent Fenestra VC to perform this study. In addition, we will compare the ability of Fenestra to convention CT imaging agents to effectively locate tumor metastases using CT imaging in the X-SPECT system.

II.III CT Imaging in the X-SPECT

The microCT imaging system in the X-SPECT utilizes a cone-beam geometry. X-rays emitted from the microfocus tube are generated at energies ranging from 0-50 kV_p and are collected with a pixelized GOS/CMOS detector; the tube operates at a current of 600 μA (although this can be extended to 1 mA). Each of the 1024 x 1024 detector pixels has a cross section of 48 μm x 48 μm. The distance from the x-ray source to the detector is 20 cm; under normal imaging conditions, the distance from the detector to the center of rotation is 73 mm, and the distance from the x-ray tube to the center of rotation is 225 mm. Under these conditions, and with a 1 mm thick aluminum filter on the x-ray beam, a typical 256-view CT scan will deliver 10 cGy to a mouse. This is approximately 1% of the accepted LD50/30 of 9 Gy.

II.IV CT Contrast Agents for Detection of Breast Tumor Metastasis

In our studies here, we would like to employ the use of a conventional CT contrast agent, iothalamate, and a new CT contrast agent (Fenestra VC) available from Alerion Biosciences for use in mice.

As mentioned in Chapter 4, iothalamate is a conventional CT contrast agent. Although it is used clinically, this high osmolarity of the contrast solution given to patients pulls water from the surrounding tissues and red blood cells into the blood vessels, causing heat and pain during dose administration. In addition, the hyperosmolar nature of the contrast solution is also associated with quick washout by the renal system and often concomitant acute renal failure. To compensate for this the base sugar molecule of iothalamate has a ring structure containing two side chains; an iodine atom is covalently bonded to each side chain. The side chains increase the polarity of the molecule, enhance its solubility in water, and hence reduce the toxicity of this agent. There are additional complications in murine studies due to the viscosity of the agent and the high doses delivered, namely difficulties related to flow through the narrow-bore needles required for tail vein injection and difficulties related to cardiac arrhythmia due to toxicity[7].

Fenestra VC and LC contrast agents have recently appeared on the market for use in small animals. Instead of being based upon an iodinated sugar, these agents mimic the structure and biological properties of a chylomicron. This has the advantage of long vascular retention and lowered toxicity, an ideal combination for small animal CT imaging, which may require as much as 30 minutes for data acquisition[8].

We will first verify the uptake of each of these imaging agents in tumors. Then we will apply CT decomposition methodology to images of solid tumors to obtain ratios of blood to soft tissue within the tumors. After imaging, these tumors will be perfused with fluorescently-labeled lectins. We will correlate these ratios to fluorescence measurements.

III. Methods

III.I Imaging Primary Breast Tumors Using Conventional CT Contrast Agents

Following procedures outlined in Chapter 4, between 200 and 900 microliters of iothalamate (300 mg I / mL) were injected over the course of 10-20 minutes. Due to toxicity concerns, injection was halted at the first sign of cardiac arrhythmia. The mouse was then placed on the scanner for imaging. 256 or 512 CT projections were acquired over 360º using an x-ray operating voltage of 50 kVp and 600 microamps current.

III.II Imaging Lung Tumors Using Fenestra CT Contrast Agents

Following procedures outlined in Chapter 4, 400 microliters of Fenestra VC or LC were injected over the course of 2-5 minutes. The mouse was then returned to its cage, given food and water, and allowed to recover for 1-4 hours. The mouse was then reanesthetized and placed on the scanner for imaging. 256 or 512 CT projections were acquired over 360º using an x-ray operating voltage of 50 kVp and 600 microamps current

III.III Imaging Bone Metastasis Using Noncontrast CT

Finally, it was noted that severe bone degradation due to tumor presence could be seen even on noncontrast CT images. These images were resliced to better highlight the deformity due to bone degradation and reactive growth and were also rendered using the Amira software package. The presence of tumor was confirmed by fluorescence microscopy (tumors were GFP-positive).

III.IV CT Decomposition Methodology

Tissue perfusion depends in part on the vascularity within the tissue. Because we know that Fenestra VC is retained in the vasculature, we assert that the relative contrast obtained in a contrast-enhanced CT image of a soft tissue will be a linear combination of the attenuation due to the soft tissue itself and the attenuation due to the presence of the contrast agent in the blood. Thus, if we know the attenuation of the soft tissue, we may infer the concentration of blood in the tissue based on its attenuation. This will allow us to calculate a blood/soft tissue ratio which may be a good measure of ischemia (heart) or hypoxia (tumor). We propose the following method for obtaining this blood/soft tissue ratio:

1) Measure attenuation coefficient of blood + Fenestra using CT images with contrast. Use ROI from left ventricle or aorta. This value represents the attenuation due to blood containing Fenestra contrast agent.

2) Measure attenuation coefficient of soft tissue using nonvascular region such as ear cartilage or subcutaneous fluid (not fat).

3) Decompose the images in a method similar to dual-energy CT. Using our tumor example, this yields

$$\mu_{\text{tissue/contrast}} = \mu_{\text{tissue/noncontrast CT}} + \mu_{\text{blood/Fenestra}}$$

where we expect the ratio of $\mu_{\text{tissue/noncontrast}}$ to $\mu_{\text{blood/Fenestra}}$ will be a relative measure of vascularity.

III.V Phantom Experiments Using CT Decomposition Methodology

To determine both the viability of our linearity assumption and the ability of our CT scanner to discriminate between varying levels of contrast agent dissolved in a liquid medium, a phantom experiment was performed. Seven microcentrifuge tubes were filled with several dilutions of iothalamate in isotonic saline ranging from pure saline to pure contrast and vortexed vigorously to ensure adequate mixing. The samples were immediately placed in a rack in the CT scanner and 512 CT projections were acquired over 360° using an x-ray operating voltage of 50 kVp and 600 microamps current.

Data were reconstructed and images were converted to Hounsfield units (HU) with custom c# software using the equation

$$HU = 1000*(I/I_{water} - 1)$$

where I is the raw image value and I_{water} is the raw image value of water (measured to be 821.9 for this machine in an earlier experiment by A. Hwang). A region of interest was drawn around each microcentrifuge tube in the reconstructed data and the mean and standard deviation for each was tabulated.

III.VI CT Decomposition Methodology Applied to *In Vivo* Studies in Mice

The decomposition methodology was then applied to CT data taken from mice injected with Fenestra VC. Data was converted from raw format to HU and to units of percent blood by volume using custom software as mentioned above. A region of interest was drawn around each organ studied, and the mean and standard deviation in both units were

tabulated. Using these statistics, the mean percentage blood volume needed to conclude that a suspected lesion was statistically different from the rest of the tissue was calculated using the Normal Test[9]

$$z = (\mu - \mu_0) / (\sigma / n^{1/2})$$

where μ is the mean of the suspected lesion, μ_0 is the mean of the surrounding tissue, σ is the standard deviation of the surrounding tissue, and n is the number of voxels in the suspected lesion. The threshold for considering suspected lesions as "real" was calculated as $|z| > 1.645$, using the one-sided rejection region and $p < 0.05$ for the probability of obtaining such a result by chance. The same test was performed to compare potential lesions to blood/Fenestra to exclude hemorrhage, vascular malformation, etc as a source of the lesion.

IV. Results

IV.I Imaging Primary Breast Tumors Using Conventional CT Contrast Agents

As discussed in chapter 4, Iothalamate proved to be a difficult imaging agent to use in practice. Its administration was complicated by the induction of arrhythmias which were often fatal. In addition, the rapid washout (a few seconds) proved to be quicker than our image acquisition hardware could handle (20 minutes per acquisition). Therefore the catheter and syringe pump delivery system mentioned above was implemented. This allowed a steady dose of contrast agent to be delivered to the mouse throughout the course of the experiment. The resulting images are shown below.

Figure 67: Iothalamate-Enhanced CT in Breast Cancer

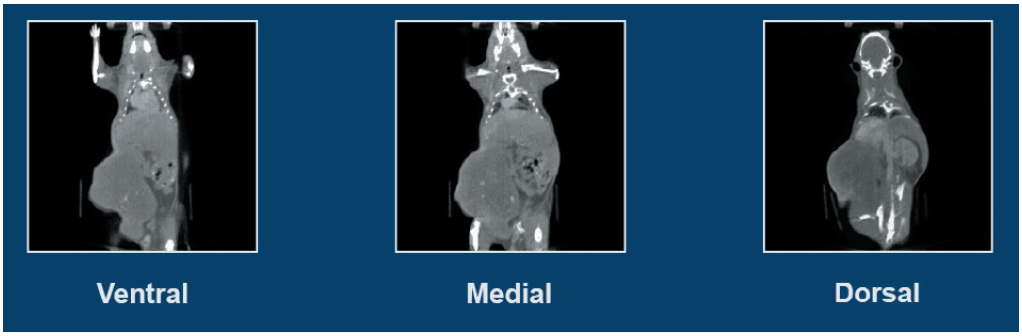

One kidney, a large primary mammary tumor, and the inferior vena cava can be seen quite clearly in these images. However, the arterial system is less distinct due to washout of the drug from the vascular system. Due to these difficulties, iothalamate was not judged an ideal agent for vascularity measurement using these methods and image decomposition was not attempted due to much superior contrast being obtained in other experiments with Fenestra contrast agent as demonstrated in the next section.

IV.II Imaging Lung Tumors Using Fenestra CT Contrast Agents

We observe excellent tumor uptake in similar lung tumor detection experiments using mice from Darya Soto and Alana Welm. The four contrast-enhanced images show good uptake of the Fenestra VC agent. Since the lung contains air spaces, the CT decomposition into blood/soft tissue is not expected to work well in this case, but we consider this good preliminary data showing tumor uptake of Fenestra VC, in contrast to the iothalamate images. In a later section, we intend to extend these experiments to other organs, such as the pancreas, where this decomposition is expected to perform nicely. Sample images are shown below.

Figure 68: Fenestra-Enhanced CT in Breast Cancer, Lung Metastasis

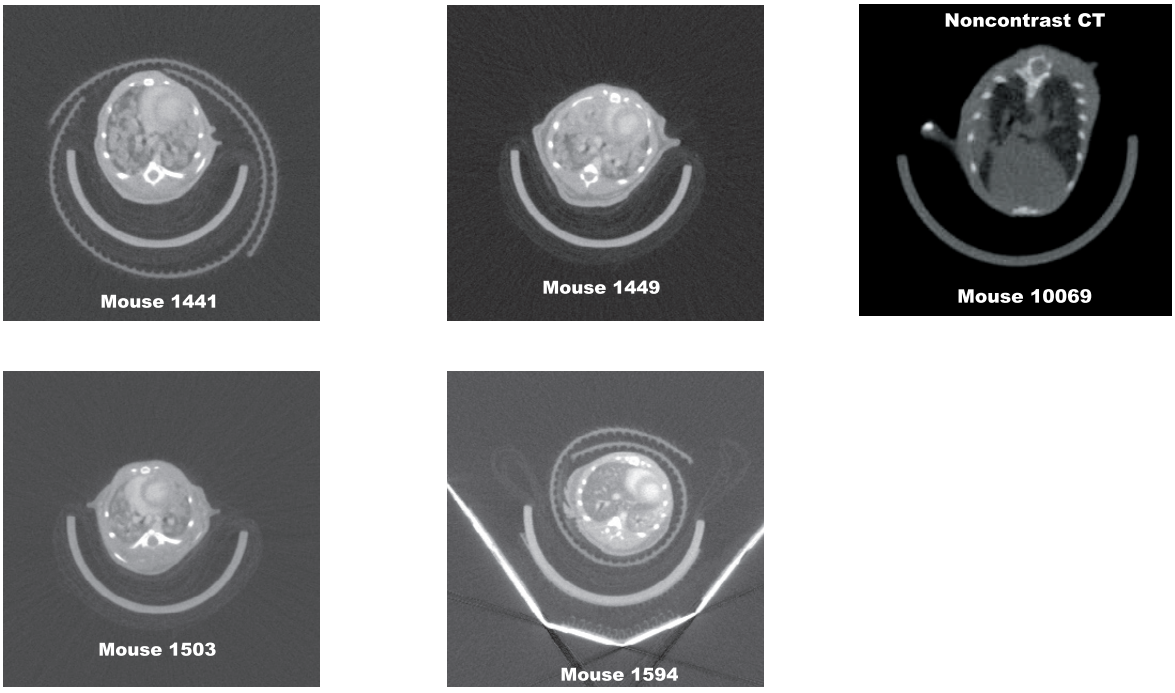

IV.III Imaging Bone Metastasis Using Noncontrast CT

We also used noncontrast CT to image the effects of breast metastasis to bone on the skeletal system. Because MSP is known to promote osteolysis, we expected that tumor metastasis to the skeletal system would result in degradation and reactive bone formation. Such a case is shown in the images below.

Figure 69: Breast Cancer Metastasis to Bone

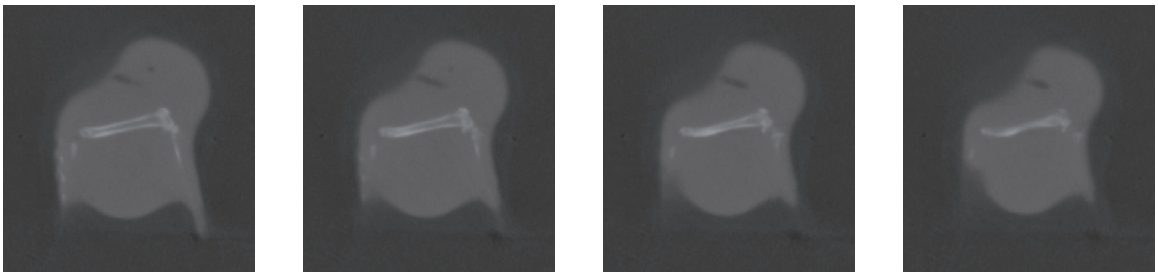

The distal femur shown in these slices exhibits extensive cortical degradation caused by direct invasion of breast tissue. Reactive bone formation can be seen in these images as well, as a sharp protrusion near the extreme distal end of the femur. This data is rendered as a surface below. Confirmation of breast tumor presence was verified with fluorescence microscopy. The image below shows the GFP-positive tumor perched on top of the distal femur, as expected from the CT data.

Figure 70: Validation of Breast Cancer Metastasis to Bone

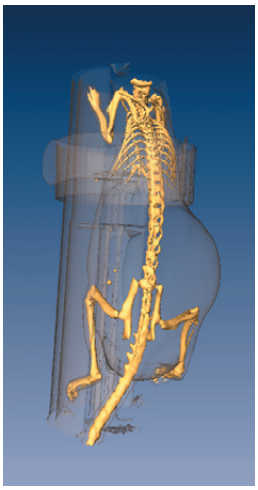

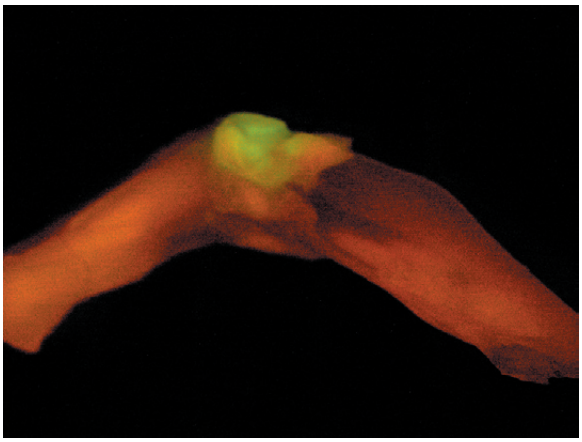

IV.IV Phantom Experiments in CT Decomposition

Varying concentrations of iothalamate in isotonic saline solution are easily resolved by CT imaging as shown below. Microcentrifuge #1 displays reconstruction artifacts caused by intense absorption of x-rays, and its value is not used in the table or graphs which follow.

Figure 71: Decomposition Phantom

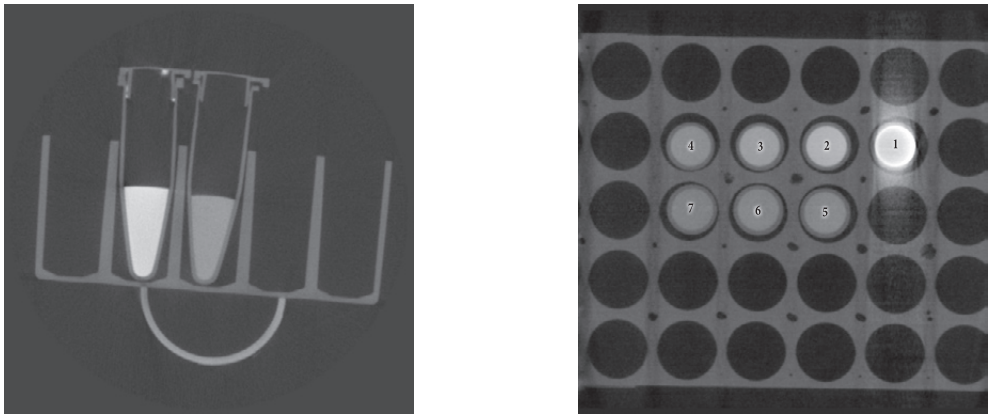

As shown in the table and graph below, there is a linear relationship between contrast concentration and average Hounsfield unit over the range of 0 to 1:10 dilution.

Table 9: Attenuation as a Function of Contrast Concentration

	Dilution of Contrast Agent	Mean (HU)	Standard Deviation (HU)
Microcentrifuge Tube #1	none	2328	387
Microcentrifuge Tube #2	1 : 10 (blood)	984	69
Microcentrifuge Tube #3	1 : 20 (bloodflow 50%)	537	48
Microcentrifuge Tube #4	1 : 50 (bloodflow 20%)	219	48
Microcentrifuge Tube #5	1 : 100 (bloodflow 10%)	130	57
Microcentrifuge Tube #6	1 : 200 (bloodflow 5%)	83	53
Microcentrifuge Tube #7	saline (avascular tissue)	12	50

Figure 72: Mean Attenuation vs. Iothalamate Concentration

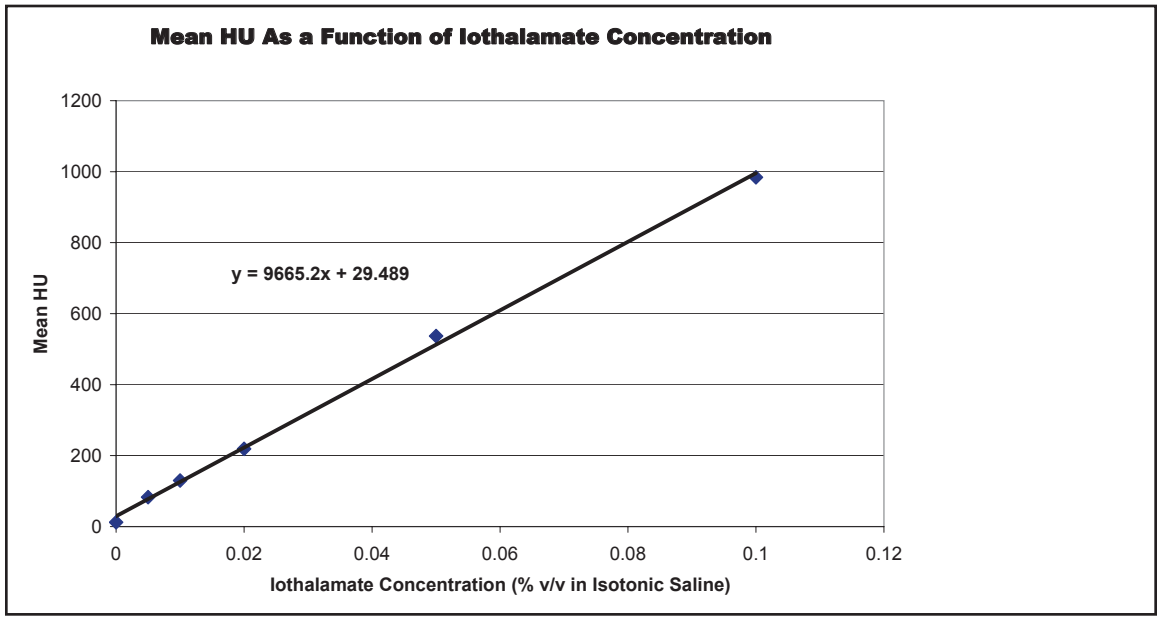

IV.V Decomposition of Solid Tumor CT Images Into Blood/Soft Tissue Ratios

An initial study showing the potential of this technique is shown below. Using the decomposition methodology described, each CT tomogram was converted to values of percent blood by volume. In the images below, white is 100% and black is 0%. Using this as a reference, several vascular features from each of the sample tomograms are highlighted. In the top left tomogram, which is taken through the thorax, the ventricular chambers and the myocardial wall are easily delineated. Several pulmonary vessels may also be seen throughout the lungs. In addition, on the left side there is an area of which appears much brighter than the surrounding lung tissue; on necropsy this was revealed to be a lung tumor which had expanded to fill an entire lobe of the left lung. The top right tomogram is taken through the liver, and several vessels may be seen as white tubular structures within the more uniformly grey liver. The left renal artery may be seen in the bottom left tomogram, and the right saphenous vein and left ureter may be seen at the bottom right.

Figure 73: CT Data Windowed for Blood/Soft Tissue Ratios

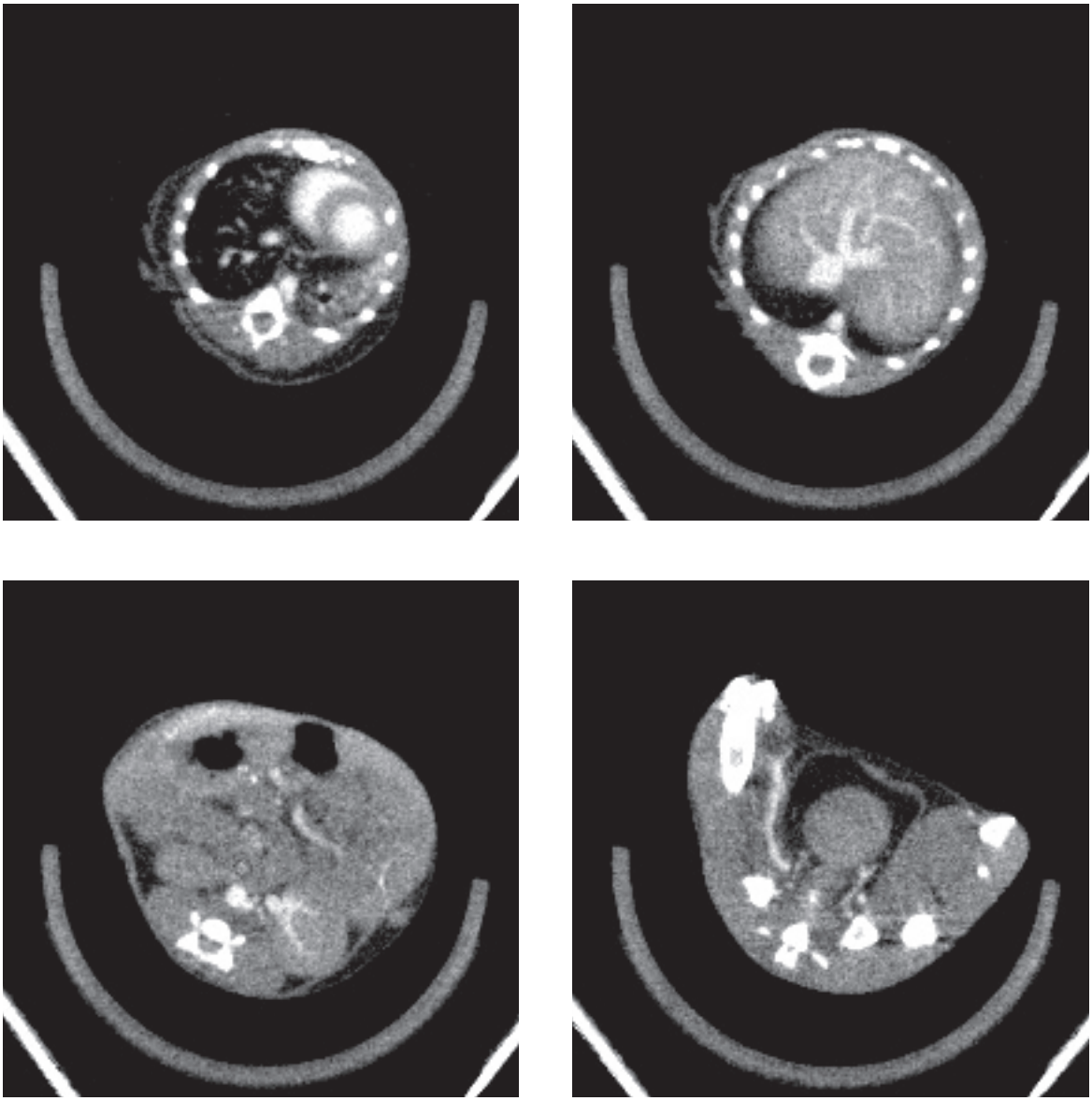

In addition to qualitative evaluation of these images, we also characterized this proposed vascularity measurement statistically. We drew regions of interest around several organs (excluding obvious large vessels) and tabulated the mean and standard deviation for each. Using these results and the Student's t-test, a threshold for hot and cold lesion detection is proposed in each of these organs based on the CT measurement of vascularity. Values are shown below for units of HU and % blood by volume, using $p < 0.05$ for lesion detection.

IV.VI Organ Statistics (HU)

Table 10: Organ Statistics (HU)

Organ	Mean	Standard Deviation	Std Dev / Mean
Heart	202.0	49.6	0.25
Liver	207.6	49.5	0.24
Lung	-292.6	73.0	0.25
Kidney	165.5	52.3	0.32
Intestine	70.7	51.2	0.72
Blood	484.6	80.1	0.17
IP Fluid	-234.8	59.0	0.25
Tumor	48.4	122.8	2.54

IV.VII Hot Lesion Mean Value Detectability Threshold (HU)

Table 11: Hot Lesion Mean Value Detectability Threshold (HU)

Lesion Size (Voxels)	Heart	Liver	Lung	Kidney	Intestine	Blood	IP Fluid
5	238.5	244.0	-238.9	204.0	108.4	543.5	-191.4
10	227.8	233.3	-254.6	192.7	97.3	526.3	-204.1
15	223.1	228.6	-261.6	187.7	92.4	518.6	-209.7
20	220.2	225.8	-265.7	184.7	89.5	514.1	-213.1
25	218.3	223.9	-268.6	182.7	87.5	511.0	-215.4
30	216.9	222.5	-270.7	181.2	86.1	508.7	-217.1
35	215.8	221.4	-272.3	180.0	84.9	506.9	-218.4
40	214.9	220.5	-273.6	179.1	84.0	505.4	-219.5
45	214.2	219.7	-274.7	178.3	83.3	504.2	-220.3
50	213.5	219.1	-275.6	177.7	82.6	503.2	-221.1

IV.VIII Cold Lesion Mean Value Detectability Threshold (HU)

Table 12: Cold Lesion Mean Value Detectability Threshold (HU)

Lesion Size (Voxels)	Heart	Liver	Lung	Kidney	Intestine	Blood	IP Fluid
5	165.5	171.2	-346.3	127.0	33.0	425.7	-278.2
10	176.2	181.9	-330.6	138.3	44.1	442.9	-265.5
15	180.9	186.6	-323.6	143.3	49.0	450.6	-259.9
20	183.8	189.4	-319.5	146.3	51.9	455.1	-256.5
25	185.7	191.3	-316.6	148.3	53.9	458.2	-254.2
30	187.1	192.7	-314.5	149.8	55.3	460.5	-252.5
35	188.2	193.8	-312.9	151.0	56.5	462.3	-251.2
40	189.1	194.7	-311.6	151.9	57.4	463.8	-250.1
45	189.8	195.5	-310.5	152.7	58.1	465.0	-249.3
50	190.5	196.1	-309.6	153.3	58.8	466.0	-248.5

IV.IX Organ Statistics (% Blood by Volume)

Table 13: Organ Statistics (% Blood by Volume)

Organ	Mean	Standard Deviation	Std Dev / Mean
Heart	57.0	5.6	0.10
Liver	60.0	6.3	0.11
Lung	0.2	0.9	4.50
Kidney	52.6	6.9	0.13
Intestine	42.9	7.1	0.17
Blood	96.7	4.9	0.05
IP Fluid	2.0	3.9	1.95
Tumor	37.9	17.0	0.45

IV.X Hot Lesion Mean Value Detectability Threshold (% Blood by Volume)

Table 14: Hot Lesion Mean Value Detectability Threshold (% Blood by Volume)

Lesion Size (Voxels)	Heart	Liver	Lung	Kidney	Intestine	Blood	IP Fluid
5	61.1	64.6	0.9	57.7	48.1	100.3	4.9
10	59.9	63.3	0.7	56.2	46.6	99.2	4.0
15	59.4	62.7	0.6	55.5	45.9	98.8	3.7
20	59.1	62.3	0.5	55.1	45.5	98.5	3.4
25	58.8	62.1	0.5	54.9	45.2	98.3	3.3
30	58.7	61.9	0.5	54.7	45.0	98.2	3.2
35	58.6	61.8	0.5	54.5	44.9	98.1	3.1
40	58.5	61.6	0.4	54.4	44.7	98.0	3.0
45	58.4	61.5	0.4	54.3	44.6	97.9	3.0
50	58.3	61.5	0.4	54.2	44.6	97.8	2.9

IV.XI Cold Lesion Mean Value Detectability Threshold (% Blood by Volume)

Table 15: Cold Lesion Mean Value Detectability Threshold (% Blood by Volume)

Lesion Size (Voxels)	Heart	Liver	Lung	Kidney	Intestine	Blood	IP Fluid
5	52.9	55.4	n/a	47.5	37.7	93.1	n/a
10	54.1	56.7	n/a	49.0	39.2	94.2	0.0
15	54.6	57.3	n/a	49.7	39.9	94.6	0.3
20	54.9	57.7	n/a	50.1	40.3	94.9	0.6
25	55.2	57.9	n/a	50.3	40.6	95.1	0.7
30	55.3	58.1	n/a	50.5	40.8	95.2	0.8
35	55.4	58.2	n/a	50.7	40.9	95.3	0.9
40	55.5	58.4	0.0	50.8	41.1	95.4	1.0
45	55.6	58.5	0.0	50.9	41.2	95.5	1.0
50	55.7	58.5	0.0	51.0	41.2	95.6	1.1

In the final table, a value of *n/a* means that cold lesions are not detectable. This is expected because air in the lung renders the average percentage of blood by volume very low. In addition, this will likely not affect tumor detectability because long tumors are far more dense that lung tissue, which means they will appear as a hot lesion.

Interestingly, decomposition into percent blood by volume yields a smaller standard deviation to mean ratio, suggesting that this methodology may be a more sensitive measure of lesion detectability. Therefore, because the vasculature is so well highlighted with this technique, we would like to validate these preliminary data using histological measurements of vascularity and extend these measurements to include studies correlating percent blood by volume both to histological detection of tumors and to measurements of vascularity. In addition, we think that it would be quite interesting to investigate the ability of this measurement to predict vascularity in turmors and to investigate whether this measurement could be used to predict a tumor's response to therapeutic agents. This idea will be investigated in the next section.

V. Discussion

We have successfully used CT imaging to detect several types of tumors. We used contrast-enhanced CT with iothalamate contrast media to detect primary breast tumors. In addition, we used contrast-enhanced CT with Fenestra VC to image lung tumors in mice, and obtained excellent contrast agent uptake in these tumors. Finally, we used noncontrast-enhanced CT to image tumor effects on the skeleton, locating an instance of direct invasion from adjacent breast tissue.

We also developed a method to decompose CT images into blood/soft tissue ratios in order to measure tissue vascularity, a factor which is related to perfusion. We demonstrated the efficacy of this method in phantom experiments, and determined that there is a linear relationship between attenuation and the ratio of contrast agent to isotonic saline in solution. Moreover, we have acquired preliminary data in tumor-bearing mice suggesting that this methodology may be used to determine a statistical basis for lesion detection based on vascularity. We also wish to acknowledge here that this methodology may be improved by including a correction for beam hardening artifacts, and we think that this would be an interesting avenue to pursue in future development of this technique. We would also like to explore the application of this methodology to the areas of tumor radiosensitivity and chemotherapy response.

We think it would be interesting to validate and extend this methodology to *in vivo* studies. For example, to validate the methodology developed above in live animals, solid tumor bearing mice could be obtained in collaboration with Minh To in Allan Balmain's laboratory and injected with Fenestra, and CT imaging would be performed as described. On comparison with histology, we expect that the necrotic core of the tumor would exhibit less enhancement than the outer edges of the tumor. We also expect that areas exhibiting high levels of enhancement on CT images will likewise exhibit high levels of fluorescence in the lectin experiment. We also think it would be interesting to correlate the measured blood/soft tissue ratios with tumor response to chemotherapy and to tumor radiosensitivity.

VI. References

1. Minino, A.M., M.P. Heron, and B.L. Smith, ***Deaths: preliminary data for 2004.*** Natl Vital Stat Rep, 2006. 54(19): p. 1-49.

2. Parsons, M.W., et al., ***Identification of the penumbra and infarct core on hyperacute noncontrast and perfusion CT.*** Neurology, 2007. 68(10): p. 730-6.

3. Wintermark, M., et al., ***Comparison of CT perfusion and angiography and MRI in selecting stroke patients for acute treatment.*** Neurology, 2007. 68(9): p. 694-7.

4. Goh, V., et al., ***Quantitative assessment of colorectal cancer tumor vascular parameters by using perfusion CT: influence of tumor region of interest.*** Radiology, 2008. 247(3): p. 726-32.

5. Komemushi, A., et al., ***CT perfusion of the liver during selective hepatic arteriography: pure arterial blood perfusion of liver tumor and parenchyma.*** Radiat Med, 2003. 21(6): p. 246-51.

6. Feldmann, H.J., et al., ***Evaluation of tumor blood perfusion by dynamic MRI and CT in patients undergoing thermoradiotherapy.*** Eur J Radiol, 1993. 16(3): p. 224-9.

7. Miles, K.A., ***Perfusion CT for the assessment of tumour vascularity: which protocol?*** Br J Radiol, 2003. 76 Spec No 1: p. S36-42.

8. Welm, A.L., et al., ***The macrophage-stimulating protein pathway promotes metastasis in a mouse model for breast cancer and predicts poor prognosis in humans.*** Proc Natl Acad Sci U S A, 2007. 104(18): p. 7570-5.

9. Almen, T., ***Contrast media: the relation of chemical structure, animal toxicity and adverse clinical effects.*** Am J Cardiol, 1990. 66(14): p. 2F-8F.

10. Badea, C.T., et al., ***4-D micro-CT of the mouse heart.*** Mol Imaging, 2005. 4(2): p. 110-6.

Chapter 8

MRI Studies of Osteoarthritis in Total Knee Arthroplasty Specimens

I. Introduction

Evaluation of glycosaminoglycan (GAG) concentration in articular cartilage is of particular interest to the study of degenerative joint diseases such as osteoarthritis (OA). Noninvasive imaging techniques such as magnetic resonance imaging (MRI) and computed tomography (CT) have demonstrated the potential to assess biochemical markers of cartilage integrity such as GAG content; however, many imaging techniques are available and the optimization of particular techniques in the diagnosis of joint disease remains an active area of research. In order to highlight the differences between these various approaches, this work compares MRI (T_1, T_2, and $T_{1\rho}$) and contrast-enhanced CT in human articular cartilage, in both the presence and absence of gadolinium-based contrast agent.

II. Background

Osteoarthritis (OA) is a chronic degenerative disease characterized primarily by the loss of articular cartilage. Loss of articular cartilage may lead to inflammation, pain, and associated pathology such as the growth of new vasculature, osteophyte development, and joint space narrowing. Traditionally, OA has been diagnosed by these secondary indicators of cartilage loss via radiographic examination[1], in which a planar x-ray is used to assess the presence or absence of osteophytes and the width of the joint space; determination of pathology is based on indirect measures of surrounding anatomical structures[2]. Although

this is an effective approach, radiographs tend to be limited to the detection of OA only at later stages of disease progression because they lack the ability to directly image soft tissues[3].

In addition, radiographs are relatively insensitive to biochemical changes, which are essential for early diagnosis and treatment of many pathologies. For example, in OA the early stages of cartilage degeneration are often marked by the loss of the proteoglycan components of the cartilage matrix[4]. Unlike collagen, which is uncharged, proteoglycans exhibit a net negative charge in solution; this fixed charge density attracts sodium and other small positive ions. These small ions in turn pull additional water into the cartilage matrix via osmosis and create a positive pressure within the tissue that helps articular cartilage to resist compressive loading forces encountered during normal activities such as walking and running. Disruption of proteoglycans may lead initially to swelling via increased osmotic pressure followed by the eventual loss of cartilage volume which accompanies the corresponding loss of particulates composed of degraded proteoglycan. As such, proteoglycan depletion and the concomitant degradation of the cartilage matrix has been hypothesized as one of the initiating events of the pathologic process leading to OA[5, 6].

This awareness of biochemical means of pathological assessment has spurred an increasing interest in employing the capabilities of MRI imaging (MRI) in the assessment of biochemical changes in the hopes of early diagnosis and treatment of diseases such as OA. MRI has all of the distinct advantages conferred from being a noninvasive assessment technique; moreover, it can assess cartilage morphology directly and has shown promise

for the detection of soft tissue changes. For example, T_2 relaxation times have been correlated with degradation of cartilage matrix[7], $T_{1\rho}$ relaxation times with proteoglycan degradation[8], and T_1 values using delayed gadolinium enhanced MR imaging of cartilage (dGEMRIC) with proteoglycan content of cartilage[9, 10]. MRI has even been used to study the sodium content of cartilage directly by using new techniques to image sodium ions[11-13]. Each of these techniques offers a unique glimpse of the pathological processes encountered during the development of OA.

T_2 imaging studies are of interest to OA because T_2 is sensitive to tissue hydration. Early degradative changes in the extracellular matrix affect tissue hydration not only by increasing the overall water content via osmosis but also by increasing the mobility of water. T_2 has been found to be negatively correlated with both cartilage volume and thickness[14, 15], and focal areas of increased T_2 levels have been found to correspond to cartilage lesion upon arthroscopic evaluation[16, 17]. In addition, early osteoarthritic changes in T_2 have been linked to changes in collagen content[18-20]. However, T_2 is not correlated with proteoglycan loss in the literature.

In contrast, T_1 dGEMRIC studies have shown that proteoglycan content may be more directly inferred from the presence or absence of contrast agent accumulation within cartilage[6, 9, 10, 21]. In dGEMRIC studies, charged contrast agent such as gadopentate (Gd-DTPA2-) is allowed to diffuse into articular cartilage over at least two hours[22]. Because the gadopentate molecule exhibits a net negative charge, it is repulsed by the similarly negative fixed charge density due to proteoglycans within the cartilage matrix[23]. Damage to the matrix and the corresponding loss of proteoglycan component may be

inferred from imaging data indicating an increased concentration of contrast agent within focal areas of articular cartilage. dGEMRIC methods are appealing for assessment of biological changes in OA due to this sensitivity to proteoglycan content.

In addition, contrast-enhanced computed tomography (CT) has also been proposed as an alternative to dGEMRIC[24]. In a similar manner to dGEMRIC imaging, CT employs a charged contrast agent and sodium imaging uses the sodium ions to identify focal areas of proteoglycan loss. However, because detection of contrast agent is accomplished directly via measurements of increased x-ray attenuation, these methods require increased amounts of contrast agent to be injected into the patient prior to imaging and hence an increased risk of complications related to contrast administration. Despite this limitation, CT methods are attractive because the imaging procedure is quick and can produce images with high resolution and isotropic voxel dimensions.

$T_{1\rho}$ describes longitudinal relaxation in the rotating frame. Because $T_{1\rho}$ measurements can probe very low frequency interactions, they are especially suited to probing spin-lattice energy exchange between water and large molecules such as those which comprise the extracellular matrix in articular cartilage. Disruption of this matrix, specifically disruption of the proteoglycan content of the matrix, leads to a loss in water molecule motion restriction and hence to an increase in measured $TT_{1\rho}$[8, 25, 26]. In addition, proteoglycans are known to be major players responsible for the physical resilience of articular cartilage, and their loss has been correlated with a loss of mechanical integrity within articular tissue. Moreover, because proteoglycan loss is thought to precede the development of symptomatic OA, there is an interest in $T_{1\rho}$ as a noninvasive method for early assessment of disease

development[27].

In the wake of the development of new imaging methods for assessment of cartilage biochemistry, there is a need for a careful, systematic comparison of the proposed imaging parameters to assess the ability of each to assess pathology and progression of OA. Moreover, the relationships between each of these parameters have not been completely characterized; as such it is unknown which of the various imaging methods available might be complementary and hence could provide a better overall picture of OA pathology. The purpose of this study is to compare MRI (T_1, T_2, and $T_{1\rho}$) and contrast-enhanced CT in human articular cartilage, in both the presence and absence of gadolinium-based contrast agent.

III. Methods

III.I Specimen Preparation

Sixteen human osteochondral specimens were used in this study; four were obtained from OA patients undergoing total knee arthroplasty surgeries and twelve were harvested from cadavers obtained from the National Disease Research Institute (NDRI). Specimens were stored at -80°C until use; when needed, specimens were allowed to equilibrate overnight in an isotonic saline bath at 4°C. Baseline MRI data were obtained for T_1, T_2 and $T_{1\rho}$. Specimens were then soaked overnight at 4°C in an isotonic saline solution containing 1mM gadolinium (Magnevist, preparation) to approximate conditions present in the joint during the course of a dGEMRIC study. The following day, MRI data were again acquired

for T_1, T_2, and $T_{1\rho}$. Following contrast-enhanced MRI imaging, specimens were again soaked overnight in solution containing 250 mM gadolinium in preparation for contrast-enhanced computed tomography (CT) studies.

III.II Imaging Acquisition

MRI data were acquired on a 3T GE Excite Signa system using a quadrature transmit/receive wrist coil. The protocol included four sequences: sagittal three-dimensional water excitation high-resolution spoiled gradient-recalled (SPGR) imaging (TR/TE = 15/6.7 ms, flip angle = 12, FOV = 7 cm, matrix = 256 x 256, slice thickness = 2 mm, bandwidth = 31.25 kHz, number of excitation [NEX] = 1), T_1 mapping using a series of fast spin-echo inversion recovery sequences (TR/TE= 10/4.56 ms, FOV = 7 cm, matrix = 256 x 256, slice thickness, TI = 50, 130, 200, 400, 800, 2100ms respectively), followed by $T_{1\rho}$ and T_2 mapping sequences. A sagittal 3D $T_{1\rho}$-weighted imaging sequence developed previously in our lab was applied in this study[28]. Briefly, the sequence is composed of two parts: magnetization preparation based on spin-lock techniques for the imparting of $T_{1\rho}$ contrast, and a elliptical-centered segmented 3D SPGR acquisition immediately after $T_{1\rho}$ preparation during transient signal evolution. A RF cycling technique was applied to eliminate the adverse impact of longitudinal relaxation on quantitative accuracy. A variable flip angle train was designed to provide a flat signal response to eliminate the filtering effect in k-space caused by transient signal evolution. The duration of the spin-lock pulse was defined as time of spin-lock (TSL), and the strength of the spin-lock pulse was defined as spin-lock frequency (F_{SL}). The number of α pulses after each $T_{1\rho}$ magnetization preparation was defined as views per segment (VPS). There was a relatively long delay (time of recovery,

T_{rec}) between each magnetization preparation to allow enough and equal recovery of the magnetization before each $T_{1\rho}$ preparation. The imaging parameters are: TR/TE = 9.3/3.7 ms; FOV = 14 cm, matrix = 256 x 128, slice thickness = 2 mm, BW = 31.25 kHz, VPS = 64, T_{rec} = 1.5 s, TSL = 0, 10, 40, 80 ms, F_{SL} = 500 Hz. The T_2 quantification sequence is based on T_2 preparation pulses contained an MLEV train of nonselective composite $90_x180_y90_x$ refocusing pulses [29, 30], followed by a SPGR sequence as for $T_{1\rho}$ mapping (TE = 4.1, 14.5, 25, 45.9 ms).

CT images were obtained on a Scanco Medical XtremeCT, with an x-ray tube voltage of 60kVp and current of 900μA. Images were reconstructed isotropically at 41μm using software provided with the system.

III.III Image Post-Processing

$T_{1\rho}$ and T_2 maps were generated by fitting the data pixel-by-pixel to the equation $S(TSL) \sim exp(-TSL/T_{1\rho})$ *and* $S(TE) \sim exp(-TE/T_2)$ respectively. T_1 maps were generated with a pixel-by-pixel 3-parameter fitting program. R_1 and R_1(Gd) maps were calculated for each sample where $R_1 = 1/T_1$ and $R_1(Gd) = 1/T_1(Gd)$ for each voxel and where (Gd) indicates a measurement made in the presence of gadolinium; ΔR_1 was calculated as the difference between R_1(Gd) and R_1. Resulting images underwent rigid registration using the VTK CISG toolkit. To facilitate a direct comparison, after registration, computed tomography data were downsampled to match the resolution present in the MRI images. Cartilage was segmented semiautomatically using the first echo $T_{1\rho}$ images via a Bezier spline-based MATLAB program developed in-house. The generated 3D contours were overlaid to

aligned T_1, T_2, and $T_{1\rho}$ maps, and also with CT data for statistical analysis.

III.IV Statistical Analysis

Median values for each image slice were computed and used to calculate Spearman rank correlations between imaging parameters. T_1, T_2, and $T_{1\rho}$ values before and after the addition of contrast were compared using a paired t-test.

IV. Results

Sample image data are in shown in Figure 74. At the right and the left of the figure are grayscale CT and SPGR images for a single sagittal slice of imaging data. In addition, color overlays for T_1(Gd), $T_{1\rho}$, T_2, and CT image data for corresponding regions of interest (ROIs) are shown. Interestingly, a focal area of elevated T_1(Gd) values appears to correspond to a similar location of decreased $T_{1\rho}$ values and also to an area of decreased CT values, which suggests qualitatively that spatial correlations between these parameters may be present.

Figure 74: Sample Image Data from Osteoarthritis Specimens

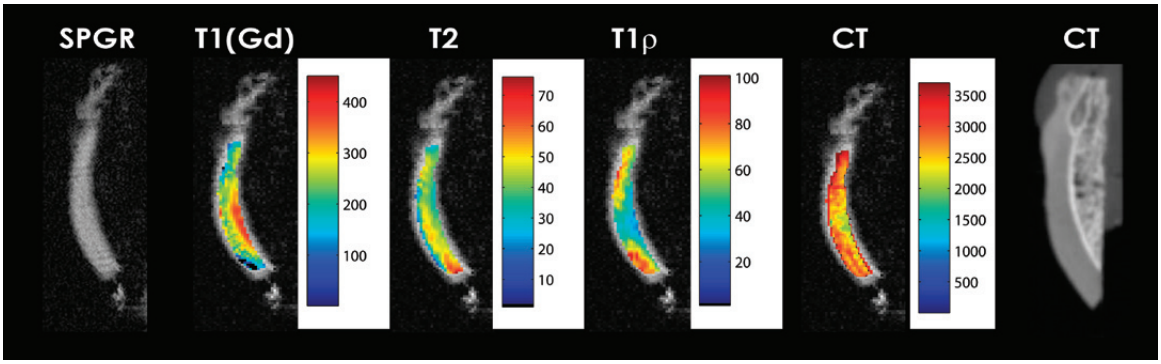

Figure 75 shows the effect of 1 mM gadolinium contrast on T_1, $T_{1\rho}$, and T_2. Addition of 1mM contrast was found to shorten T_1 and $T_{1\rho}$ values significantly, but was not found to affect T_2 values in articular cartilage. As shown in the figure, T_1 values were found to decrease significantly from a median value of 1136 ms to a median value of 244 ms upon equilibration with 1 mM gadolinium. $T_{1\rho}$ values were also found to decrease significantly from a median of 60 ms to 47 ms. As expected T_2 values were relatively unaffected by the addition of gadolinium (median 43 vs 42 ms).

Figure 75: Effect of Contrast on Relaxation Times

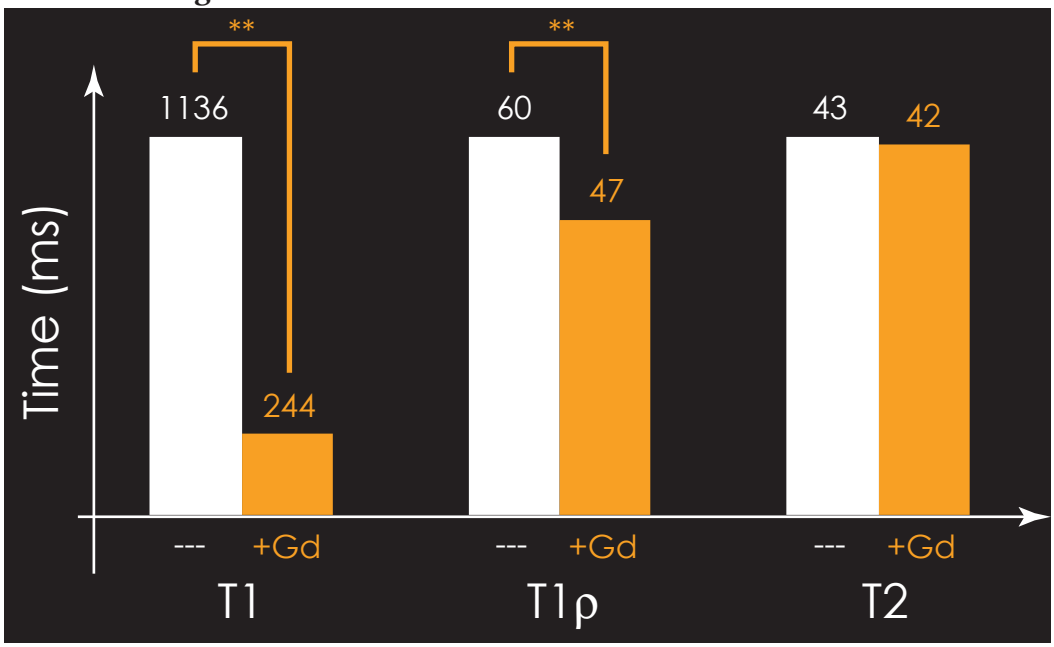

Table 1 displays the correlations between MRI and CT imaging parameters. As shown, T2 values were found to correlate equally mildly with $T_{1\rho}$, T_1(Gd), and ΔR_1 values (Spearman r= 0.24, -0.19, and 0.25, respectively, and $p < 0.05$ for each). In addition, $T_{1\rho}$ values were found to correlate very well (r = 0.68) with precontrast T_1 and less well with other parameters. ΔR_1 values were found to correlate extremely well (r = -0.96) with

T_1(Gd), although they were only mildly correlated with the other MRI imaging measures. Interestingly, $T_{1\rho}$ and T_1(Gd) imaging data were uncorrelated in this study. As expected, T_2 values were found to be uncorrelated with computed tomography data. In addition, $T_{1\rho}$ and T_1(Gd) values were found to be mildly correlated (r = 0.34 and -0.41, respectively, $p < 0.05$) with computed tomography. Finally, ΔR_1 was found to be moderately correlated with computed tomography (r = 0.48, $p<0.05$).

IV.I Spearman rank correlation between imaging parameters.

Table 16: Spearman Rank Correlations Between Imaging Parameters

	T_2	T_1	T_1(Gd)	ΔR_1	CT Attenuationn
$T_{1\rho}$	0.24*	0.68**	0.01	0.14	0.34**
T_2		0.41**	-0.19	0.25*	0.02
T_1			0.14	0.06	0.18
T_1(Gd)				-0.96**	-0.41**
ΔR_1					0.48**

* indicates $p < 0.05$, ** indicates $p < 0.005$

V. Discussion

MRI imaging has become prominent in the assessment of OA due to its ability to visualize soft tissues. In particular, the development of early OA has been associated with biochemically-driven changes such as cartilage swelling and macromolecular destruction, especially destruction of collagen and proteoglycan[31]. Due to this, the dGEMRIC technique for cartilage imaging has received much attention for its intuitive mechanistic appeal relating to the measurement of fixed charge density and hence its ability to characterize spatial variations of proteoglycans in cartilage. In addition, $T_{1\rho}$ imaging

has been shown to be sensitive to the macromolecular content of articular cartilage and as such has the potential to detect changes in proteoglycan content as well. Moreover, elevated osmotic pressure associated with inflammation and macromolecular destruction has generated much interest in T_2 characterization of OA due to the sensitivity of T_2 to fluid[18, 19].

In this study T_2 values correlated equally well on a regional basis with T_1(Gd), ΔR_1, and $T_{1\rho}$. However, the correlation was quite mild in all cases, which is likely based on the influence of local fluid accumulation. Although both T_2 and $T_{1\rho}$ are influenced by water motility, this result might be expected partially on the basis that $T_{1\rho}$ is sensitive to large molecular weight proteoglycans, whose degradation may not necessarily correlate on a spatial basis with fluid accumulation. In addition, the low effect of fluid on T_1(Gd) and ΔR_1 can be explained via Donnan equilibrium calculations in which gadolinium accumulation is predominately determined by the presence or absence of charged glycosaminoglycan within the cartilage matrix[23]. These calculations suggest that the equilibrium accumulation of contrast in articular cartilage is not expected to be influenced by fluid due to identical effects of hydration on fixed and mobile charge density, even though the rate of influx of contrast may be affected by the hydration of the extracellular matrix.

In addition, it was found that $T_{1\rho}$ correlated quite well with T_1, but was only mildly correlated with other MRI measures. Because spin-locking theoretically minimizes T_2 decay effects, a higher correlation between $T_{1\rho}$ and T_1 than between $T_{1\rho}$ and T_2 is consistent with effective spin-locking technique. Furthermore, it suggests that increasing spin locking frequency would increase the differences between correlations with T_1 and

T_2. Biochemically, the difference in correlations may be explained in part by the fact that both T_1 and $T_{1\rho}$ relaxation rates are influenced heavily by the molecular content of the cartilage matrix while influences on T_2 are through a more indirect mechanism[9, 27, 32]. This influence may not be specific to a particular macromolecular constituent. For example, although proteoglycans have received much interest as macromolecules whose loss may be indicative of OA progression, it is reasonable to assume that $T_{1\rho}$ changes seen in OA are at least in part affected by other macromolecular constituents of the extracellular matrix such as collagen because the proteoglycan content of cartilage is on the order of 3-6% by weight. However, in early OA, it is thought that proteoglycans are lost preferentially throughout the matrix; hence $T_{1\rho}$ may be specific to their loss at the onset of disease. In addition, although $T_{1\rho}$ may be affected by collagen, spin-locking technique suppresses dipolar interaction and therefore dependence of $T_{1\rho}$ on collagen; thus $T_{1\rho}$ may be more sensitive to PG[33, 34]. $T_{1\rho}$ may be dominated by PG due to its increased sensitivity to molecules in the proteoglycan weight range as compared to those in the collagen weight range. $T_{1\rho}$ relaxation rate ($1/T_{1\rho}$) has also been shown to decrease linearly with decreasing PG content in *ex vivo* bovine patellae[25] and has been proposed as a more specific indicator of PG content than T_2 relaxation in trypsinized cartilage[8]. Finally, $T_{1\rho}$ possesses a higher dynamic range than T_2, which may indicate an ability to discriminate between disease and health states with increased accuracy.

More recently, the use of contrast agents has proven useful in the evaluation of articular cartilage[21, 35-37]. Specifically, small, mobile, charged contrast agents can be used to probe the density of charged macromolecules in the extracellular matrix such as

proteoglycans. Proteoglycan loss is thought to precede development of OA and thus the ability to probe this property of cartilage may provide a method of early diagnosis of underlying pathology. Interestingly, in this study T_1(Gd) was found to be uncorrelated to $T_{1\rho}$ although it has been documented that both measures are sensitive to proteoglycan loss in articular cartilage. The low correlation between T_2 and $T_{1\rho}$ suggests that hydration may play a role in the discrepancy, although it is doubtful that this will account for the entire effect seen here. Although it was not assessed in this study, it is likely that both collagen and proteoglycan were degraded in many of the samples leading to complex changes in $T_{1\rho}$. In addition, it is likely that destruction of proteoglycan is a heterogeneous process in which the loss of fixed charge density does not correlate exactly with the loss of macromolecular mass. The exact ratio of charge to mass lost will depend on the specific degradative enzymatic pathway which predominates, and this is quite likely to vary from region to region within the joint. Such a heterogeneous loss of charge relative to mass (or vice versa) could certainly explain the results presented here.

Employing methodology similar to that of dGEMRIC imaging, contrast-enhanced computed tomography techniques have also been studied as a potential method for imaging proteoglycans in cartilage; as expected, CT attenuation values in this study were found to correlate on a regional basis with T_1(Gd). Interestingly, however, the correlation was moderate. This suggests that the quantitation of contrast accumulation is biased differently in the two techniques, which is reasonable given that the physical mechanisms of x-ray absorption and nuclear magnetic energy transfer are widely different. Contrast-enhanced computed tomography has a potential advantage in that it detects the presence

of contrast agent by directly sensing its electron density instead of relying indirectly on its effect on tissue relaxation times. In addition, relaxation times are affected by such effects as inhomogeneities in the magnetic field which make absolute quantitation of relaxation times challenging. At the present time, however, concerns related to radiation exposure and administration of increased contrast agent dose will likely require some technological advancement before the use of computed tomography becomes widespread in human studies of OA.

Together, these results indicate that $T_{1\rho}$, T_2, contrast-enhanced techniques may provide complementary information about the molecular environment in cartilage during the evolution of OA. In particular we found the low correlation between $T_{1\rho}$ and dGEMRIC to be quite surprising, suggesting that the mechanistic picture of proteoglycan loss early in OA may not be complete. In addition, we note only a moderate correlation between contrast-enhanced computed tomography and the dGEMRIC index, which suggests that T_1(Gd) may be influenced by factors in addition to contrast agent accumulation. Finally, we report that T_2 values were essentially uncorrelated with the other imaging measures studied here, indicating that T_2 may provide additional, complementary information beyond what can be obtained with T_1(Gd), $T_{1\rho}$, or contrast-enhanced computed tomography. We expect that further study will expand our understanding of these relationships.

VI. References

1. Altman, R., J. Fries, and D. Bloch, *Radiographic assessment of progression in osteoarthritis.* Arthritis Rheum, 1987. **30**: p. 11.

2. Rogers, J., Watt, and P. Dieppe, *A comparison of the visual and radiographic detection*

of bony changes at the knee joint. BMJ, 1990. **300**: p. 367-368.

3. Chan, W.P., et al., *Osteoarthritis of the knee: comparison of radiography, CT, and MR imaging to assess extent and severity.* Ajr Am J Roentgenol, 1991. **157**(4): p. 799-806.

4. Dijkgraaf, L.C., et al., *The structure, biochemistry, and metabolism of osteoarthritic cartilage: a review of the literature.* J Oral Maxillofac Surg, 1995. **53**(10): p. 1182-92.

5. Bashir, A., et al., *Glycosaminoglycan in articular cartilage: in vivo assessment with delayed Gd DTPA 2- -enhanced MR imaging.* Radiology, 1997. **205**(2): p. 551-8.

6. Bashir, A., M.L. Gray, and D. Burstein, *Gd-DTPA2- as a measure of cartilage degradation.* Magn Reson Med, 1996. **36**(5): p. 665-73.

7. Mlynarik, V., et al., *The role of relaxation times in monitoring proteoglycan depletion in articular cartilage.* J Magn Reson Imaging, 1999. **10**(4): p. 497-502.

8. Regatte, R.R., et al., *Proteoglycan depletion-induced changes in transverse relaxation maps of cartilage: comparison of T2 and T1rho.* Acad Radiol, 2002. **9**(12): p. 1388-94.

9. Bashir, A., et al., *Nondestructive imaging of human cartilage glycosaminoglycan concentration by MRI.* Magn Reson Med, 1999. **41**(5): p. 857-65.

10. Nieminen, M.T., et al., *Prediction of biomechanical properties of articular cartilage with quantitative magnetic resonance imaging.* J Biomech, 2004. **37**(3): p. 321-8.

11. Wheaton, A.J., et al., *Sodium magnetic resonance imaging of proteoglycan depletion in an in vivo model of osteoarthritis.* Acad Radiol, 2004. **11**(1): p. 21-8.

12. Shapiro, E.M., et al., *23Na MRI accurately measures fixed charge density in articular cartilage.* Magn Reson Med, 2002. **47**(2): p. 284-91.

13. Reddy, R., et al., *Sodium MRI of human articular cartilage in vivo.* Magn Reson Med, 1998. **39**(5): p. 697-701.

14. Blumenkrantz, G., et al. *Cartilage T2 as a Marker of Progression of Osteoarthritis*. in *ACR*. 2004. San Antonio, TX.

15. Dunn, T.C., et al., *T2 Relaxation Time of Cartilage at MR Imaging: Comparison with Severity of Knee Osteoarthritis.* Radiology, 2004. **232**(2): p. 592-598

16. Broderick, L., et al., *Severity of articular cartilage abnormality in patients with osteoarthritis: evaluation with fast spin-echo MR vs arthroscopy.* AJR, 1994. **162**: p. 99-103.

17. Peterfy, C.G., *Imaging of the disease process.* Curr Opin Rheumatol, 2002. **14**(5): p. 590-6.

18. Menezes, N.M., et al., *T2 and T1rho MRI in articular cartilage systems.* Magn Reson Med, 2004. **51**(3): p. 503-9.

19. Mosher, T.J., et al., *MR imaging and T2 mapping of femoral cartilage: in vivo determination of the magic angle effect.* AJR Am J Roentgenol, 2001. **177**(3): p. 665-9.

20. Xia, Y., J.B. Moody, and H. Alhadlaq, *Orientational dependence of T2 relaxation in articular cartilage: A microscopic MRI (microMRI) study.* Magn Reson Med, 2002. **48**(3): p. 460-9.

21. Burstein, D., et al., *Diffusion of small solutes in cartilage as measured by nuclear magnetic resonance (NMR) spectroscopy and imaging.* J Orthop Res, 1993. **11**: p. 465-478.

22. Burstein, D., et al., *Protocol issues for delayed Gd(DTPA)(2-)-enhanced MRI (dGEMRIC) for clinical evaluation of articular cartilage.* Magn Reson Med, 2001. **45**(1): p. 36-41.

23. Maroudas, A., *Distribution and diffusion of solutes in articular cartilage.* Biophys J, 1970. **10**(5): p. 365-79.

24. Cockman, M.D., et al., *Quantitative imaging of proteoglycan in cartilage using a gadolinium probe and microCT.* Osteoarthritis Cartilage, 2006. **14**(3): p. 210-4.

25. Duvvuri, U., et al., *T1rho-relaxation in articular cartilage: effects of enzymatic degradation.* Magn Reson Med, 1997. **38**(6): p. 863-7.

26. Regatte, R.R., et al., *In vivo proton MR three-dimensional T1rho mapping of human articular cartilage: initial experience.* Radiology, 2003. **229**(1): p. 269-74.

27. Li, X., et al., *In vivo T(1rho) and T(2) mapping of articular cartilage in osteoarthritis of the knee using 3 T MRI.* Osteoarthritis Cartilage, 2007. **15**(7): p. 789-97.

28. Li, X., et al., *In vivo T(1rho) mapping in cartilage using 3D magnetization-prepared angle-modulated partitioned k-space spoiled gradient echo snapshots (3D MAPSS).* Magn Reson Med, 2008. **59**(2): p. 298-307.

29. Brittain, J.H., et al., *Coronary angiography with magnetization-prepared T2 contrast.* Magn Reson Med, 1995. **33**(5): p. 689-96.

30. Foltz, W., et al., *Optimized spiral imaging for measurement of myocardial T2 relaxation.* Magn Reson Med, 2003. **49**(6): p. 1089-97.

31. Blumenkrantz, G. and S. Majumdar, *Quantitative magnetic resonance imaging of articular cartilage in osteoarthritis.* Eur Cell Mater, 2007. **13**: p. 76-86.

32. Li, X., et al., *In Vivo 3T Spiral Imaging Based Multi-slice $T_{1\rho}$ Mapping of Knee Cartilage in Osteoarthritis.* Mag. Res. Med, 2005. **54**(4): p. 929-936.

33. Makela, H.I., et al., *Proton exchange as a relaxation mechanism for T1 in the rotating frame in native and immobilized protein solutions.* Biochem Biophys Res Commun, 2001. **289**(4): p. 813-8.

34. Duvvuri, U., et al., *Water magnetic relaxation dispersion in biological systems: the contribution of proton exchange and implications for the noninvasive detection of cartilage*

degradation. Proc Natl Acad Sci U S A, 2001. **98**(22): p. 12479-84.

35. Kurkijarvi, J.E., et al., *Delayed gadolinium-enhanced MRI of cartilage (dGEMRIC) and T2 characteristics of human knee articular cartilage: topographical variation and relationships to mechanical properties.* Magn Reson Med, 2004. **52**(1): p. 41-6.

36. Williams, A., et al., *Glycosaminoglycan distribution in cartilage as determined by delayed gadolinium-enhanced MRI of cartilage (dGEMRIC): potential clinical applications.* AJR Am J Roentgenol, 2004. **182**(1): p. 167-72.

37. Williams, A., et al., *Delayed gadolinium-enhanced magnetic resonance imaging of cartilage in knee osteoarthritis: findings at different radiographic stages of disease and relationship to malalignment.* Arthritis Rheum, 2005. **52**(11): p. 3528-35.

Chapter 9

MRI Studies of Osteoarthritis in ACL-Transected Rabbits

I. Introduction

As mentioned in the last chapter, osteoarthritis (OA) is a chronic degenerative disease characterized primarily by the loss of articular cartilage. Loss of articular cartilage may lead to inflammation, pain, and associated pathology such as the growth of new vasculature, osteophyte development, and joint space narrowing. Although OA has been traditionally diagnosed by these secondary indicators of cartilage loss via radiographic examination[1], there remains much basic science research to be done before the pathology of the disease is fully understood. In particular, the scarcity of good animal models with relevance to the human condition has proven a challenge. Animal models are essential for the study of the basic pathologic processes which produce osteoarthritis, and they are also critical in the evaluation of new treatments, both surgical and pharmaceutical. In this chapter, we will extend the results of our previous *ex vivo* study and follow the development of OA in the anterior cruciate ligament (ACL) transection rabbit model using magnetic resonance imaging (MRI).

II. Background

For example, in a recent study, the effects of doxycycline on osteoarthritis progression were evaluated in a large scale clinical trial using radiographic assessment of joint space narrowing in the medial tibiofemoral compartment as the primary outcome measure[2].

Although the differences between treated and untreated groups were small, they were statistically significant and suggest that a more controlled, specific study might yield more insight into the mechanism of doxycycline modification of disease processes involved in joint degeneration. Toward this end, we propose to characterize the rabbit anterior cruciate ligament (ACL) transection model of osteoarthritis as an objective model which may be used to assess the effects of doxycycline treatment in a controlled manner. In the literature, ACL transection has been shown to reliably induce cartilage injury in experimental animals[3-6], and the effects of doxycycline have shown promising ability to mitigate the progression of osteoarthritis[7, 8]. Moreover, this model has additional relevance in that it mimics injuries sustained by athletes who have managed to tear their ACL due to excessive strain or injury. In this section, we will extend the utility of the rabbit ACL transection model to the longitudinal evaluation and characterization of doxycycline treatment. These longitudinal measurements will not only allow us to better account for individual variability, but will also provide us with a unique opportunity to study the natural history of cartilage repair.

III. Methods

III.I Coil Choice

We evaluated the use of three coils for the purposes of rabbit imaging: a quadrature transmit/receive wrist coil, a quadrature transmit/receive knee coil, and a custom coil made by our colleague Xiaoliang Zhang. Previous studies in our lab used the wrist coil as the coil of choice, but these studies were *ex vivo* and involved only isolated leg specimens

instead of whole rabbits. In light of this concern, we evaluated the coils first based on accommodation of rabbit anatomy, and then on signal to noise ratio using the SPGR and $T_{1\rho}$ sequences listed below. 6 rabbit cadavers obtained from opthamology studies were used for coil evaluation.

III.II *In Vivo* Studies

6 female New Zealand White (NZW) rabbits were used for this study. Each rabbit underwent bilateral knee surgery on the hind limbs. On the left side (ACLX), a medial arthrotomy was performed to expose the ACL for transection and removal from its attachment on the femoral condyle and tibia; on the right, only the medial arthrotomy was performed, and the ACL was left intact. The joint capsule was then closed, and the rabbits were allowed to recover. Total surgery time was about 15 minutes per animal. Immediately following surgery, rabbits were broken into two groups: treatment and control. The treatment group received 2.2 mg/kg doxycycline twice per day for the duration of the study. Control rabbits received no treatment. Rabbits were allowed free cage activities following surgery.

III.III MRI Imaging

Rabbits were imaged at three and six weeks post-surgery. In preparation for imaging, rabbits were injected with a mixture of ketamine and xylazine (30-50 mg/kg ketamine + 5-10 mg/kg xylazine). Once induced, rabbits were transferred to a custom positioner which was contoured to match a transmit/receive knee coil used for imaging. A pad

containing recirculating warm (37°C) water was placed underneath the rabbit to maintain body temperature, and a pulse oximeter was placed on a forepaw to monitor heart rate and oxygenation level during imaging. Anesthesia was supplemented as needed using isoflurane for the duration of the scan (~2 hours).

MRI data were acquired on a 3T GE Excite Signa system using a quadrature transmit/receive knee coil. The protocol included four sequences: sagittal three-dimensional water excitation high-resolution spoiled gradient-recalled (SPGR) imaging (TR/TE = 15/6.7 ms, flip angle = 12, FOV = 12 cm, matrix = 512 x 256, slice thickness = 1 mm, bandwidth = 31.25 kHz, number of excitation [NEX] = 1), followed by $T_{1\rho}$ and T_2 mapping sequences. A sagittal 3D $T_{1\rho}$-weighted imaging sequence developed previously in our lab[9]. Briefly, the sequence is composed of two parts: magnetization preparation based on spin-lock techniques for the imparting of $T_{1\rho}$ contrast, and an elliptical-centered segmented 3D SPGR acquisition immediately after $T_{1\rho}$ preparation during transient signal evolution. A radio frequency (RF) cycling technique was applied to eliminate the adverse impact of longitudinal relaxation on quantitative accuracy. A variable flip angle train was designed to provide a flat signal response to eliminate the filtering effect in k-space caused by transient signal evolution. The duration of the spin-lock pulse was defined as time of spin-lock (TSL), and the strength of the spin-lock pulse was defined as spin-lock frequency (F_{SL}). The number of α pulses after each $T_{1\rho}$ magnetization preparation was defined as views per segment (VPS). There was a relatively long delay (time of recovery, T_{rec}) between each magnetization preparation to allow enough and equal recovery of the magnetization before each $T_{1\rho}$ preparation. The imaging parameters are: TR/TE = 9.3/3.7 ms; FOV =

14 cm, matrix = 256 x 128, slice thickness = 1 mm, BW = 31.25 kHz, VPS = 64, T_{rec} = 1.5 s, TSL = 0, 10, 40, 80 ms, F_{SL} = 500 Hz. The T_2 quantification sequence was based on T_2 preparation pulses contained an MLEV train of nonselective composite $90_x180_y90_x$ refocusing pulses [10, 11], followed by a SPGR sequence as for $T_{1\rho}$ mapping (TE = 4.1, 14.5, 25, 45.9 ms).

Resulting images were segmented into five compartments using SPGR images: lateral femoral condyle (LFC), medial femoral condyle (MFC), lateral tibia (LT), medial tibia (MT), and patellofemoral (PF) compartments. Three slices per compartment were segmented. The LFC and LT were segmented starting medially at the insertion of the extensor digitorum longus (EDL) on the condyle. The MFC and MT were segmented starting just medial to the intercondylar notch. In addition, the only the most medial slice of the three in the MT included the entire section through the tibial plateau; the central and lateral slices in this compartment included only the posterior half of the cartilage due to extreme partial volume effects. Finally, in the PF compartment, the central three slices were chosen for segmentation. Data corresponding to the mean value from each slice for $T_{1\rho}$ and T_2 were tabulated, and a Wilcoxon rank test was performed to determine statistical significance between test groups.

IV. Results

IV.I Coil Choice

As shown below, although the wrist coil performs well for *ex vivo* studies, examination of rabbit anatomy reveals that the coil geometry is unsuitable for *in vivo* imaging. In contrast to humans, rabbits have short femurs, rendering their knees much closer to their bodies. In addition, because rabbits are quadrupeds, the orientation of their femurs in their pelvis is rotated to bring their hind limbs underneath them. Therefore, when whole rabbits were fitted with the wrist coil for imaging, it was found that the knee could not be centered in the coil because the length of the coil was too great. This is shown in the figure below which shows a photograph of the wrist coil and an illustration of the fit on the rabbit.

Figure 76: Wrist Coil Geometry

Next, the knee coil was evaluated. The knee coil was found to accommodate the entire rabbit inside comfortably, and allowed positioning of the pelvis such that the patella was centered lengthwise in the coil. However, due to the bulk of the rabbit's pelvis, the knees had to be placed near the inside edge of coil, as shown below. This arrangement did allow

for images to be taken, which will be discussed in the next section.

Figure 77: Knee Coil Geometry

Finally, we evaluated the custom coil. As shown, a circular design was first attempted. However, the rabbit's large muscles and oval shape of the leg made this geometry challenging to work with. In addition, this arrangement again placed the knee at the inside edge of the coil, instead of allowing the preferred centered placement.

Figure 78: Custom Coil Geometry

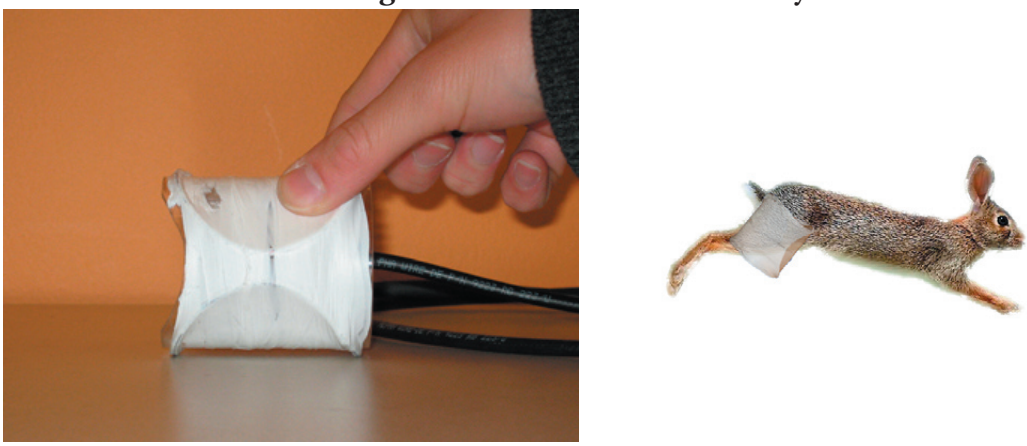

Next, the images were acquired with the dedicated coil and compared to images made with the same acquisition parameters on the knee coil. As shown below, the dedicated coil proved to be very sensitive to loading and to local field inhomogeneities, necessitating manual adjustment of transmit gain (top left), field shimming (not shown), and metal artifact reduction (top left) to avoid the artifacts shown here.

Figure 79: Artifacts from Improper Custom Coil Adjustment

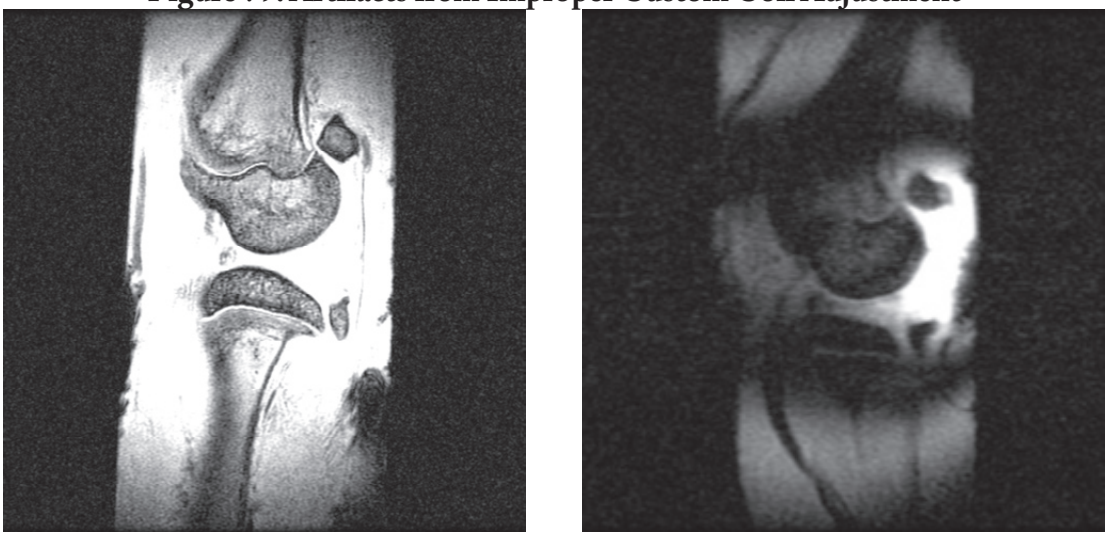

Figure 80: Proper Coil Adjustment

However, after manual adjustment, artifact free images were obtained with the dedicated coil as shown at the bottom left.

Finally, images from the dedicated and the knee coil were compared on the basis of signal to noise ratio (SNR). Corresponding SPGR images of the same specimen are shown below. SNR for cartilage was measured as 70.0 in the dedicated coil and 31.4 in the knee coil. This additional boost in SNR was not judged worth the additional time and effort required to manually adjust the imaging parameters, and therefore the decision was made to go with the knee coil on the basis of robustness.

Figure 81: Dedicated vs. Knee Coil

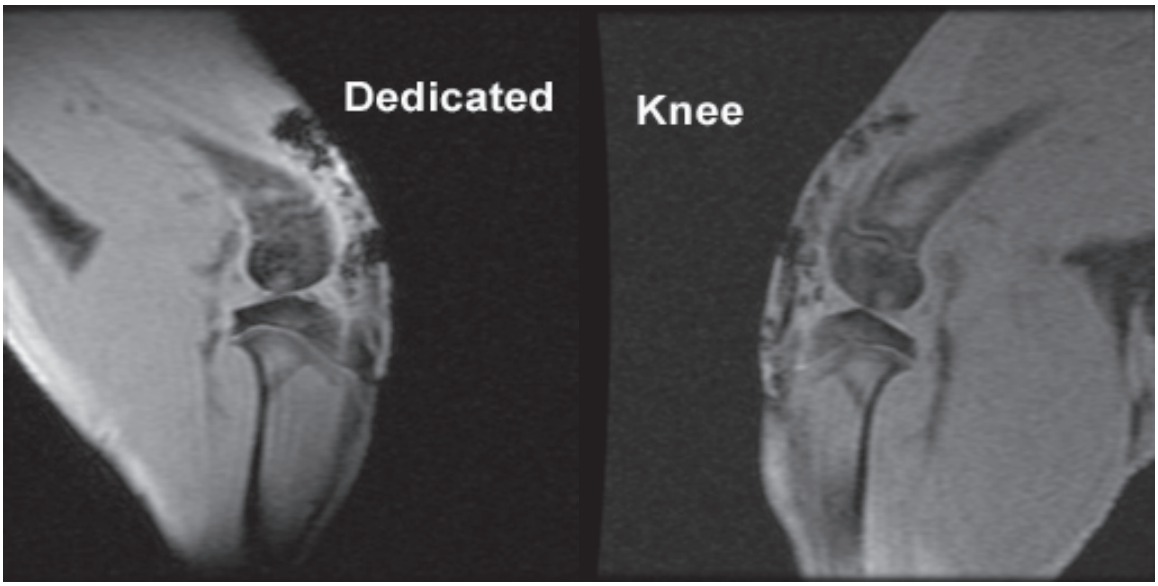

IV.II *In Vivo* Imaging

A schematic of the experimental setup is shown in Figure 1. As shown, the rabbit is anesthetized and placed in prone position such that its knees are centered within the human knee coil when fully extended. A custom nose cone supplies isoflurane and oxygen to the rabbit during the scan, and a recirculating warm water bath provides heat. The rabbit's pulse and oxygenation level are monitored via the use of a pulse oximeter positioned on the forepaw.

Figure 82: Custom Rabbit Holder Geometry

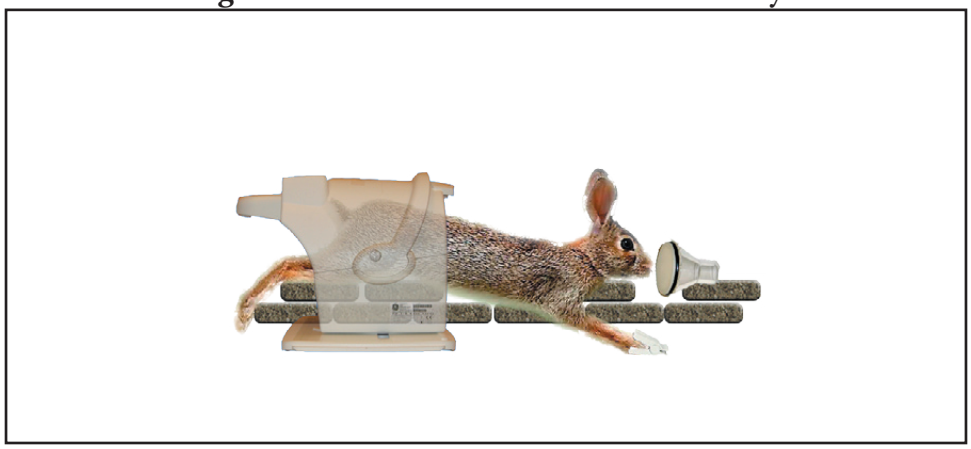

Figure 82 shows greater detail of the custom holder designed to position the rabbit correctly within the knee coil during the scan. The holder is constructed from high density polyethylene (HDPE) plastic, and is contoured to match the inner dimensions of the coil. Three supports in front of the coil and one behind are crossbraced to prevent movement of the top surface during loading, positioning, or imaging.

Figure 83: Custom Rabbit Holder Schematic

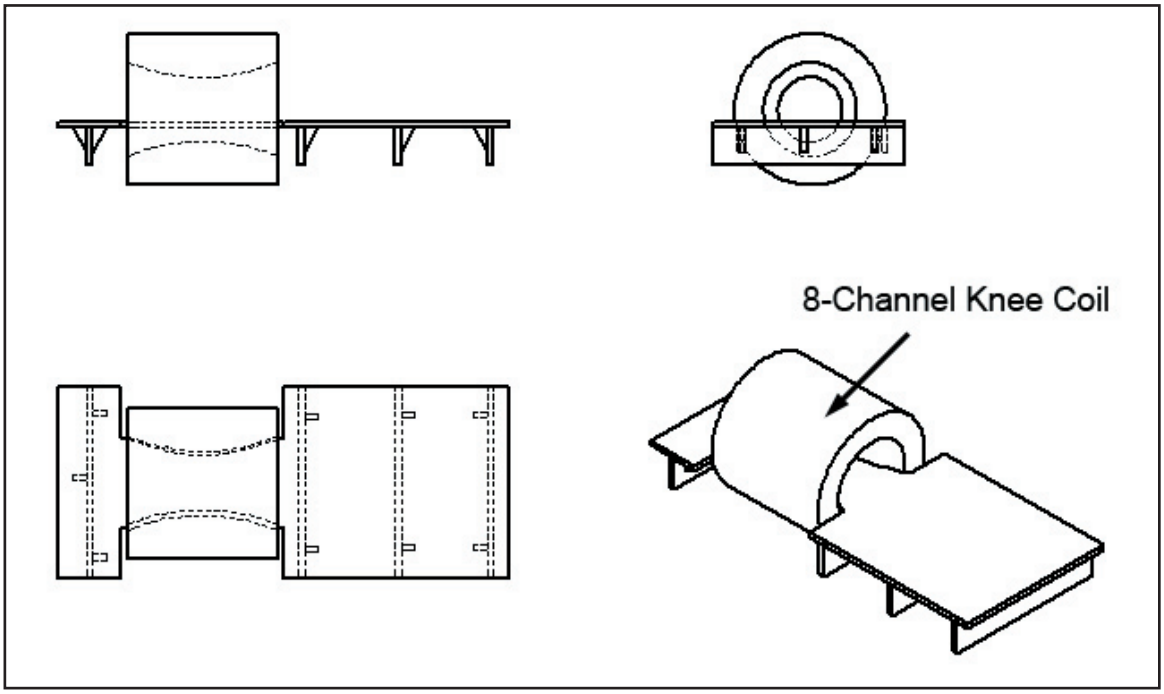

Figure 84 shows the final version of the holder, complete with anesthesia, heating, and monitoring equipment during an *in vivo* rabbit imaging session.

Figure 84: *In Vivo* Rabbit Imaging

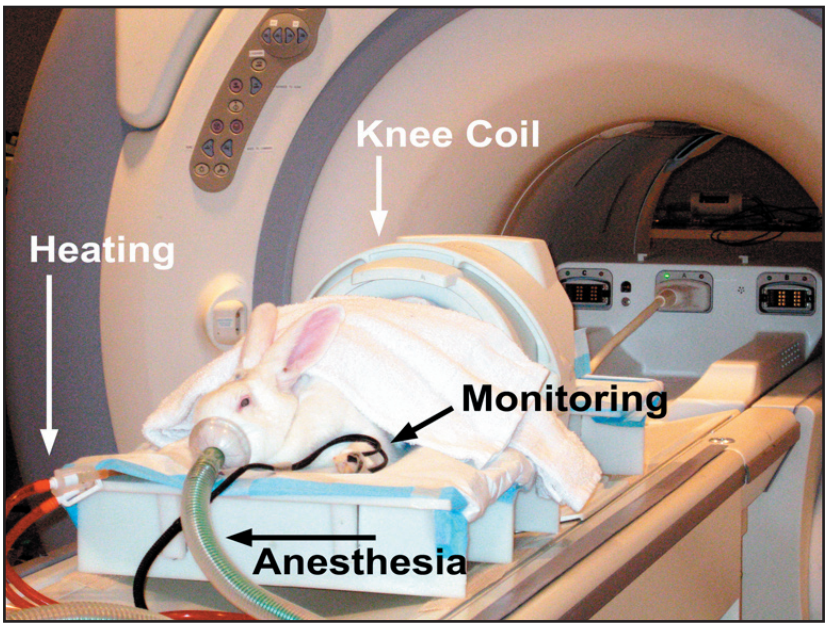

Sample image data are in shown in Figure 85. Shown at the left is a morphologic SPGR image through a lateral section of the right knee of one of the treatment rabbits; at the center is the corresponding segmentation of the LFC cartilage, and at the right is an overlay of the $T_{1\rho}$ data (in color) in the region of interest. Note that extreme partial volume effects are highlighted in this example, in which much of the data from the weight bearing region

Figure 85: Sample Image Data from Rabbit Knee *In Vivo*

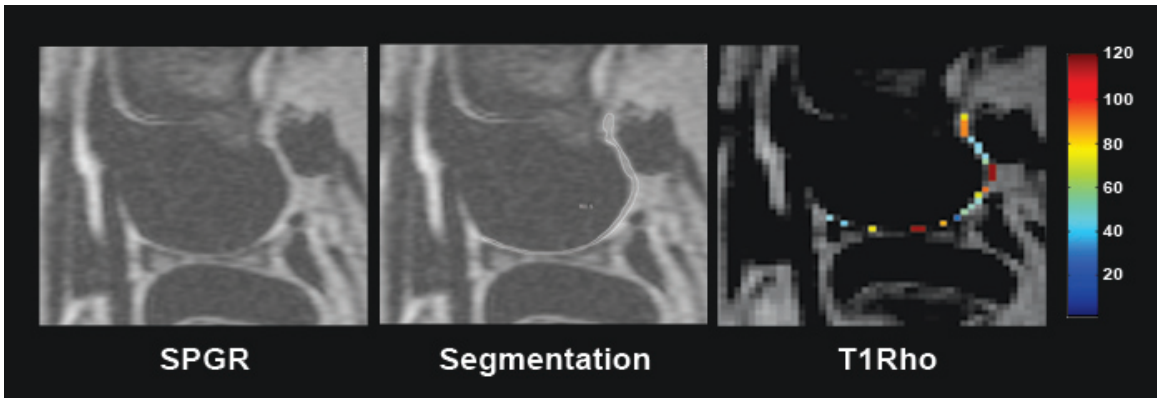

of the cartilage in not included when the region of interest taken from the SPGR image is overlaid on the $T_{1\rho}$ and T_2 maps; most rabbits exhibited some of this effect, although its presence was much less pronounced in those cases.

Figure 86 illustrates the effect of ACL transection at three and six weeks post surgery. Individual slice data from each compartment were pooled to assess the overall effect of ACL transection on $T_{1\rho}$ and T_2 data. Data from both the treatment group and the control group were also pooled to increase the statistical validity of the data. Statistically significant differences in $T_{1\rho}$ and T_2 between the ACLX side and the sham operated side can be seen in the MFC, MT, and LT at three weeks; $T_{1\rho}$ differences persist in the MFC and MT and T_2 differences persist in the MFC, and LT at six weeks. A change at six weeks is also seen at 6 weeks in the T_2 data, but in this case significance is driven by an outlier.

Figure 86: Effect of ACL Transection

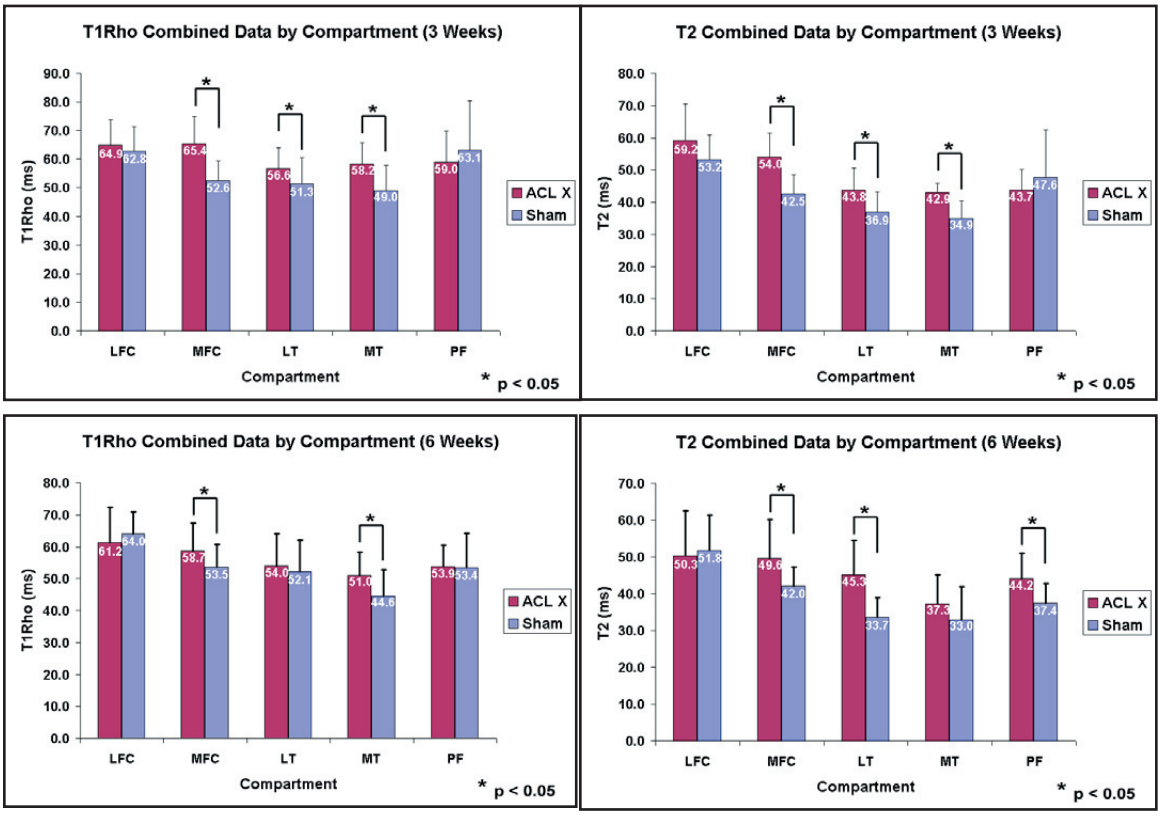

Figure 87 illustrates the progression as assessed by imaging parameters in both the sham operated and ACLX cases. Significant $T_{1\rho}$ and T_2 differences in the sham operated side can be seen only in the patellofemoral compartment, although they are driven by an outlier (rabbit 1167) exhibiting an extremely high value at three weeks. In contrast, $T_{1\rho}$ data indicates that ACLX knees improve over the time period from three to six weeks, with values reaching significance in the MFC and MT. In addition, there is a trend of improvement within all compartments which may be validated as more rabbits enter the study.

Figure 87: Progression as Measured by Imaging Parameters

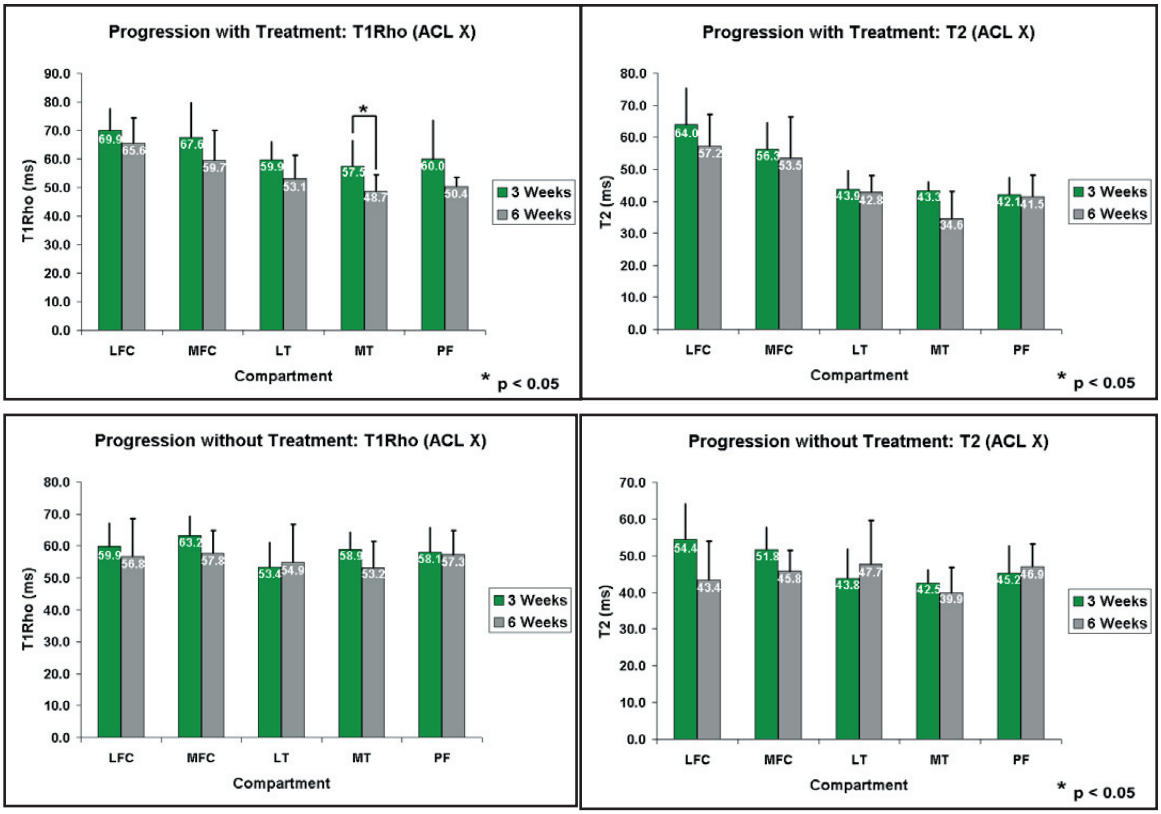

To assess the effect of treatment on progression, the data was further broken down into treatment and control cases. Figure 88 contains results for each of these cases in the ACLX

knee. As shown, there is no improvement as judged by imaging parameters in the absence of treatment, and no clear trend emerges as a function of time. However, in the treatment case there is a trend towards improvement over time, and the data becomes statistically significant in the MT compartment. However, the data indicates that the treated rabbits exhibit some higher initial (three week) values of T_2 and $T_{1\rho}$ than the nontreated rabbits, indicating a possible bias in this small data set.

Figure 88: Effect of Treatment on Progression

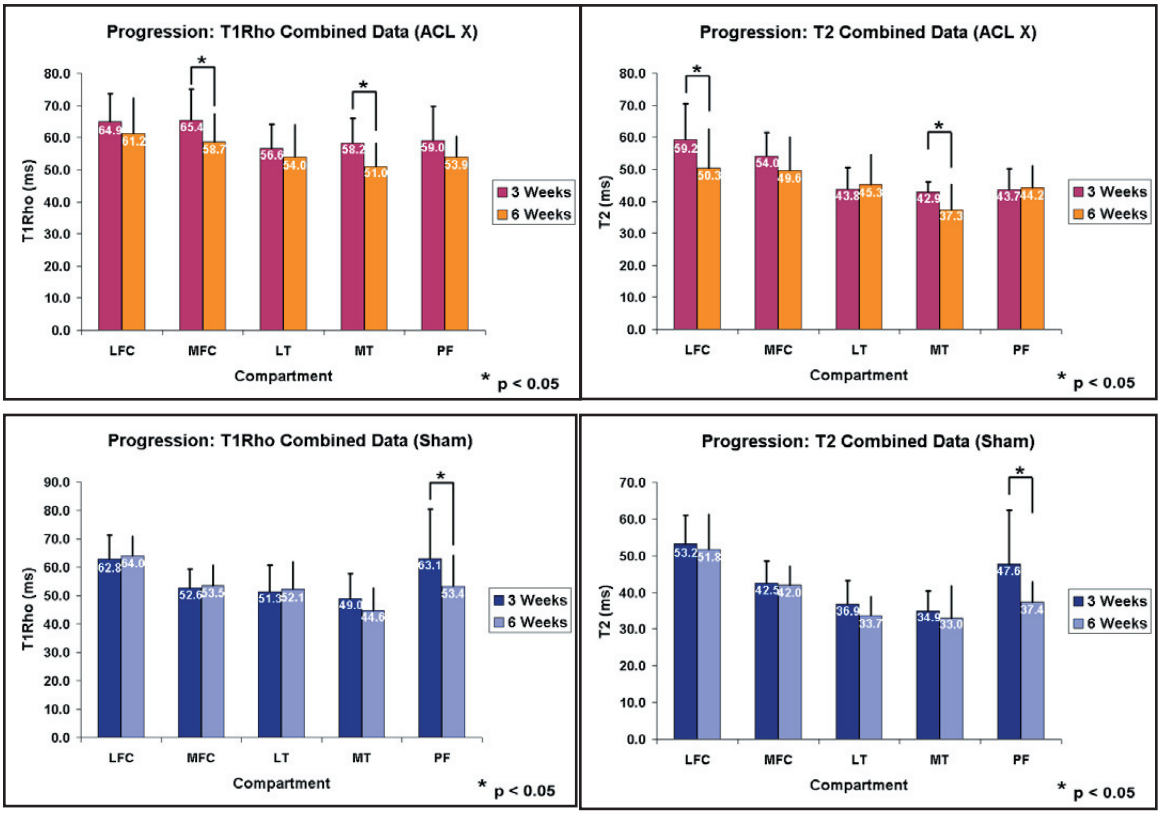

Finally, the data is Figure 88 was analyzed to account for individual variability. Data from each compartment in the sham operated knee was averaged and subtracted from that of the ACLX knee in each rabbit. Results are tabulated in Figure 89. In the doxycycline rabbits, there is a clear difference between the ACLX and sham operated knees, and the

difference resolves over time. In the control rabbits, there is almost no difference between the cases, and the difference remains small throughout the study. Interestingly, although $T_{1\rho}$ measures indicate differences in the rabbits receiving treatment over the course of the study, T_2 measures show no corresponding differences. However, more data is needed before these changes can be shown to be statistically significant or not.

Figure 89: Effect of Treatment on Progression Controlled for Individual Variability

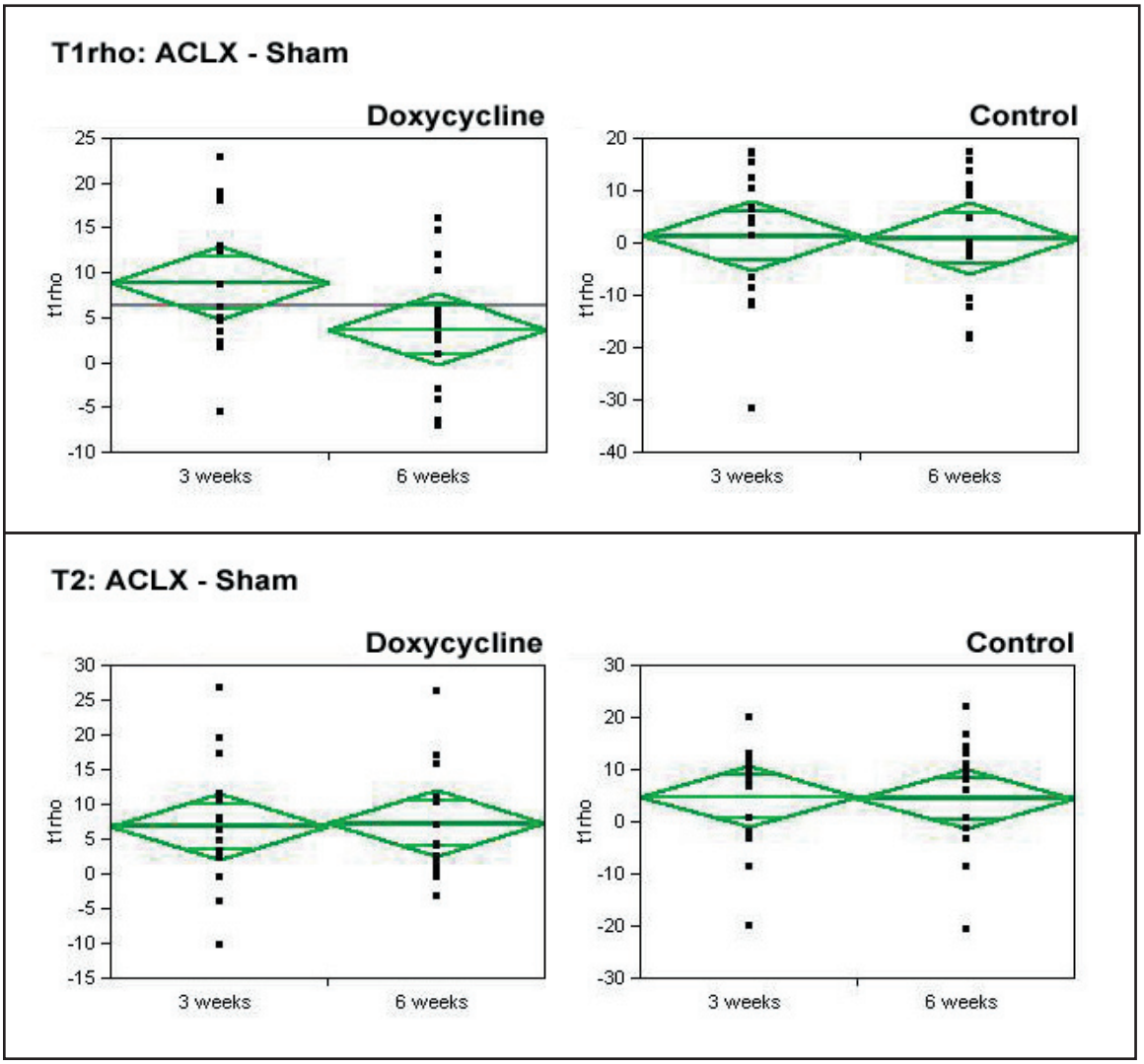

V. Discussion

The rabbit anterior cruciate ligament transection model of osteoarthritis is well established in the literature. In the course of this study, we have demonstrated the ability of MRI to follow the changes induced by ACL transection in rabbit articular cartilage. Moreover, we have demonstrated the ability to make longitudinal measurements and compare the disease states of small animals as they evolve over time, extending the utility of our small animal model to the characterization of the disease response to treatment. That being said, the discussion of the relevance of six rabbits to a disease which affects more than fourteen million people in the United States alone is rather preliminary at this time. However, this is preliminary data and is quite exciting despite this limitation. In addition, the ongoing rabbit ACL transection study will include more rabbits, which will lend statistical validity to the results presented here.

In this study, we have chosen to follow the development of osteoarthritis in rabbits secondary to ACL transection. In addition, we have chosen to examine the effects of doxycycline on disease progression following ACL transection; data in the literature suggests that doxycycline, an MMP inhibitor, may prevent the loss of cartilage through prevention of enzyme activity. The preliminary results presented here from three and six weeks post surgery indicate the potential for $T_{1\rho}$ and T_2 measurements to detect early damage to cartilage following ACL injury. Interestingly, the imaging data at three weeks indicated increased $T_{1\rho}$ values in ACL transected knees in rabbits treated with doxycycline relative to control rabbits. At six weeks, the difference between the two groups was reduced, but still evident. Combined with data in the literature suggesting that elevated $T_{1\rho}$ values

are associated with proteoglycan loss, this suggests that doxycycline may promote collagen preservation at the expense of proteoglycan loss early in the course of healing following an ACL tear. This result is in some contrast to the clinical trial presented by Brandt et al. in the literature, in which doxycycline was correlated with reduced measures of joint space narrowing. However, patients in the Brandt trial were studied at time intervals much longer than those used here, and the artificially induced mechanism of cartilage injury in the study presented here was quite different from the natural history presented in the Brandt study. Further study is warranted in order to clarify these differences.

Evaluation of treatments for chronic disease such as osteoarthritis can greatly benefit from controlled trials such as those presented here. In particular, a longitudinal study such as this has the additional benefit of reducing individual to individual variability, which allows us to tease out the details of pathologic progression or the response to treatment over time. In addition to providing a more complete picture of the biologic process under study, the capability to do longitudinal evaluation also reduces the cost of experiments in terms of animals, preparation (operating room) time, and personnel time. Moreover, with a noninvasive imaging modality such as MRI, the disease process itself does not have to be disturbed or manipulated in order for us as researchers to glean information.

VI. References

1. Altman, R., J. Fries, and D. Bloch, *Radiographic assessment of progression in osteoarthritis.* Arthritis Rheum, 1987. **30**: p. 11.

2. Brandt, K.D., *Modification by oral doxycycline administration of articular cartilage breakdown in osteoarthritis.* J Rheumatol Suppl, 1995. **43**: p. 149-51.

3. Smith, G., Jr., et al., *Effect of intraarticular hyaluronan injection on vertical ground*

reaction force and progression of osteoarthritis after anterior cruciate ligament transection. J Rheumatol, 2005. **32**(2): p. 325-34.

4. Smith, G.N., Jr., et al., *Effect of intraarticular hyaluronan injection on synovial fluid hyaluronan in the early stage of canine post-traumatic osteoarthritis.* J Rheumatol, 2001. **28**(6): p. 1341-6.

5. Smith, G.N., Jr., et al., *Diacerhein treatment reduces the severity of osteoarthritis in the canine cruciate-deficiency model of osteoarthritis.* Arthritis Rheum, 1999. **42**(3): p. 545-54.

6. Smith, G.N., Jr., et al., *Effect of intraarticular hyaluronan injection in experimental canine osteoarthritis.* Arthritis Rheum, 1998. **41**(6): p. 976-85.

7. Verbruggen, G., *Chondroprotective drugs in degenerative joint diseases.* Rheumatology (Oxford), 2006. **45**(2): p. 129-38.

8. Yu, L.P., Jr., et al., *Reduction of the severity of canine osteoarthritis by prophylactic treatment with oral doxycycline.* Arthritis Rheum, 1992. **35**(10): p. 1150-9.

9. Li, X., et al., *In vivo T(1rho) mapping in cartilage using 3D magnetization-prepared angle-modulated partitioned k-space spoiled gradient echo snapshots (3D MAPSS).* Magn Reson Med, 2008. **59**(2): p. 298-307.

10. Brittain, J.H., et al., *Coronary angiography with magnetization-prepared T2 contrast.* Magn Reson Med, 1995. **33**(5): p. 689-96.

11. Foltz, W., et al., *Optimized spiral imaging for measurement of myocardial T2 relaxation.* Magn Reson Med, 2003. **49**(6): p. 1089-97.

Chapter 10

Conclusion

As discussed in Chapter 1, chronic diseases such as cancer and cardiovascular disease are among the leading causes of death in industrialized nations such as the United States. In this country, approximately two out of every five people who die this year will die of heart disease. Of the rest, another one will die of cancer, and approximately one more will die of a stroke. In addition, chronic disease also causes huge health care expenses due to long term disability and pain. However, as science advances, we are developing more understanding of these diseases and better treatments for not only the root diseases but also their symptoms.

In this thesis, we developed the capability for studying chronic diseases in animal models using noninvasive imaging methods. In particular, we developed dual-isotope SPECT/CT methods, implemented hardware which would support the physiological needs of an animal during an imaging study, and used MRI as a means to study osteoarthritis in both human osteochondral specimens and rabbits with surgically-induced ACL transection. As delineated in the following section, the work presented here develops the capabilities of our imaging systems for the study of chronic disease in small animals using SPECT, CT, and MRI.

Development of Dual-Isotope Methodology

The microSPECT/CT imaging system in our laboratory did not ship with the capability

to perform dual-isotope SPECT, although the hardware contained within the system could support such a capability. Therefore, we developed the methodology ourselves. We employed our knowledge of photon acquisition to perform this task by characterizing the energy response of our recently-obtained X-SPECT microSPECT/microCT small animal imaging system (Gamma Medica-Ideas, Northridge, CA) to two radionuclides which exhibit photopeaks that differ widely in energy: technetium-99m (^{99m}Tc) and iodine-125 (^{125}I). Because no tools are provided by the manufacturer for examining any form of the raw data, we found and decoded this raw data. We then performed phantom experiments to determine our ability to construct useful projection data from the raw data from individual isotopes and reconstructed those projections into tomograms. We then separated the two signals and characterized the crosstalk between them, demonstrating the capacity to perfom two measurements simultaneously.

Hardware Specializations For Small Animal Imaging

We not only developed dual-isotope methodology but built tools which would allow us test its efficacy *in vivo*. Because work needed to be done in areas pertaining to support of the animal's physiology during the course of data acquisition in addition we also made some additional hardware modifications to our X-SPECT imaging system which will allow us to image live animals. These improvements include implementation of anesthesia, heating, and catheterization/syringe pump drug delivery for small animals. As the focus of this work is on chronic disease, these hardware implementations are vital to our ability to follow a disease course over time and perform repeated measurements on the same animal.

MicroSPECT/CT Perfusion Studies Using Mouse Models of Human Pathology

Using the dual-isotope methodology developed here, we demonstrated the capacity to image two isotopes simultaneously *in vivo* in normal mice. Therefore, any studies which could benefit from simultaneous acquisition of two types of data can be performed with this system: the only limitations are those related to availability and/or labeling of radioisotopes with ^{99m}Tc and ^{125}I. In the course of validating the dual-isotope data, we explored the application of SPECT and CT imaging to the study of mouse models of human disease and proposed two studies which would benefit from the use of our techniques. The first of these studies is the cardiac study of the simultaneous measurement of perfusion and innervation in the Conklin mouse model of dilated cardiomyopathy. The second study is the simultaneous measurement of perfusion and bone turnover in tumor metastasis to bone in the Welm model of mammary carcinoma. These two studies are only a sample of the kinds of work which can now be performed on the imaging systems in our laboratory, and we expect that many other experiments will eventually follow.

We also extended the utility of our methodology to include complementary perfusion measurements made with CT. We investigated a conventional CT contrast agent, iothalamate, and a new CT contrast agent, Fenestra VC, in breast and lung tumor detection studies. In addition, we developed a new method of mathematical decomposition of CT images to provide quantitative data about the location and extent of soft tissue perfusion; and we evaluate this method in phantoms. Again, we proposed a mouse study which would benefit from this methodology: a tumor perfusion/drug delivery study using the Welm model of mammary carcinoma.

MRI Studies of Osteoarthritis in Human and Animal Models

Finally, in order to demonstrate the utility of small animal imaging in chronic disease, we performed two validation studies using MRI to follow the development of osteoarthritis in both specimens obtained from total knee arthroplasty surgeries and also in rabbits which have had their ACL transected surgically. In the specimen study, we compared T_1, T_2, $T_{1\rho}$, and CT and determined the correlations between the imaging parameters. We found that although each of these imaging methodologies exhibits sensitivity to changes which occur in osteoarthritis, these differences are not highly correlated, indicating a complementary role in the characterization of disease. These results provided preliminary data suggesting that T_2 and $T_{1\rho}$ changes might be indicative of early degeneration of cartilage in osteoarthritis.

We extended the results of the specimen study to an *in vivo* rabbit study of osteoarthritis development secondary to ACL damage. In our rabbit study, we found that $T_{1\rho}$ data exhibited differences between rabbits treated with doxycycline following surgery and rabbits which were not treated. Although interesting, at this time the studies are quite preliminary and will require greater numbers for statistical validity. However, these studies clearly demonstrate the potential to use noninvasive imaging to study the development and progression of chronic disease *in vivo* in animal models. In addition, these studies will provide the framework for more comprehensive studies which may lend insight into diagnosis and treatment of chronic dieases.

Together, these results demonstrate the potential for small animal imaging to improve the study of chronic disease. In the course of this thesis, we have implemented the capabilities

for performing small animal studies, developed both custom software and hardware which enhance the abilities of our noninvasive imaging systems, and validated our methods *in vivo* using small animal such as rabbits and mice. We are excited to leave these new capabilities in the hands of researchers who will follow and hope that their studies will provide even more data which can be used to treat chronic conditions such as heart disease, cancer, and osteoarthritis.

Library Release

Publishing Agreement

It is the policy of the University of encourage the distribution of all theses and dissertations. Copies of all UCSF theses and dissertations will be routed to the library via the Graduate Division. The Library will make all theses and dissertations accessible to the public and will preserve these to the best of their abilities, in perpetuity.

I hereby grant permission to the Graduate Division of the University of California, San Francisco to release copies of my thesis to the Campus Library to provide access and preservation, in whole or in part, in perpetuity.

Signature: 

Date: 09/05/08